Noname manuscript No.
(will be inserted by the editor)

Implications of X-ray Observations for Electron Acceleration and Propagation in Solar Flares

G.D. Holman[1], M. J. Aschwanden[2], H. Aurass[3], M. Battaglia[4], P. C. Grigis[5], E. P. Kontar[6], W. Liu[1], P. Saint-Hilaire[7], and V. V. Zharkova[8]

September 30, 2011

Abstract High-energy X-rays and γ-rays from solar flares were discovered just over fifty years ago. Since that time, the standard for the interpretation of spatially integrated flare X-ray spectra at energies above several tens of keV has been the collisional thick-target model. After the launch of the *Reuven Ramaty High Energy Solar Spectroscopic Imager* (*RHESSI*) in early 2002, X-ray spectra and images have been of sufficient quality to allow a greater focus on the energetic electrons responsible for the X-ray emission, including their origin and their interactions with the flare plasma and magnetic field. The result has been new insights into the flaring process, as well as more quantitative models for both electron acceleration and propagation, and for the flare environment with which the electrons interact. In this article we review our current understanding of electron acceleration, energy loss, and propagation in flares. Implications of these new results for the collisional thick-target model, for general flare models, and for future flare studies are discussed.

Keywords Sun: flares, Sun: X-rays, gamma rays, Sun: radio radiation

Contents

[1] NASA Goddard Space Flight Center, Code 671, Greenbelt, MD 20771, U.S.A. E-mail: Gordon.D.Holman@nasa.gov
[2] Lockheed Martin Advanced Technology Center, Solar and Astrophysics Laboratory, Organization ADBS, Building 252, 3251 Hanover Street, Palo Alto, CA 94304, U.S.A.
[3] Astrophysikalisches Institut Potsdam
[4] Department of Physics & Astronomy, University of Glasgow, Glasgow, G12 8QQ, Scotland, UK
[5] Harvard-Smithsonian Center for Astrophysics P-148, 60 Garden St., Cambridge, MA 02138, U.S.A.
[6] Department of Physics and Astronomy, University of Glasgow, Kelvin Building, Glasgow, G12 8QQ, U.K.
[7] Space Sciences Lab, UC Berkeley, CA, U.S.A.
[8] Department of Computing and Mathematics, University of Bradford, Bradford, BD7 1DP, UK

1 Introduction

A primary characteristic of solar flares is the acceleration of electrons to high, suprathermal energies. These electrons are observed directly in interplanetary space, and indirectly at the Sun through the X-ray, γ-ray, and radio emissions they emit (Hudson & Ryan 1995). Understanding how these electrons are produced and how they evolve is fundamental to obtaining an understanding of energy release in flares. Therefore, one of the principal goals of solar flare research is to determine when, where, and how these electrons are accelerated to suprathermal energies, and what happens to them after they are accelerated to these high energies.

A major challenge to obtaining an understanding of electron acceleration in flares is that the location where they are accelerated is not necessarily where they are most easily observed. The flare-accelerated electrons that escape the Sun are not directly observed until they reach the instruments in space capable of detecting them, usually located at the distance of the Earth from the Sun. The properties of these electrons are easily modified during their long journey from the flaring region to the detecting instruments (e.g., Agueda et al. 2009). Distinguishing flare-accelerated electrons from electrons accelerated in interplanetary shock waves is also difficult (Kahler 2007).

The electrons that are observed at the Sun through their X-ray or γ-ray emissions radiate most intensely where the density of the ambient plasma is highest (see Section 2). Therefore,

the radiation from electrons in and near the acceleration region may not be intense enough to be observable. Although these radiating electrons are much closer to the acceleration region than those detected in interplanetary space, their properties can still be significantly modified as they propagate to the denser regions where they are observed. The radio emission from the accelerated electrons also depends on the plasma environment, especially the magnetic field strength for the gyrosynchrotron radiation observed from flares (Bastian et al. 1998). Therefore, determining when, where, and how the electrons were accelerated requires a substantial amount of deductive reasoning.

Here we focus primarily on the X-ray emission from the accelerated electrons. Interplanetary electrons and low-energy emissions are addressed by Fletcher et al. (2011), while the γ-ray emission is addressed by Vilmer et al. (2011), and the radio by White et al. (2011). The X-rays are predominantly *electron-ion bremsstrahlung* (free-free radiation), emitted when the accelerated electrons scatter off ions in the ambient thermal plasma. Issues related to the emission mechanism and deducing the properties of the emitting electrons from the X-ray observations are primarily addressed by Kontar et al. (2011). Here we address the interpretation of the X-ray observations in terms of flare models, and consider the implications of the observations for the acceleration process, energy release in flares, and electron propagation. Specific models for particle acceleration and energy release in flares are addressed by Zharkova et al. (2011).

The accelerated electrons interact with both ambient electrons and ions, but lose most of their energy through *electron-electron Coulomb collisions*. Consequently, the brightest X-ray sources are associated with high collisional energy losses. These losses in turn change the energy distribution of the radiating electrons. When the accelerated electrons lose their suprathermal energy to the ambient plasma as they radiate, the source region is called a *thick target*. Electrons streaming downward into the higher densities in lower regions of the solar atmosphere, or trapped long enough in lower density regions, will emit thick-target X-rays. Hence, thick-target models are important to understanding the origin and evolution of accelerated electrons in flares. Thick-target X-ray emission is addressed in Section 2.

The total energy carried by accelerated electrons is important to assessing acceleration models, especially considering that these electrons carry a significant fraction of the total energy released in flares. Also, the energy carried by electrons that escape the acceleration region is deposited elsewhere, primarily to heat the plasma in the thick-target source regions. The X-ray flux from flares falls off rapidly with increasing photon energy, indicating that the number of radiating electrons decreases rapidly with increasing electron energy. Therefore, the energy carried by the accelerated electrons is sensitive to the value of the low-energy cutoff to the electron distribution. The determination of this low-energy cutoff and the total energy in the accelerated electrons is addressed in Section 3.

In the standard thick-target model, the target plasma is assumed to be fully ionized. If the target ionization is not uniform, so that the accelerated electrons stream down to cooler plasma that is partially ionized or un-ionized, the X-ray spectrum is modified. This is addressed in Section 4.

Observations of the radiation from hot flare plasma have shown this plasma to primarily be confined to magnetic loops or arcades of magnetic loops (cf. Aschwanden 2004). The observations also indicate that the heating of this plasma and particle acceleration initially occur in the corona above these hot loops (see Section 12.2 and Fletcher et al. 2011). When the density structure in these loops is typical of active region loops, or at least not highly enhanced above those densities, the highest intensity, thick-target X-ray emission will be from the footpoints of the loops, as is most often observed to be the case. If accelerated electrons alone, unaccompanied by neutralizing ions, stream down the legs of the loop from the

acceleration region to the footpoints, they will drive a co-spatial return current in the ambient plasma to neutralize the high current associated with the downward-streaming electrons. We refer to this primarily downward-streaming distribution of energetic (suprathermal) electrons as an electron beam. The electric field associated with the return current will decelerate electrons in the beam, which can in turn modify the X-ray spectrum from the accelerated electrons. This is addressed in Section 5.

Both the primary beam of accelerated electrons and the return current can become unstable and drive the growth of waves in the ambient plasma. These waves can, in turn, interact with the electron beam and return current, altering the energy and angular distributions of the energetic electrons. These plasma instabilities are discussed in Section 6.

The collisional energy loss rate is greater for lower energy electrons. Therefore, for suprathermal electrons streaming downward to the footpoints of a loop, the footpoint X-ray sources observed at lower energies should be at a higher altitude than footpoint sources observed at higher X-ray energies. The height dispersion of these sources provides information about the height distribution of the plasma density in the footpoints. The spatial resolution of the *Reuven Ramaty High Energy Solar Spectroscopic Imager* (*RHESSI* – see Lin et al. 2002) has made such a study possible. This is described in Section 7. *RHESSI* has observed X-ray sources that move downward from the loop top and then upward from the footpoints during some flares. This source evolution in time is also discussed in Section 7.

If electrons of all energies are simultaneously injected, the footpoint X-ray emission from the slower, lower energy electrons should appear after that from faster, higher energy electrons. The length of this time delay provides an important test for the height of the acceleration region. Longer time delays can result from magnetic trapping of the electrons. The evolution of the thermal plasma in flares can also exhibit time delays associated with the balance between heating and cooling processes. These various time delays and the information they provide are addressed in Section 8.

An important diagnostic of electron acceleration and propagation in flares is the time evolution of the X-ray spectrum during flares. In most flares, the X-ray spectrum becomes harder (flatter, smaller spectral index) and then softer (steeper, larger spectral index) as the X-ray flux evolves from low to high intensity and then back to low intensity. There are notable exceptions to this pattern, however. Spectral evolution is addressed in Section 9.

One of the most important results from the *Yohkoh* mission is the discovery in some flares of a hard (high energy) X-ray source above the top of of the thermal (low energy) X-ray loops. This, together with the *Yohkoh* observations of cusps at the top of flare X-ray loops, provided strong evidence that energy release occurs in the corona above the hot X-ray loops (for some flares, at least). Although several models have been proposed, the origin of these “above-the-looptop” hard X-ray sources is not well understood. We need to determine how their properties and evolution compare to the more intense footpoint hard X-ray sources. These issues are addressed in Section 10.

Radio observations provide another view of accelerated electrons and related flare phenomena. Although radio emission and its relationship to flare X-rays are primarily addressed in White et al. (2011), some intriguing radio observations that bear upon electron acceleration in flares are presented in Section 11.

RHESSI observations of flare X-ray emission have led to substantial progress, but many questions remain unanswered. Part of the progress is that the questions are different from those that were asked less than a decade ago. The primary context for interpreting the X-ray emission from suprathermal electrons is still the thick-target model, but the ultimate goal is to understand how the electrons are accelerated. In Section 12 we summarize and discuss the implications of the X-ray observations for the thick-target model and electron acceleration

mechanisms, and highlight some of the questions that remain to be answered. Implications of these questions for future flare studies are discussed.

2 Thin- and thick-target X-ray emission

As was summarized in Section 1, the electron-ion bremsstrahlung X-rays from a beam of accelerated electrons will be most intense where the density of target ions is highest, as well as where the flux of accelerated electrons is high. The local emission (emissivity) at position $\mathbf{r}$ of photons of energy ε by electrons of energy E is given by the plasma ion density, $n(\mathbf{r})$ ions cm^{-3}, times the electron-beam flux density distribution, $F(E,\mathbf{r})$ electrons cm^{-2} s^{-1} keV^{-1}, times the differential electron-ion bremsstrahlung cross-section, $Q(\varepsilon,E)$ cm^2 keV^{-1}. For simplicity, we do not consider here the angular distribution of the beam electrons or of the emitted photons, topics addressed in Kontar et al. (2011).

The emissivity of the radiation at energy ε from all the electrons in the beam is obtained by integrating over all contributing electron energies, which is all electron energies above the photon energy. The photon flux emitted per unit energy is obtained by integrating over the emitting source volume (V) or, for an imaged source, along the line of sight through the source region. Finally, assuming isotropic emission, the observed spatially integrated flux density of photons of energy ε at the X-ray detector, $I(\varepsilon)$ photons cm^{-2} s^{-1} keV^{-1}, is simply the flux divided by the geometrical dilution factor $4\pi R^2$, where R is the distance to the X-ray detector. Thus,

$$I(\varepsilon) = \frac{1}{4\pi R^2} \int_V \int_\varepsilon^\infty n(\mathbf{r})\, F(E,\mathbf{r})\, Q(\varepsilon,E)\, dE\, dV. \tag{2.1}$$

We refer to $I(\varepsilon)$ as the X-ray flux spectrum, or simply the X-ray spectrum. The spectrum obtained directly from an X-ray detector is generally a spectrum of counts versus energy loss in the detector, which must be converted to an X-ray flux spectrum by correcting for the detector response as a function of photon energy (see, for example, Smith et al. 2002).

Besides increasing the X-ray emission, a high plasma density also means increased Coulomb energy losses for the beam electrons. In a plasma, the bremsstrahlung losses are small compared to the collisional losses to the plasma electrons. For a fully ionized plasma and beam electron speeds much greater than the mean speed of the thermal electrons, the (nonrelativistic) energy loss rate is

$$dE/dt = -(K/E)\, n_e(\mathbf{r})\, \mathrm{v}(E), \tag{2.2}$$

where $K = 2\pi e^4 \Lambda_{ee}$, Λ_{ee} is the Coulomb logarithm for electron-electron collisions, e is the electron charge, $n_e(\mathbf{r})$ is the plasma electron number density, and $\mathrm{v}(E)$ is the speed of the electron (see Brown 1971; Emslie 1978). The coefficient K is usually taken to be constant, although Λ_{ee} depends weakly on the electron energy and plasma density or magnetic field strength, typically falling in the range 20 – 30 for X-ray-emitting electrons. Taking a value of 23 for Λ_{ee}, the energy loss rate in keV s^{-1} or erg s^{-1} with E in keV is numerically determined by

$$K = 3.00 \times 10^{-18} \left(\frac{\Lambda_{ee}}{23}\right) \text{ keV cm}^2 = 4.80 \times 10^{-27} \left(\frac{\Lambda_{ee}}{23}\right) \text{ erg cm}^2. \tag{2.3}$$

Here and in equations to follow, notation such as $(\Lambda_{ee}/23)$ is used to show the scaling of a computed constant (here, K) with an independent variable and the numerical value taken

for the independent variable ($\Lambda_{ee} = 23$ in Equation 2.3). If the plasma is not fully ionized, K also depends on the ionization state (see Section 4.1).

Noting that v$dt = dz$, Equation 2.2 can be simplified to $dE/dN_e = -K/E$, where $dN_e(z) = n_e(z)dz$ and $N_e(z)$ (cm^{-2}) is the plasma electron *column density*. (Here we treat this as a one-dimensional system and do not distinguish between the total electron velocity and the velocity component parallel to the magnetic field.) Hence, the evolution of an electron's energy with column density is simply

$$E^2 = E_0^2 - 2KN_e, \tag{2.4}$$

where E_0 is the initial energy of the electron where it is injected into the target region. For example, a 1 keV electron loses all of its energy over a column density of $1/(2K) = 1.7 \times 10^{17}$ cm^{-2} (for $\Lambda_{ee} = 23$). A 25 keV electron loses 20% of its energy over a column density of 3.8×10^{19} cm^{-2}.

If energy losses are not significant within a spatially unresolved X-ray source region, the emission is called *thin-target*. If, on the other hand, the non-thermal electrons lose all their suprathermal energy within the spatially unresolved source during the observational integration time, the emission is called *thick-target*. We call a model that assumes these energy losses are from Coulomb collisions (equations 2.2 & 2.3) a *collisional thick-target model*. Collisional thick-target models have been applied to flare x-ray/γ-ray emission since the discovery of this emission in 1958 (Peterson & Winckler 1958, 1959).

The maximum information that can be obtained about the accelerated electrons from an X-ray spectrum alone is contained in the *mean electron flux distribution*, the plasma-density-weighted, target-averaged electron flux density distribution (Brown et al. 2003; Kontar et al. 2011). The mean electron flux distribution is defined as

$$\bar{F}(E) = \frac{1}{\bar{n}V} \int_V n(\mathbf{r})\, F(E,\mathbf{r})\, dV \quad \text{electrons cm}^{-2}\,\text{s}^{-1}\,\text{keV}^{-1}, \tag{2.5}$$

where $\bar{n}$ and V are the mean plasma density and volume of the emitting region. As can be seen from Equation 2.1, the product $\bar{n}V\bar{F}$ can, in principle, be deduced with only a knowledge of the bremsstrahlung cross-section, $Q(\varepsilon, E)$. Additional information is required to determine if the X-ray emission is thin-target, thick-target, or something in between. The flux distribution of the emitting electrons and the mean electron flux distribution are equivalent for a homogeneous, thin-target source region.

Equation 2.1 gives the observed X-ray flux in terms of the accelerated electron flux density distribution throughout the source. However, we are interested in the electron distribution injected into the source region, $F_0(E_0, \mathbf{r_0})$, since that is the distribution produced by the unknown acceleration mechanism, including any modifications during propagation to the source region. To obtain this, we need to know how to relate $F(E,\mathbf{r})$ at all locations within the source region to $F_0(E_0, \mathbf{r_0})$. Since we are interested in the X-rays from a spatially integrated, thick-target source region, the most direct approach is to first compute the bremsstrahlung photon yield from a single electron of energy E_0, $v(\varepsilon, E_0)$ photons keV^{-1} per electron (Brown 1971). As long as the observational integration time is longer than the time required for the electrons to radiate all photons of energy ε (i.e., longer than the time required for energy losses to reduce all electron energies to less than ε), the thick-target X-ray spectrum is then given by

$$I_{thick}(\varepsilon) = \frac{1}{4\pi R^2} \int_\varepsilon^\infty \mathscr{F}_0(E_0)\, v(\varepsilon, E_0)\, dE_0, \tag{2.6}$$

where $\mathscr{F}_0(E_0)$ is the electron beam flux distribution (electrons s^{-1} keV^{-1}). $\mathscr{F}_0(E_0)$ is the integral of $F_0(\mathbf{r_0},E_0)$ over the area at the injection site through which the electrons stream into the thick-target region.

The rate at which an electron of energy E radiates bremsstrahlung photons of energy ε is $n(\mathbf{r})\mathrm{v}(E)Q(\varepsilon,E)$. The photon yield is obtained by integrating this over time. Since the electrons are losing energy at the rate dE/dt, the time integration can be replaced by an integration over energy from the initial electron energy E_0 to the lowest energy capable of radiating a photon of energy ε:

$$\nu(\varepsilon,E_0) = \int_{E_0}^{\varepsilon} \frac{n(\mathbf{r})\,\mathrm{v}(E)\,Q(\varepsilon,E)\,dE}{dE/dt}. \tag{2.7}$$

Using Equation 2.2 for dE/dt, Equation 2.6 becomes

$$I_{thick}(\varepsilon) = \frac{1}{4\pi R^2}\frac{1}{\overline{Z}K}\int_{E_0=\varepsilon}^{\infty}\mathscr{F}_0(E_0)\int_{E=\varepsilon}^{E_0} E\,Q(\varepsilon,E)\,dE\,dE_0. \tag{2.8}$$

We have used the relationship $n_e = \overline{Z}n$, where $\overline{Z}\simeq 1.1$ is the ion-species-number-density-weighted (or, equivalently, relative-ion-abundance-weighted) mean atomic number of the target plasma. Thus, the thick-target X-ray flux spectrum does not depend on the plasma density. However, the plasma must be dense enough for the emission to be thick-target, i.e., dense enough for all the electrons to be thermalized in the observation time interval. Integration of Equation 2.2 shows that this typically implies a plasma density $\gtrsim 10^{11}-10^{12}$ cm^{-3} for an observational integration time of 1 s (see Sections 10.4 and 12.1 for more about this). This condition is well satisfied at loop footpoints.

Observed non-thermal X-ray spectra from solar flares can usually be well fitted with a model photon spectrum that is either a single or a double power-law. For a single power-law electron flux distribution of the form $\mathscr{F}(E) = AE^{-\delta}$, the photon spectrum is also well approximated by the power-law form $I(\varepsilon) = I_0\varepsilon^{-\gamma}$. The relationship between the electron and photon spectral indices δ and γ can most easily be obtained from equations 2.1 and 2.8 using the Kramers approximation to the nonrelativistic Bethe-Heitler (NRBH) bremsstrahlung cross section (see Koch & Motz 1959 for bremsstrahlung cross-sections). The NRBH cross-section is given by:

$$Q_{NRBH}(\varepsilon,E) = \frac{\overline{Z^2}Q_0}{\varepsilon E}\ln\left(\frac{1+\sqrt{1-\varepsilon/E}}{1-\sqrt{1-\varepsilon/E}}\right)\quad \mathrm{cm^2\,keV^{-1}}, \tag{2.9}$$

where $Q_0 = 7.90\times10^{-25}$ cm^2 keV and $\overline{Z^2}\simeq 1.4$ is the ion-species-number-density-weighted mean square atomic number of the target plasma. The Kramers approximation to this cross-section is Equation 2.9 without the logarithmic term. The bremsstrahlung cross-section is zero for $\varepsilon > E$, since an electron cannot radiate a photon that is more energetic than the electron. Analytic expressions for the photon flux from both a uniform thin-target source and a thick-target source can be obtained with the Kramers and the NRBH cross-sections when the electron flux distribution has the single-power-law form (Brown 1971; Tandberg-Hanssen & Emslie 1988). The thin-target result also generalizes to the photon flux from a single-power-law mean electron flux distribution.

For a uniform thin-target source and $\mathscr{F}(E) = AE^{-\delta}$,

$$I_{thin}(\varepsilon) = 3.93\times10^{-52}\left(\frac{1\ \mathrm{AU}}{R}\right)^2\left(\frac{\overline{Z^2}}{1.4}\right)NA\beta_{tn}(\delta)\varepsilon^{-(\delta+1)}, \tag{2.10}$$

giving $\gamma_{thin} = \delta + 1$. The photon energy ε is in keV, the distance from the source to the X-ray detector is taken to be one Astronomical Unit (1 AU), a typical value of 1.4 is taken for $\overline{Z^2}$, and N is the ion column density. The power-law-index-dependent coefficient for the NRBH cross-section is

$$\beta_{tn}(\delta) = \frac{B(\delta, 1/2)}{\delta}, \tag{2.11}$$

where $B(x,y)$ is the standard Beta function. In the Kramers approximation, $\beta_{tn}(\delta) = 1/\delta$. Typical values for the ion column density and A, the differential electron flux at 1 keV, are $N = 10^{18}$–10^{20} cm^{-2} and $A = 10^{34}$–10^{38} electrons s^{-1} keV^{-1}.

For a thick-target source region,

$$I_{thick}(\varepsilon) = 1.17 \times 10^{-34} \left(\frac{1\ \mathrm{AU}}{R}\right)^2 \left(\frac{\overline{Z^2}/\overline{Z}}{1.25}\right) \left(\frac{23}{\Lambda_{ee}}\right) A \beta_{tk}(\delta) \varepsilon^{-(\delta-1)}, \tag{2.12}$$

giving $\gamma_{thick} = \delta - 1$. The power-law-index-dependent coefficient for the NRBH cross-section is

$$\beta_{tk}(\delta) = \frac{B(\delta - 2, 1/2)}{(\delta - 1)(\delta - 2)}. \tag{2.13}$$

In the Kramers approximation, $\beta_{tk}(\delta) = 1/[(\delta - 1)(\delta - 2)]$.

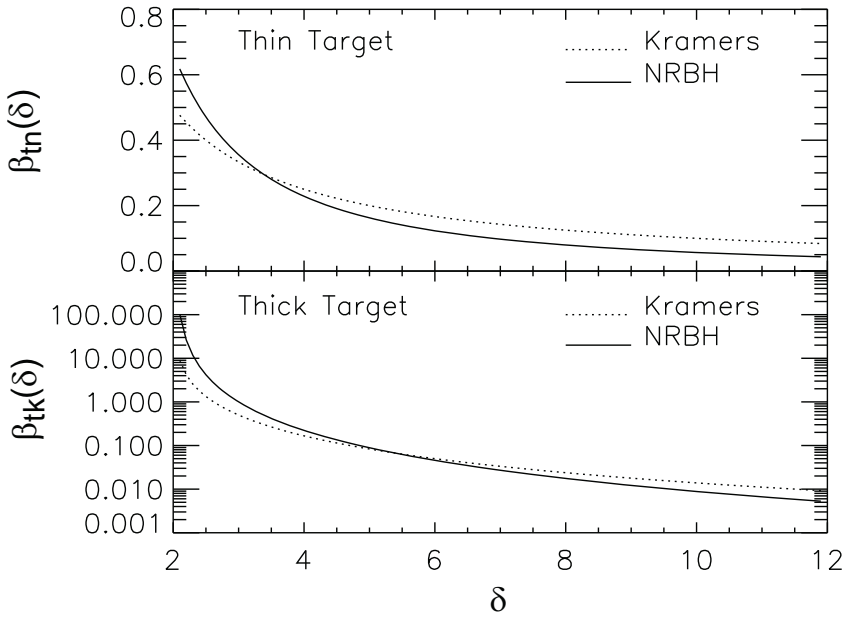

Fig. 2.1 The power-law-index-dependent terms $\beta_{tn}(\delta)$ (equation 2.11) and $\beta_{tk}(\delta)$ (equation 2.13) in the analytic expressions for the thin-target and the thick-target photon flux from a power-law electron flux distribution (equations 2.10 and 2.12). The *solid* curves are for the nonrelativistic Bethe-Heitler bremsstrahlung cross-section and the *dotted* curves are for the Kramers cross-section. Note that the β axis is linear for the thin-target coefficient, and logarithmic for the thick-target coefficient.

The coefficients $\beta_{tn}(\delta)$ and $\beta_{tk}(\delta)$ for both the NRBH and the Kramers cross-sections are plotted as a function of δ in Figure 2.1. The Kramers and NRBH results are equal for

thin-target emission when $\delta \simeq 3.4$, and for thick-target emission when $\delta \simeq 5.4$. For the plotted range of δ, the Kramers approximation can differ from the NRBH result by over 90%. For δ in the range 3–10, the Kramers result can differ from the NRBH result by as much as 76% and 57% for thin- and thick-target emission, respectively.

It is important to recognize that the above power-law relationships are only valid if the electron *flux density distribution*, $F(\mathbf{r},E)$ electrons cm^{-2} s^{-1} keV^{-1}, or the electron *flux distribution*, $\mathscr{F}(E)$ electrons s^{-1} keV^{-1}, is assumed to have a power-law energy dependence. It is sometimes convenient to work with the electron *density distribution*, $f(\mathbf{r},E)$ (electrons cm^{-3} keV^{-1}), rather than the flux density distribution, especially when considering thin-target emission alone or comparing X-ray spectra with radio spectra. The flux density and density distributions are related through $F(\mathbf{r},E) = f(\mathbf{r},E)\mathrm{v}(E)$. If the electron density distribution rather than the flux or flux density distribution is assumed to have a power-law index δ', so that $f(\mathbf{r},E) \propto E^{-\delta'}$, the relationships between this power-law index and the photon spectral index become $\gamma_{thin} = \delta' + 0.5$ and $\gamma_{thick} = \delta' - 1.5$.

The simple power-law relationships are *not valid* if there is a break or a cutoff in the electron distribution at an energy less than $\sim$2 orders of magnitude above the photon energies of interest. Since all electrons with energies above a given photon energy ε contribute to the bremsstrahlung at that photon energy, for the power-law relationships to be valid the break energy must be high enough that the deficit (or excess) of electrons above the break energy does not significantly affect the photon flux at energy ε. The power-law relationship is typically not accurate until photon energies one to two orders of magnitude below the break energy, depending on the steepness of the power-law electron distribution (see Figures 9 & 10 of Holman 2003). Thus, for example, these relationships are not correct for the lower power-law index of a double power-law fit to a photon spectrum at photon energies within about an order of magnitude below the break energy in the double power-law electron distribution. Equation 2.1 or 2.8 can be used to numerically compute the X-ray spectrum from an arbitrary flux distribution in electron energy.

When electrons with kinetic energies approaching or exceeding 511 keV significantly contribute to the radiation, the relativistic Bethe-Heitler bremsstrahlung cross-section (Equation 3BN of Koch & Motz 1959) or a close approximation (Haug 1997) must be used. Haug (1997) has shown that the maximum error in the NRBH cross-section relative to the relativistic Bethe-Heitler cross section becomes greater than 10% at electron energies of 30 keV and above. Numerical computations using the relativistic Bethe-Heitler cross-section have been incorporated into the *RHESSI* spectral analysis software (OSPEX) for both thin- and thick-target emission from, in the most general case, a broken-power-law electron flux distribution with both low- and high-energy cutoffs (the functions labeled "thin" and "thick" using the IDL programs `brm_bremspec.pro` and `brm_bremthick.pro` – see Holman 2003). Faster versions of these programs are now available in OSPEX and are currently labeled "thin2" and "thick2" and use the IDL programs `brm2_thintarget.pro` and `brm2_thicktarget.pro`.

The analytic results based on the NRBH cross-section have been generalized to a broken-power-law electron flux distribution with cutoffs by Brown et al. (2008). They find a maximum error of 35% relative to results obtained with the relativistic Bethe-Heitler cross-section for the range of parameters they consider. These results provide the fastest method for obtaining thin- and thick-target fits to X-ray spectra in the *RHESSI* spectral analysis software, where they are labeled "photon_thin" and "photon_thick" and use the IDL programs `f_photon_thin.pro` and `f_photon_thick.pro`.

3 Low-energy cutoffs and the energy in non-thermal electrons

One of the most important aspects of the distribution of accelerated electrons is the low-energy cutoff. The acceleration of charged particles out of the thermal plasma typically involves a competition between the collisions that keeps the particles thermalized and the acceleration mechanism. The particles are accelerated out of the tail of the thermal distribution, down to the lowest particle energy for which the acceleration mechanism can overcome the collisional force. Thus, the value of the low-energy cutoff can provide information about the force of the acceleration mechanism. More generally, as discussed below, the electron distribution must have a low-energy cutoff (1) so that the number and energy flux of electrons is finite and reasonable, and (2) because electrons with energies that are not well above the thermal energy of the plasma through which they propagate will be rapidly thermalized. Knowledge of the low-energy cutoff and its evolution during a flare is critical to determining the energy flux and energy in non-thermal electrons and, ultimately, the efficiency of the acceleration process.

3.1 Why do we need to determine the low-energy cutoff of non-thermal electron distributions?

An important feature of the basic thick-target model is that the photon spectrum $I(\varepsilon)$ is directly determined by the injected electron flux distribution $\mathscr{F}_0(E_0)$. As can be seen from Equation 2.8, no additional parameters such as source density or volume need to be determined. Consequently, by integrating over all electron energies, we can also determine the total flux of non-thermal electrons, N_{nth} electrons s^{-1}, the power in non-thermal electrons, P_{nth} erg s^{-1}, and, integrating over time, the total number of, and energy in, non-thermal electrons.

The total non-thermal electron number flux and power are computed as follows:

$$N_{nth} = \int_{E_c}^{+\infty} \mathscr{F}_0(E_0)\, dE_0 = \frac{A}{\delta - 1} {E_c}^{-\delta+1} \quad \text{electrons s}^{-1} \tag{3.1}$$

$$P_{nth} = \kappa_E \int_{E_c}^{+\infty} E_0 \cdot \mathscr{F}_0(E_0)\, dE_0 = \frac{\kappa_E A}{\delta - 2} {E_c}^{-\delta+2} \quad \text{erg s}^{-1} \tag{3.2}$$

The last expression in each equation is the result for a power-law electron flux distribution of the form $\mathscr{F}_0(E_0) = A \cdot E_0^{-\delta}$. The constant $\kappa_E = 1.60 \times 10^{-9}$ is the conversion from keV to erg. E_c is a low-energy cutoff to the electron flux distribution. These expressions are valid and finite for $\delta > 2$ and $E_c > 0$. We call this form of low-energy cutoff a *sharp low-energy cutoff*. An electron distribution that continues below a transition energy E_c that has a positive slope, is flat, or in general has a spectral index $\delta_{low} < 1$ also provides finite electron and energy fluxes, but these fluxes are somewhat higher than those associated with the sharp low-energy cutoff.

For this single-power-law electron flux distribution with a sharp low-energy cutoff, the non-thermal *power* (erg s^{-1}), and ultimately the non-thermal *energy* (erg), from the power-law electron flux distribution depends on only three parameters: δ, A, and E_c. Observations indicate that δ is greater than 2 (Dennis 1985; Lin & Schwartz 1987; Winglee et al. 1991; Holman et al. 2003). Hence, were $E_c = 0$, the integral would yield an infinite value, a decidedly unphysical result! Therefore, the power-law electron distribution cannot extend all the way to zero energy with the same or steeper slope, and some form of *low-energy cutoff* in

the accelerated electron spectrum must be present. As we will see, the determination of the energy at which this cutoff occurs is not a straightforward process, but it is the single most important parameter to determine (as the other two are generally more straightforward to determine – see Section 2 and Kontar et al. 2011). For example, with $\delta = 4$ (typical during the peak time of strong flares), a factor of 2 error in E_c yields a factor of 4 error in P_{nth}. For larger δ (as found in small flares, or rise/decay phases of large flares), such an error quickly leads to an order of magnitude (or even greater) difference in the injected power P_{nth} and in the total energy in the non-thermal electrons accelerated during the flare!

3.2 Why is the low-energy cutoff difficult to determine?

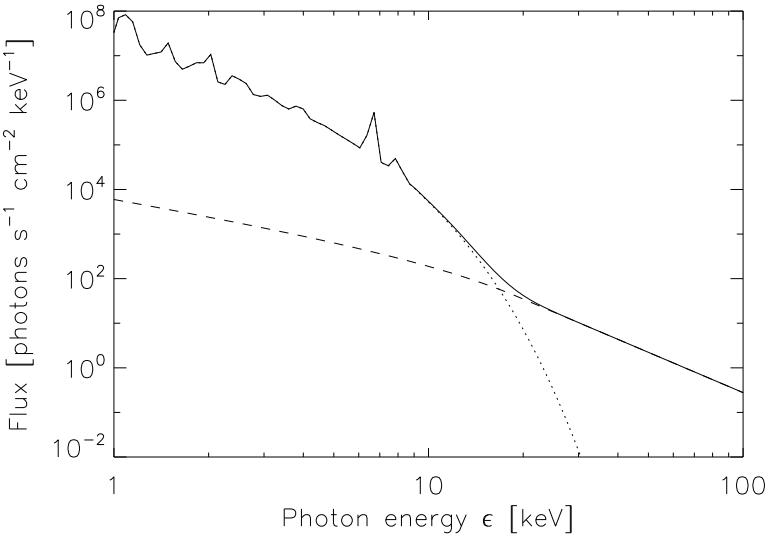

Fig. 3.1 Typical full-Sun flare spectrum. *Dashed:* Nonthermal thick-target spectrum from an accelerated electron distribution with δ=4, and a low-energy cutoff of 20 keV. *Dotted:* Thermal spectrum, from a plasma with temperature $T = 20$ MK and emission measure $EM = 10^{49}$ cm^{-3}. *Solid:* Total radiated spectrum. The multiple peaks in the thermal spectrum are from spectral lines, as observed by an instrument with ~ 1 keV spectral resolution.

The essence of the problem in many flare spectra is summarized in Figure 3.1: the non-thermal power-law is well-observed above $\sim$20 keV, but any revealing features that it might possess at lower energies, such as a low-energy cutoff, are masked by the thermal emission.

Even if a spectrum does show a flattening at low energies that could be the result of a low-energy cutoff, other mechanisms that could produce the flattening must be ruled out (see Section 3.4). The low-energy cutoff has the characteristic feature, determined by the photon energy dependence of the bremsstrahlung cross-section (see Equation 2.9), that the X-ray spectrum eventually approaches a spectral index of $\gamma \approx 1$ at low energies (cf. Holman 2003). It is currently impossible, however, to observe a flare spectrum to low enough photon

energies to see that it does indeed become this flat. Generally we can only hope to rule out the other mechanisms based on additional data and detailed spectral fits.

3.3 What is the shape of the low-energy cutoff, and how does it impact the photon spectrum and P_{nth}?

Bremsstrahlung photon spectra are obtained from convolution integrals over the electron flux distribution (equations 2.1 and 2.8). Hence, features in an electron distribution are smoothed out in the resulting photon spectrum (see, e.g., Brown et al. 2006).

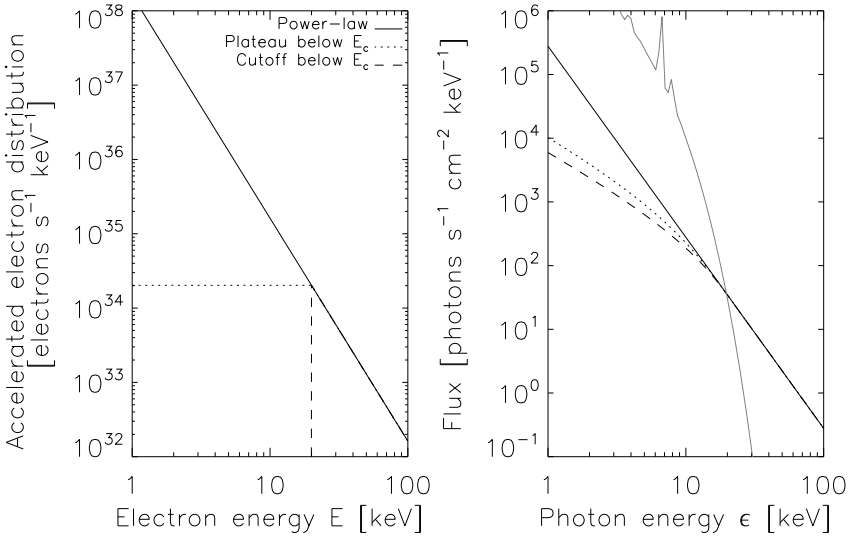

Fig. 3.2 Different shapes of low-energy cutoff in the injected electron distribution *(left)* lead to slightly different photon spectra *(right)*. The cutoff/turnover electron energy is E_c=20 keV. The thin curve in the right panel demonstrates how the cutoff can be masked by emission from thermal plasma. See also Holman (2003) for a thorough discussion of bremsstrahlung spectra generated from electron power-laws with cutoff.

As can be seen in Figure 3.2, both a sharp cutoff at E_c and a "turnover" (defined here to be a constant $F_0(E)$ below E_c, a "plateau") in the injected electron distribution lead to similar thick-target photon spectra. This subtle difference is difficult to discriminate observationally, and the problem is compounded by the dominance of the thermal component at low energies.

A sharp cutoff would lead to plasma instabilities that should theoretically flatten the distribution around and below the cutoff within microseconds (see Section 6). On the other hand, the electron flux distribution below the cutoff must be flatter than E^{-1}, as demonstrated by Equation 3.1, or the total electron number flux would be infinite. Having a constant value for the distribution below E_c (turnover case) seems like a reasonable middle ground and approximates a quasilinearly relaxed electron distribution (Section 6; Krall & Trivelpiece 1973, Chapter 10). Coulomb collisional losses, on the other hand, yield an electron distribution that increases linearly at low energies (see Figure 3.3), leading to a photon spectrum between the sharp cutoff case and the turnover case.

Notice that the photon spectra actually flatten gradually to the spectral index of 1 at low energies from the spectral index of $\gamma = \delta + 1$ at E_c and higher energies. Below E_c, it is *not* a power-law. Fitting a double power-law model photon spectrum, and using the break (i.e., kink) energy as the low-energy cutoff typically leads to a large error in E_c (e.g., Gan et al. 2001; Saint-Hilaire & Benz 2005), and hence to an even larger error in P_{nth}.

In terms of the energetics, Saint-Hilaire & Benz (2005) have shown that the choice of an exact shape for the low-energy cutoff as a model is not dramatically important. For a fixed cutoff energy, from Equation 3.2 it can be shown that the ratio of the power in the turnover model to the power in the sharp cutoff model without the flat component below the cutoff energy is $\delta/2$. In obtaining spectral fits, however, the turnover model gives higher cutoff energies than the sharp cutoff model. Using simulations, Saint-Hilaire & Benz (2005) found that assuming either a sharp cutoff model or a turnover model led to differences in P_{nth} typically less than $\sim$20%. Hence, the sharp cutoff, being the simplest, is the model of choice for computing flare energetics. Nevertheless, knowing the shape of the low-energy cutoff would not only yield more accurate non-thermal energy estimates, but would be a source of information on the acceleration mechanism and/or propagation effects.

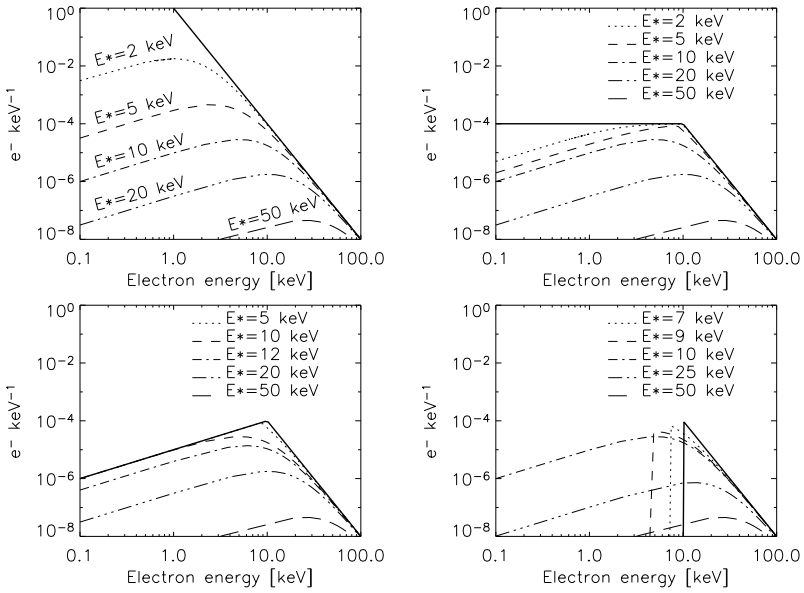

Fig. 3.3 The four plots show the Coulomb-collisional evolution with column density of an injected electron distribution (*thick, solid line*). For the simple power-law case (*upper left*), the low-energy end of the distribution becomes linear, and the peak of the distribution is found at $E_{peak} = E_*/\sqrt{\delta}$, where δ is the injected distribution power-law spectral index (δ=4 in the plots), and $E_* = \sqrt{2K \cdot N_*}$ is the initial energy that electrons must possess in order not to be fully stopped by a column density N_* (Equation 2.4). When a low-energy cutoff is present, the peak of the distribution is seen to first decrease in energy until E_* exceeds the cutoff energy (from Saint-Hilaire 2005).

Spectral inversion methods have recently been developed for deducing the *mean electron flux distribution* (Equation 2.5) from X-ray spectra (Johns & Lin 1992; Brown et al. 2003, 2006). A spectral "dip" has been found just above the presumed thermal component in some deduced mean electron flux distributions that may be associated with a low-energy cutoff

(e.g., Piana et al. 2003). In the collisional thick-target model, the slope of the high-energy "wall" of this dip should be linear or flatter, with a linear slope indicating the absence of emitting electrons in the injected electron distribution at the energies displaying this slope. Kontar & Brown (2006a) have found evidence for slopes that are steeper than linear, but their spectra were not corrected for photospheric albedo (see Section 3.5). Finding and understanding these dips is a crucial element for gaining an understanding of the low-energy properties of flare electron distributions (see Kontar et al. 2011).

Emslie (2003) has pointed out that the non-thermal electron distribution could seamlessly merge into the thermal distribution, removing the need for a low-energy cutoff. As was shown by Holman et al. (2003) for SOL2002-07-23T00:35 (X4.8), however, merger of the electron distribution into the typically derived $\sim$10–30 MK thermal flare plasma generally implies an exceptionally high energy in non-thermal electrons. Thus, for a more likely energy content, a higher low-energy cutoff or a hotter plasma would need to be present in the target region. Any emission from this additional "hot core," because of its much lower emission measure, is likely to be masked by the usual $\sim$10–30 MK thermal emission. This merger of the non-thermal electron distribution into the thermal tail in the target region does not remove the need for a low-energy cutoff in the electrons that escape the acceleration region, however.

This section has dealt with the shape of the low-energy cutoff under the assumptions that the X-ray photon spectra are not altered by other mechanisms and that the bremsstrahlung emission is isotropic. The next section lists the important caveats to these assumptions, and their possible influence in the determination of the low-energy cutoff to the electron flux distribution.

3.4 Important caveats

As previously discussed, apparently minor features in the bremsstrahlung photon spectrum can have substantial implications for the mean electron flux and, consequently, the injected electron distribution. This means that unknown or poorly-understood processes that alter the injected electron distribution (propagation effects, for example) or the photon spectrum (including instrumental effects) can lead to significant errors in the determination of the low-energy cutoff. Known processes that affect the determination of the low-energy cutoff are enumerated below.

1. Detector pulse pileup effects (Smith et al. 2002), if not properly corrected for, can introduce a flattening of the spectrum toward lower energies that simulates the flattening resulting from a low-energy cutoff.
2. The contribution of Compton back-scattered photons (photospheric albedo) to the measured X-ray spectrum can simulate the spectral flattening produced by a low-energy cutoff. Kašparová et al. (2005) have shown that the dip in a spectrum from SOL2002-08-20T08:25 (M3.4) becomes statistically insignificant when the spectrum is corrected for photospheric albedo (also see Kontar et al. 2011). Kašparová et al. (2007) show that spectra in the 15–20 keV energy band tend to be flatter near disk center when albedo from isotropically emitted photons is not taken into account, further demonstrating the importance of correcting for photospheric albedo.
3. The assumed differential cross-section and electron energy loss rate can influence the results (for a discussion of this, see Saint-Hilaire & Benz 2005). In some circumstances, a contribution from recombination radiation may significantly change the results (Brown et al. 2010; also see Kontar et al., 2011).

4. Anisotropies in the electron beam directivity and the bremsstrahlung differential cross-section can significantly alter the X-ray spectrum (Massone et al. 2004).
5. Non-uniform target ionization (the fact that the chromosphere's ionization state varies with depth, see Section 4) can introduce a spectral break that may be confused with the break associated with a low-energy cutoff.
6. Energy losses associated with a return current produce a low-energy flattening of the X-ray spectrum (Section 5). This is a low-energy "cutoff" in the electron distribution injected into the thick target, but it is produced between the acceleration region and the emitting source region.
7. A non-power-law distribution of injected electrons or significant evolution of the injected electron distribution during the observational integration time could affect the deduced value of the low-energy cutoff.

For all the above reasons, the value of the low-energy cutoff in the injected electron flux distribution has not been determined with any degree of certainty except perhaps in a few special cases. Even less is known about the shape of the low-energy cutoff. The consensus in the solar physics community for now is to assume the simplest case, a sharp low-energy cutoff. Existing studies, presented in the next section, tend to support the adequacy of this assumption for the purposes of estimating the total power and energy in the accelerated electrons.

3.5 Determinations of E_c and electron energy content from flare data

Before *RHESSI*, instruments did not cover well (if at all) the $\sim$10–40 keV photon energies where the transition from thermal emission to non-thermal emission usually occurs. Researchers typically assumed an arbitrary low-energy cutoff at a value at or below the instrument's observing range (one would talk of the "injected power in electrons above E_c keV" instead of the total non-thermal power P_{nth}). An exception is Nitta et al. (1990). They argued that spectral flattening observed in two flares with the *Solar Maximum Mission* and *Hinotori* indicated a cutoff energy of $\gtrsim$50 keV. Also, Gan et al. (2001) interpreted spectral breaks at $\sim$80 keV in *Compton Gamma-Ray Observatory (CGRO)* flare spectra as the low-energy cutoff in estimating flare energetics, resulting in rather small values for the non-thermal energy in the analyzed flares. The relatively low resolution of the spectra from these instruments prevented the quantitative evaluation of any spectral flattening toward lower energies, however.

The only high-resolution flare spectral data before the launch of *RHESSI* was the balloon data of Lin et al. (1981) for SOL1980-06-27T16:17 (M6.7) along with $\sim$25 microflares observed during the same balloon flight. Benka & Holman (1994) applied a direct electric field electron acceleration model to the SOL1980-06-27 flare data. They derived, along with other model-related parameters, the time evolution of the critical energy above which runaway acceleration occurs – the model equivalent to the low-energy cutoff. They found this critical energy to range from $\sim$20–40 keV.

It is now possible in most cases to obtain a meaningful upper limit on E_c, thanks to *RHESSI*'s high-spectral-resolution coverage of the 10–40 keV energy range and beyond. Holman et al. (2003), Emslie et al. (2004), and Saint-Hilaire & Benz (2005), in determining the low-energy cutoff, obtained the "highest value for E_c that still fits the data." In many solar flare spectra, because of the dominance of radiation from thermal plasma at low energies, a range of values for E_c fit the data equally well, up to a certain critical energy, above

which the χ^2 goodness-of-fit parameter becomes unacceptably large. The low-energy cutoff is taken to be equal to this critical value. This upper limit on the cutoff energy results in a lower limit for the non-thermal power and energy. The results obtained for the maximum value of E_c were typically in the 15–45 keV range, although late in the development of SOL2002-07-23T00:35 (X4.8) some values as high as ∼80 keV were obtained for E_c. The minimum non-thermal energies thus determined were comparable to or somewhat larger than the calculated thermal energies.

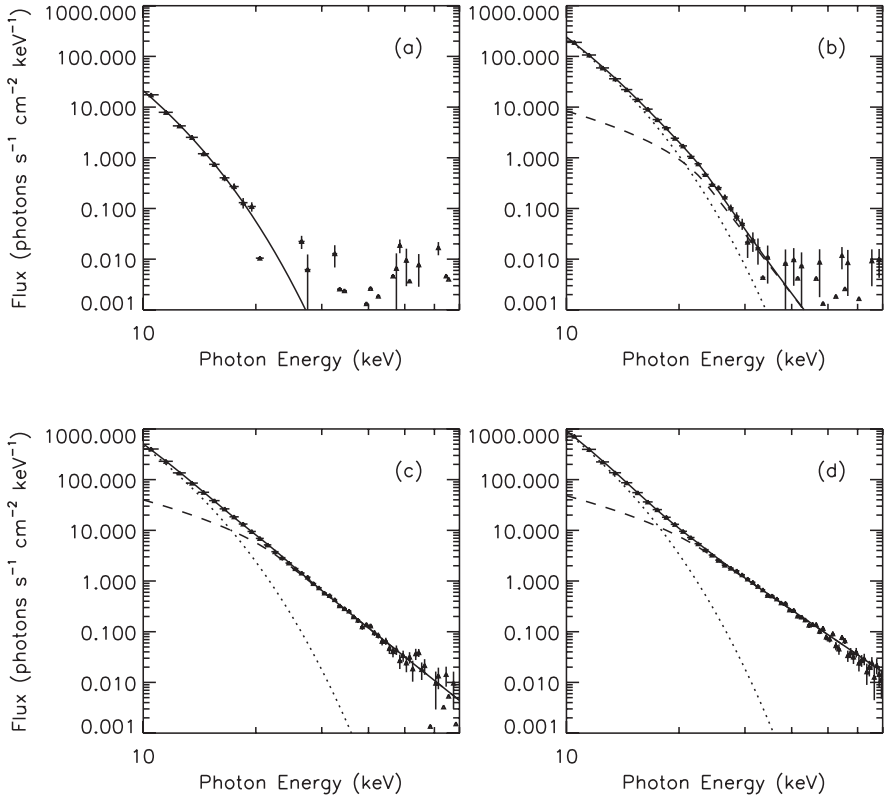

Fig. 3.4 *RHESSI* spatially integrated spectra in four time intervals during SOL2002-04-15T03:55 (M1.2). (a) Spectrum at 23:06:20–23:06:40 UT (early rise phase). (b) Spectrum at 23:09:00-23:09:20 UT (just before impulsive phase). (c) Spectrum at 23:10:00–23:10:20 UT (soon after the impulsive rise). (d) Spectrum at 23:11:00–23:11:20 UT (at the hard X-ray peak). The plus signs with error bars represent the spectral data. The lines represent model spectral fits: the dashed lines are non-thermal thick-target bremsstrahlung, the dotted lines are thermal bremsstrahlung, and the solid lines are the summation of the two (from Sui et al. 2005a).

One of the best determinations of the low-energy cutoff so far was obtained by Sui et al. (2005a). They complemented the spatially-integrated spectral data for the SOL2002-04-15T03:55 (M1.2) limb flare with imaging and lightcurve information. Four spectra from this flare are shown in Figure 3.4. The earliest spectrum, before the impulsive rise of the higher energy X-rays, was well fitted with an isothermal model. The last spectrum, from the time of the hard X-ray peak, clearly shows a thermal component below ∼20 keV. Of

particular interest is the second spectrum, showing both thermal and non-thermal fit components. As a consequence of the flattening of the isothermal component at low energies, the low-energy cutoff to the non-thermal component cannot extend to arbitrarily low energies without exceeding the observed emission. This places a tight constraint on the value of the low-energy cutoff. The additional requirement that the time evolution of the derived temperature and emission measure of the thermal component be smooth and continuous throughout the flare constrains the value at other times. Applying the collisional thick-target model with a power-law distribution of injected electrons, they found the best cutoff value to be $E_c = 24 \pm 2$ keV (roughly constant throughout the flare). The energy associated with these non-thermal electrons was found to be comparable to the peak energy in the X-ray-emitting thermal plasma, but an order of magnitude greater than the kinetic energy of the associated coronal mass ejection (CME) (Sui et al. 2005b). This contrasts with results obtained for large flares, where the minimum energy in non-thermal electrons is typically found to be less than or on the order of the energy in the CME (e.g., Emslie et al. 2004).

The importance of correcting for the distortion of spectra by albedo was revealed by a search for low-energy cutoffs in a sample of 177 flares with relatively flat spectra ($\gamma \leq 4$) between 15 and 20 keV (Kontar et al. 2008a). Spectra can be significantly flattened by the presence of albedo photons in this energy range. The X-ray spectra, integrated over the duration of the impulsive phase of the flares, were inverted to obtain the corresponding mean electron flux distributions. Eighteen of the flares showed significant dips in the mean electron flux distribution in the 13-19 keV electron energy range that might be associated with a low-energy cutoff (see Section 3.3). However, when the X-ray spectra were corrected for albedo from isotropically emitted X-rays, all of the dips disappeared. Therefore, the authors concluded that none of these flare electron distributions had a low-energy cutoff above 12 keV, the lowest electron energy in their analysis.

Low-energy cutoffs were identified in the spectra of a sample of *early impulsive flares* observed by *RHESSI* in 2002 (Sui et al. 2007). Early impulsive flares are flares in which the $>$25 keV hard X-ray flux increase is delayed by less than 30 s after the flux increase at lower energies. The pre-impulsive-phase heating of plasma to X-ray-emitting temperatures is minimal in these flares, allowing the nonthermal part of the spectrum to be observed to lower energies. In the sample of 33 flares, 9 showed spectral flattening at low energies in spectra obtained throughout the duration of each flare with a 4 s integration time. After correcting for the albedo from isotropically emitted X-rays, the flattening in 3 of the 9 flares, all near Sun center, disappeared. The flattening that persisted in the remaining 6 flares was consistent with that produced by a low-energy cutoff. The values derived for the low-energy cutoff ranged from 15 to 50 keV. The authors found the evolution of the spectral break and the corresponding low-energy cutoff in these flares to be correlated with the non-thermal hard X-ray flux. Further studies are needed to assess the significance of this correlation.

Low-energy cutoffs with values exceeding 100 keV were identified in the spectra of the large flare SOL2005-01-19T08:22 (X1.3) (Warmuth et al. 2009). The hard X-ray light curve of this flare consisted of multiple peaks that have been interpreted as quasi-periodic oscillations driven by either magnetoacoustic oscillations in a nearby loop (Nakariakov et al. 2006) or by super-Alfvénic beams in the vicinity of the reconnection region (Ofman & Sui 2006). The high low-energy cutoffs were found in the last major peak of the series of hard X-ray peaks. Unlike the earlier peaks, this peak was also unusual in that it was not accompanied by the Neupert effect (see Section 8.3), consistent with the high values of the low-energy cutoff, and it exhibited soft-hard-harder rather than soft-hard-soft spectral evolution (see Section 9.1). A change in the character of the observed radio emission and movement of one of the two hard X-ray footpoints into a region of stronger photospheric magnetic field were

also observed at the time of this peak. These changes suggest a strong connection between large-scale flare evolution and electron acceleration.

4 Nonuniform ionization in the thick-target region

In the interpretation of hard X-ray (HXR) spectra in terms of the thick-target model, one effect which has been largely ignored until recently is that of varying ionization along the path of the thick-target beam. As first discussed by Brown (1973), the decrease of ionization with depth in the solar atmosphere reduces long-range collisional energy losses. This enhances the HXR bremsstrahlung efficiency there, elevating the high energy end of the HXR spectrum by a factor of up to 2.8 above that for a fully ionized target. The net result is that a power-law electron spectrum of index δ produces a photon spectrum of index $\gamma = \delta - 1$ at low and high energies (see Equation 2.12), but with $\gamma < \delta - 1$ in between. The upward break, where the spectrum begins to flatten toward higher energies, occurs at fairly low energies, probably masked in measured spectra by the tail of the thermal component. The downward knee, where the spectrum steepens again to $\gamma = \delta - 1$, occurs in the few deka-keV range, depending on the column depth of the transition zone. Thus, the measured X-ray spectrum may show a flattening similar to that expected for a low-energy cutoff in the electron distribution.

4.1 Electron energy losses and X-ray emission in a nonuniformly ionized plasma

The collisional energy-loss cross-section $Q_c(E)$ is dependent on the ionization of the background medium. Flare-accelerated electron beams can propagate in the fully ionized corona as well as in the partially ionized transition region and chromosphere.. Following Hayakawa & Kitao (1956) and Brown (1973), the cross-section $Q_c(E)$ can be written for a hydrogen plasma ionization fraction x

$$Q_c(E) = \frac{2\pi e^4}{E^2}\left(x\Lambda_{ee} + (1-x)\Lambda_{eH}\right) = \frac{2\pi e^4}{E^2}\Lambda\left(x+\lambda\right), \tag{4.1}$$

where e is the electronic charge, Λ_{ee} the electron-electron logarithm for fully ionized media and Λ_{eH} is an effective Coulomb logarithm for electron-hydrogen atom collisions. Numerically $\Lambda_{ee} \simeq 20$ and $\Lambda_{eH} \simeq 7.1$, so $\Lambda = \Lambda_{ee} - \Lambda_{eH} \simeq 12.9$ and $\lambda = \Lambda_{eH}/\Lambda \simeq 0.55$.

Then, in a hydrogen target of ionization level $x(N)$ at column density $N(z)$, the energy loss equation for electron energy E is (cf. Equation 2.2)

$$\frac{dE}{dN} = -\frac{2\pi e^4 \Lambda}{E}(\lambda + x(N)) = -\frac{K'}{E}(\lambda + x(N)), \tag{4.2}$$

where $K' = 2\pi e^4 \Lambda = (\Lambda/\Lambda_{ee})K \simeq 0.65K$.

The energy loss of a given particle with initial energy E_0 depends on the column density $N(z) = \int_0^z n(z')dz'$, so the electron energy at a given distance z from the injection site can be written $E^2 = E_0^2 - 2K'M(N(z))$ (cf. Equation 2.4), where

$$M(N(z)) = \int_0^{N(z)} (\lambda + x(N'))dN' \tag{4.3}$$

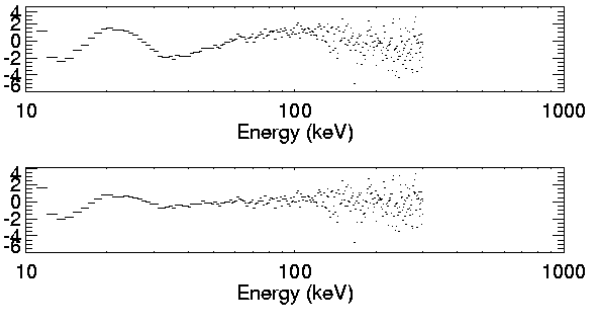

Fig. 4.1 Photon spectrum residuals, normalized by the statistical error for the spectral fit, for the time interval 00:30:00 – 00:30:20 UT, 2002-July-23, for (*upper panel*) an isothermal Maxwellian plus a power-law and (*lower panel*) an isothermal Maxwellian plus the nonuniform ionization spectrum with $\delta = 4.24$ and $E_* = 53$ keV (from Kontar et al. 2003).

is the "effective" ionization-weighted collisional column density.

The fractional atmospheric ionization x as a function of column density N (cm^{-2}) changes from 1 to near 0 over a small spatial range in the solar atmosphere. Therefore, to lowest order, $x(N)$ can be approximated by a step function $x(N) = 1$ for $N < N_*$, and $x(N) = 0$ for $N \geq N_*$. This gives $M(N) = (\lambda + 1)N$ for $N < N_*$ and $M(N) = N_* + \lambda N$ for $N \geq N_*$. Electrons injected into the target with energies less than $E_* = \sqrt{2K'(\lambda+1)N_*} = \sqrt{2KN_*}$ experience energy losses and emit X-rays in the fully ionized plasma with $x = 1$, as in the standard thick-target model. Electrons injected with energies higher than E_* lose part of their energy and partially emit X-rays in the un-ionized ($x = 0$), or, more generally, partially ionized plasma.

We can deduce the properties of the X-ray spectrum by substituting Equation 4.2 into Equation 2.7 (with $dN = nvdt$) and comparing $I_{thick}(\varepsilon)$ from Equation 2.6 with $I_{thick}(\varepsilon)$ from Equation 2.8. We see that for the nonuniformly ionized case the denominator in the inner integral now contains $\lambda + x(N)$ and K is replaced with K'. In the step-function model for $x(N)$, photon energies greater than or equal to $\varepsilon_* = E_*$ are emitted by electrons in the un-ionized plasma with $E \geq E_*$. Since $\lambda + x(N)$ has the constant value λ, the thick-target power-law spectrum is obtained (for injected power-law spectrum), but the numerical coefficient contains $K'\lambda = 2\pi e^4 \Lambda_{eH}$ instead of K. At photon energies far enough below ε_* that the contribution from electrons with $E \geq E_*$ is negligible, $\lambda + x(N) = \lambda + 1$ and the numerical coefficient contains $(\lambda + 1)K' = K$. The usual thick-target spectral shape and numerical coefficient are recovered. The ratio of the amplitude of the high-energy power-law spectrum to the low-energy power-law spectrum is $(\lambda + 1)/\lambda \simeq 2.8$. The photon energy $\varepsilon_*(\mathrm{keV}) \simeq 2.3 \times 10^{-9} \sqrt{\mathrm{N}_*(\mathrm{cm}^{-2})}$, between where the photon spectrum flattens below the high-energy power law and above the low-energy power law, determines the value of the column density where the plasma ionization fraction drops from 1 to 0.

4.2 Application to flare X-ray spectra

The step-function nonuniform ionization model was used by Kontar et al. (2002, 2003) to fit photon spectra from five flares. They assume a single power-law distribution of injected

electrons with power-law index δ and approximate the bremsstrahlung cross-section with the Kramers cross-section. First, they fit the spectra to the sum of a thermal Maxwellian at a single temperature T plus a single power law of index γ. For SOL2002-07-23T00:35 (X4.8) (Kontar et al. 2003) they limit themselves to deviations from a power law in the non-thermal component of the spectrum above ∼40 keV. The top panel of Figure 4.1 shows an example of such deviations, which represent significant deviations from the power-law fit. These deviations are much reduced by replacing the power law with the spectrum from the nonuniform ionization model, with the minimum rms residuals obtained for values of $\delta =$ 4.24 and $E_* = 53$ keV (Figure 4.1, bottom panel). The corresponding minimum (reduced) χ^2 value obtained for the best fit to the X-ray spectrum (10–130 keV) dropped from 1.4 for the power-law fit to 0.8 for the nonuniform ionization fit. There are still significant residuals present in the range from 10 to 30 keV; these might be due to photospheric albedo or the assumption of a single-temperature thermal component.

By assuming that the main spectral feature observed in a hard X-ray spectrum is due to the increased bremsstrahlung efficiency of the un-ionized chromosphere, allowance for nonuniform target ionization offers an elegant direct explanation for the shape of the observed hard X-ray spectrum and provides a measure of the location of the transition region. Table 4.1 shows the best fit parameters derived for the four flare spectra analyzed by Kontar et al. (2002). The last column shows the ratio of the minimum χ^2 value obtained from the nonuniform ionization fit to the minimum χ^2 value obtained from a uniform ionization (single power-law) fit to the non-isothermal part of the spectrum. The nonuniform ionization model fits clearly provide substantially better fits than single power-law fits.

Table 4.1 Best fit nonuniformly ionized target model parameters for a single power-law $\mathscr{F}_0(E_0)$, the equivalent N_* (energy range 20-100 keV), and the ratio of $\chi^2_{nonuni}/\chi^2_{uni}$ (from Kontar et al. 2002)

Date	Time, UT	kT(keV)	δ	E_* (keV)	N_* (cm^2)	$\chi^2_{nonuni}/\chi^2_{uni}$
20 Feb 2002	11:06	1.47	5.29	37.4	2.7×10^{20}	0.032
17 Mar 2002	19:27	1.27	4.99	24.4	1.1×10^{20}	0.047
31 May 2002	00:06	2.02	4.15	56.2	6.1×10^{20}	0.041
1 Jun 2002	03:53	1.45	4.46	21.0	8.4×10^{19}	0.055

Values of the fit parameters kT (keV), δ and E_* as a function of time for SOL2002-07-23T00:35 (X4.8) , together with the corresponding value of $N_*(\mathrm{cm}^{-2}) \simeq 1.9 \times 10^{17} E_*(\mathrm{keV})^2$ were obtained by Kontar et al. (2003). The results (Figure 4.2) demonstrate that the thermal plasma temperature rises quickly to a value $\simeq 3$ keV and decreases fairly slowly thereafter. The injected electron flux spectral index δ follows a general "soft-hard-soft" trend and qualitatively agrees with the time history of the simple best-fit power-law index γ (Holman et al. 2003). E_* rises quickly during the first minute or so from ∼40 keV to ∼70 keV near the flare peak and thereafter declines rather slowly. The corresponding values of N_* are ∼2-5 $\times 10^{20}$ cm^{-2}.

The essential results of these studies are that (1) for a single power-law electron injection spectrum, the expression for bremsstrahlung emission from a nonuniformly-ionized target provides a significantly better fit to observed spectra than the expression for a uniform target; and (2) the value of E_* (and correspondingly N_*) varies with time.

An upper limit on the degree of spectral flattening $\Delta\gamma$ that can result from nonuniform ionization was derived by Su et al. (2009). They applied this upper limit to spectra from a sample of 20 flares observed by *RHESSI* in the period 2002 through 2004. They found that

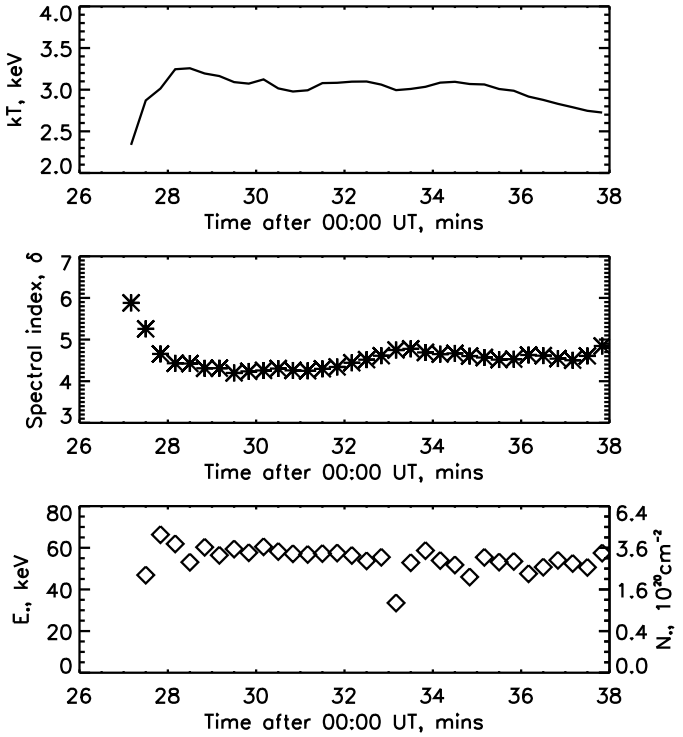

Fig. 4.2 Variation of kT, δ, E_*, and N_* throughout SOL2002-07-23T00:35 (X4.8) (Kontar et al. 2003). The variation of other parameters, such as emission measure, can be found in Holman et al. (2003) and Caspi & Lin (2010).

15 of the 20 flare spectra required a downward spectral break at low energies and for each of these 15 spectra derived the difference $\Delta\gamma$ of the best-fit power-law spectral indices above and below the break. A Monte Carlo method was used to determine the 95% confidence interval for each of the derived values of $\Delta\gamma$. Taking the value of $\Delta\gamma$ to be incompatible with nonuniform ionization if the 95% confidence interval fell above the derived upper limit, Su et al. (2009) found that six of the flare spectra could not be explained by nonuniform ionization alone. Thus, for these six flares some other cause such as a low-energy cutoff or return-current-associated energy losses (Section 5) must be at least partially responsible for the spectral flattening.

5 Return current losses

The thick-target model assumes that a beam of electrons is injected at the top of a loop and "precipitates" downwards in the solar atmosphere. Unless accompanied by an equal flux of positively charged particles, these electrons constitute a current and must create a significant

self-induced electric field that in turn drives a co-spatial return current for compensation (Hoyng et al. 1976; Knight & Sturrock 1977; Emslie 1980; D'Iakonov & Somov 1988). The return current consists of ambient electrons, plus any primary electrons that have scattered back into the upward direction. By this means we have a full electric circuit of precipitating and returning electrons that keeps the whole system neutral and the electron beam stable against being pinched off by the self-generated magnetic field required by Ampère's law for an unneutralized beam current. However, the self-induced electric field results in a potential drop along the path of the electron beam that decelerates and, therefore, removes energy from the beam electrons.

5.1 The return current electric field

The initial formation of the beam/return-current system has been studied by van den Oord (1990) and references therein. We assume here that the system has time to reach a quasi-steady state. Van den Oord finds this time scale to be on the order of the thermal electron-ion collision time. This time scale is typically less than or much less than one second, depending on the temperature and density of the ambient plasma. In numerical simulations by Siversky & Zharkova (2009), times to reach a steady state after injection ranged from 0.07 s to 0.2 s, depending on the initial beam parameters.

The self-induced electric field strength at a given location z along the beam and the flare loop, $\mathscr{E}(z)$, is determined by the current density associated with the electron beam, $j(z)$, and the local conductivity of the loop plasma, $\sigma(z)$, through Ohm's law: $\mathscr{E}(z) = j(z)/\sigma(z)$. Relating the current density to the density distribution function of the precipitating electrons, $f(z,E,\theta)$, where E is the electron energy and θ is the electron pitch angle, gives

$$\mathscr{E}(z) = \frac{2\sqrt{2}\pi}{\sigma(z)} \frac{e}{\sqrt{m_e}} \int_0^1 \int_0^\infty f(z,E,\theta)\sqrt{E}\mu dE d\mu. \tag{5.1}$$

Here μ is the cosine of the pitch angle and e and m_e are the electron charge and mass, respectively. The self-induced electric field strength $\mathscr{E}(z)$ depends on the local distribution of the beam electrons, which in turn depends on the electric field already experienced by the beam as well as any Coulomb energy losses and pitch-angle scattering that may have significantly altered the beam. It also depends on the local plasma temperature (and, to a lesser extent, density) through $\sigma(z)$, which can, in turn, be altered by the interaction of the beam with the loop plasma (i.e., local heating and "chromospheric evaporation"). Therefore, determination of the self-induced electric field and its impact on the precipitating electrons generally requires self-consistent modeling of the coupled beam/plasma system.

Such models have been computed by Zharkova & Gordovskyy (2005, 2006). They numerically integrate the time-dependent Fokker-Planck equation to obtain the self-induced electric field strength and electron distribution function along a model flare loop. The injected electron beam was assumed to have a single power-law energy distribution in the energy range from E_{low} = 8 keV to E_{upp} = 384 keV and a normal (Gaussian) distribution in pitch-angle cosine μ with half-width dispersion $\Delta\mu = 0.2$ about $\mu = 1$.

The model computations show that the strength of the self-induced electric field is nearly constant at upper coronal levels and rapidly decreases with depth (column density) in the lower corona and transition region. The rapidity of the decrease depends on the beam flux spectral index. It is steeper for softer beams (δ=5-7) than for harder ones (δ=3). The strength of the electric field is higher for a higher injected beam energy flux density (erg cm^{-2} s^{-1}),

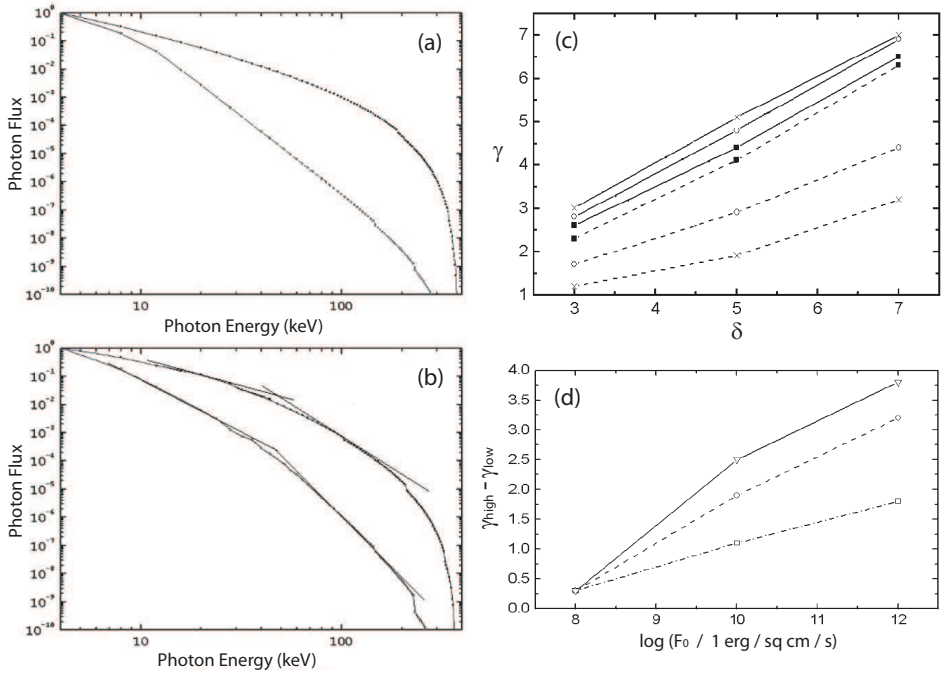

Fig. 5.1 (a) Photon spectra computed from full kinetic solutions including return current losses and collisional losses and scattering. The top spectrum is for an injected single-power-law electron flux distribution between 8 keV and 384 keV with an index of $\delta = 3$, and the bottom spectrum is for $\delta = 7$. The injected electron energy flux density is 10^8 erg cm^{-2} s^{-1}. (b) Same as (a), but for an injected energy flux density of 10^{12} erg cm^{-2} s^{-1}. The tangent lines at 20 and 100 keV demonstrate the determination of the low-energy and high-energy power-law spectral indices γ_{low} and γ_{high}. (c) The photon spectral indices γ_{low} (dashed lines) and γ_{high} (solid lines) vs. δ for an injected energy flux density of 10^8 (squares), 10^{10} (circles), and 10^{12} erg cm^{-2} s^{-1} (crosses). (d) $\gamma_{high} - \gamma_{low}$ vs. the log of the injected electron energy flux density for δ equal to 3 (bottom curve, squares), 5 (middle curve, circles), and 7 (top curve, triangles) (from Zharkova & Gordovskyy 2006).

and the distance from the injection point over which the electric field strength is highest (and nearly constant) decreases with increasing beam flux density.

5.2 Impact on hard X-ray spectra

Deceleration of the precipitating beam by the electric field most significantly affects the lower energy electrons (<100 keV), since the fraction of the original particle energy lost to the electric field is greater for lower energy electrons. This leads to flattening of the electron distribution function towards the lower energies and, therefore, flattening of the photon spectrum.

Photon spectra computed from kinetic solutions that include return current energy losses and collisional energy losses and scattering are shown in Figure 5.1 (a) and (b). Low- and high-energy spectral indices and their dependence on the power-law index of the injected electron distribution and on the injected beam energy flux density are shown in Figure 5.1 (c) and (d). The difference between the high-energy and low-energy spectral indices is seen

to increase with both the beam energy flux density and the injected electron power-law index δ. The low-energy index is found to be less than 2 for δ as high as 5 when the energy flux density is as high as 10^{12} erg cm^{-2} s^{-1}.

5.3 Observational evidence for the presence of the return current

We have seen that return current energy losses can introduce curvature into a spectrum, possibly explaining the "break" often seen in observed flare X-ray spectra. A difficulty in directly testing this explanation is that the thick-target model provides the power (energy flux) in the electron beam (erg s^{-1}), but not the energy flux density (erg cm^{-2} s^{-1}). X-ray images provide information about the area of the target, but this is typically an upper limit on the area. Even if the source area does appear to be well determined, the electron beam can be filamented so that it does not fill the entire area (the filling factor is less than 1). Also, if only an upper limit on the low-energy cutoff to the electron distribution is known, as described in Section 3.5, the energy flux density may be higher. Therefore, the observations typically only give a lower limit on the beam energy flux density.

The non-thermal hard X-ray flux is proportional to the electron beam flux density, but the return-current energy losses are also proportional to the beam flux density. As a consequence, Emslie (1980) concluded that the flux density of the non-thermal X-ray emission from a flare cannot exceed on the order of 10^{-15} cm^{-2} s^{-1} above 20 keV. Alexander & Daou (2007) have deduced the photon flux density from non-thermal electrons in a sample of 10 flares ranging from *GOES* class M1.8 to X17. They find that the non-thermal photon flux density does not monotonically increase with the thermal energy flux, but levels off (saturates) as the thermal energy flux becomes high. They argue that this saturation most likely results from the growing importance of return current energy losses as the electron beam flux increases to high values in the larger flares. They find that the highest non-thermal photon flux densities agree with an upper limit computed by Emslie.

A correlation between the X-ray flux and spectral break energy was found by Sui et al. (2007) in their study of X-ray spectra in early impulsive flares (see Section 3.5). They point out that the increasing impact of return current energy losses on higher energy electrons as the electron beam energy flux density increases could be an explanation for this correlation.

Battaglia & Benz (2008) studied two flares with non-thermal coronal hard X-ray sources for which the difference between the measured photon spectral index at the footpoints and the spectral index of the coronal source was greater than two, the value expected for coronal thin-target emission and footpoint thick-target emission from a single power-law electron distribution (see Section 10.2). They argue that return-current losses between the coronal and footpoint source regions are most likely responsible for the large difference between the spectral indices.

The return current can also affect the spectral line emission from flares. Evidence for the presence of the return current at the chromospheric level from observations of the linear polarization of the hydrogen Hα and Hβ lines has been presented by Hénoux & Karlický (2003). Dzifčáková & Karlický (2008) have shown that the presence of a return current in the corona may have a distinguishable impact on the relative intensities of spectral lines emitted from the corona.

6 Beam-plasma and current instabilities

Interaction of the accelerated electrons with plasma turbulence as they stream toward the thick-target emission region can modify the electron distribution. In this section we briefly discuss a likely source of such turbulence: that generated by the electron beam itself. If the beam is or becomes unstable to driving the growth of plasma waves, these waves can interact with the beam and modify its energy and/or pitch angle distribution until the instability is removed or the wave growth is stabilized. The return current associated with the beam (Section 5) can also become unstable, resulting in greater energy loss from the beam. Beam-plasma and return-current instabilities in solar flares have been reviewed by Melrose (1990) and Benz (2002).

A sharp, low-energy cutoff to an electron beam or, more generally, a positive slope in the beam electron energy distribution is well-known to generate the growth of electrostatic plasma waves (Langmuir waves). The characteristic time scale for the growth of these waves is on the order of $[(N_b/n)\omega_{pe}]^{-1}$, where ω_{pe} is the electron plasma frequency and N_b/n the ratio of the density of unstable electrons in the beam to the plasma density. This is on the order of microseconds for a typical coronal loop plasma density and $N_b/n \approx 10^{-3}$. This plasma instability is often referred to as the bump-on-tail instability. The result is that on a somewhat longer but comparable time scale electrons from the unstable region of the electron distribution lose energy to the waves until the sharp cutoff is flattened so that the distribution no longer drives the rapid growth of the waves. Therefore, the electron energy distribution below the low-energy cutoff is likely to rapidly become flat or nearly flat (sufficiently flat to stabilize the instability) after the electrons escape the acceleration region (see Chapters 9 & 10 of Krall & Trivelpiece 1973).

A recent simulation of the bump-on-tail instability for solar flare conditions, including Coulomb collisions and wave damping as the electrons propagate into an increasingly dense plasma, has been carried out by Hannah et al. (2009). The authors compute the mean electron flux distribution in their model flare atmosphere after injecting a power-law distribution with a sharp low-energy cutoff. They find a mean electron flux distribution with no dip (see Section 3.3) and a slightly negative slope below the original cutoff energy with a spectral index δ between 0 and 1.

A beam for which the mean electron velocity parallel to the magnetic field substantially exceeds the mean perpendicular velocity can drive the growth of waves that resonantly interact with the beam. When the electron gyrofrequency exceeds the plasma frequency, these waves are electrostatic and primarily scatter the electrons in pitch angle. Generally known as the anomalous Doppler resonance instability, this instability tends to isotropize the beam electrons. Holman et al. (1982) showed that under solar flare conditions this instability can grow and rapidly isotropize the beam electrons in less than a millisecond. They found that electrons at both the low- and high-energy ends of the distribution may remain unscattered, however, because of wave damping. This could result in up to two breaks in the emitted X-ray spectrum. On the other hand, Vlahos & Rowland (1984) have argued that non-thermal tails will form in the ambient plasma and stabilize the anomalous Doppler resonance instability by suppressing the growth of the plasma waves.

Electrons streaming into a converging magnetic field can develop a loss-cone distribution, with a deficit of electrons at small pitch angles. Both classical Coulomb collisions and loss-cone instabilities can relax this distribution by scattering electrons into the loss cone or extracting energy from the component of the electron velocities perpendicular to the magnetic field (e.g., Aschwanden 1990). One loss-cone instability, the electron-cyclotron

or gyrosynchrotron maser, produces coherent radiation observable at radio frequencies (Holman et al. 1980; Melrose & Dulk 1982).

The return current associated with the streaming electrons becomes unstable to the ion-acoustic instability when its drift speed exceeds a value on the order of the ion sound speed. The excited ion sound waves enhance the plasma resistivity, increasing the electric field strength associated with the return current, the heating of the plasma by the current, and the energy loss from the electron beam.

It has been argued that rapid plasma heating and particle acceleration in the corona should result in the expansion of hot plasma down the legs of flare loops at the ion sound speed, confined behind a collisionless ion-acoustic conduction front (Brown et al. 1979). Electrons with speeds greater than about three times the electron thermal speed would be able to stream ahead of the conduction front. This scenario has not been observationally verified, but the observational signature may be confused by the chromospheric evaporation produced by the high-energy particles streaming ahead of the conduction front.

Rowland & Vlahos (1985) argued that if the electron beam is unstable to beam plasma interactions, the return current will be carried by high-velocity electrons. This reduces the impact of collisions on the beam/return-current system and helps stabilize the system. In a recent simulation, Karlický et al. (2008) have found that for current drift velocities exceeding the electron thermal speed, the return current is carried by both the primary (drifting thermal) current and an extended tail of high-velocity electrons.

The evolution of the electron-beam/return-current system when the return-current drift speed exceeds the electron thermal speed has also been simulated by Lee et al. (2008). They find that double layers form in the return current, regions of enhanced electric field that further increase the energy losses of the electron beam. This, in turn, increases the highest electron energy to which these losses significantly flatten the electron distribution and corresponding hard X-ray spectrum.

The beam/return-current system has been simulated by Karlický (2009), with a focus on the role of the Weibel instability. The Weibel instability tends to isotropize the electron distribution. Karlický & Kašparová (2009) have computed the thin-target X-ray emission from the evolved electron distributions for a model with a weak magnetic field and another model with a strong magnetic field (ratio of the electron gyrofrequency to the plasma frequency $\sim$0 and $\sim$ 1, respectively). They demonstrate that in both cases the electron distribution is more isotropic and the directivity of the X-ray emission is lower than when the instability of the system is not taken into account, with the greatest isotropization occurring in the weak field limit.

Although we expect plasma instabilities to affect the evolution of the electron beam, observationally identifying them is difficult. The bump-on-tail instability and return current losses both lead to a flat low-energy cutoff. So far we have not established the ability to observationally distinguish a flat low-energy cutoff from a sharp low-energy cutoff. The bump-on-tail instability may be distinguishable from return-current losses by its short time scale and, therefore, the short distance from the acceleration region over which it effectively removes the unstable positive slope from the electron energy distribution. The instabilities that isotropize the electron pitch-angle distribution may be responsible for evidence from albedo measurements that flare electron distributions are isotropic or nearly isotropic (Kontar & Brown 2006b).

7 Height dependence and size of X-ray sources with energy and time

7.1 Footpoint Sources

Hard X-ray footpoint sources result from collisional bremsstrahlung radiated by precipitating electrons, which produce most of the emission in the chromosphere according to the collisional thick-target model. Depending on the density structure in the legs of the coronal magnetic loop, mildly energetic electrons lose their energy in the lower corona or transition region, while the more energetic electrons penetrate deeper into the chromosphere (see Equation 2.2).

The altitude of these hard X-ray footpoint sources could never be measured accurately before *RHESSI*, because of a lack of spatial and spectral resolution. With *RHESSI*, we can measure the centroid of the footpoint location with an accuracy of order an arcsecond for every photon energy in steps as small as 1 keV. For a flare near the limb (Figure 7.1), the centroid location translates directly into an altitude.

Aschwanden et al. (2002) studied such a flare, SOL2002-02-20T11:07 (C7.5). The heights of the footpoint sources were fitted with a power-law function of the photon energy. This yielded altitudes $h \approx 1000 - 5000$ km in the energy range $\varepsilon = 10 - 60$ keV, progressively lower with higher energy, as expected from the thick-target model (Figure 7.1, right frame).

Since the stopping depth of the precipitating electrons is a function of column density, the integrated density along their path in the chromosphere (equation 2.4), the measured height dependence of the hard X-ray centroids can be inverted to yield a density model of the chromosphere (Brown et al. 2002). Assuming the decrease in density with height had a power-law dependence and the plasma is fully ionized, the inversion of the *RHESSI* data in the example shown in Figure 7.1 yielded a chromospheric density model that has a significantly higher electron density in the $h = 2000 - 5000$ km range than the standard chromospheric models based on UV spectroscopy and hydrostatic equilibrium (VAL and FAL models). The *RHESSI*-based chromospheric density model was therefore found to be more consistent with the "spicular extended chromosphere," similar to the results from sub-mm radio observations during solar eclipses carried out at Caltech (Ewell et al. 1993).

Forward fitting *RHESSI* X-ray visibilities to an assumed circular Gaussian source shape, Kontar et al. (2008b) found for a limb flare the full width at half maximum (FWHM) size and centroid positions of hard X-ray sources as a function of photon energy with a claimed resolution of $\sim 0''.2$. They show that the height variation of the chromospheric density and of the magnetic flux density can be found with a vertical resolution of $\sim$150 km by mapping the $18 - 250$ keV X-ray emission of energetic electrons propagating in the loop at chromospheric heights of $400 - 1500$ km. Assuming collisional losses in neutral hydrogen with an exponential decrease in density with height, their observations of SOL2004-01-06T06:29 (M5.8) suggest that the density of the neutral gas is in good agreement with hydrostatic models with a scale height of around 140 ± 30 km. FWHM sizes of the X-ray sources decrease with energy, suggesting the expansion (fanning out) of magnetic flux tubes in the chromosphere with height. The magnetic scale height $B(z)(dB/dz)^{-1}$ is found to be on the order of 300 km and a strong horizontal magnetic field is associated with noticeable flux tube expansion at a height of $\sim$900 km. A subsequent analysis with an assumed elliptical Gaussian source shape (Kontar et al. 2010) confirms these results and shows that the vertical extent of the X-ray source decrease with increasing X-ray energy. The authors find the vertical source sizes to be larger than expected from the thick-target model and suggest that a multi-threaded density structure in the chromosphere is required. The thick-target model

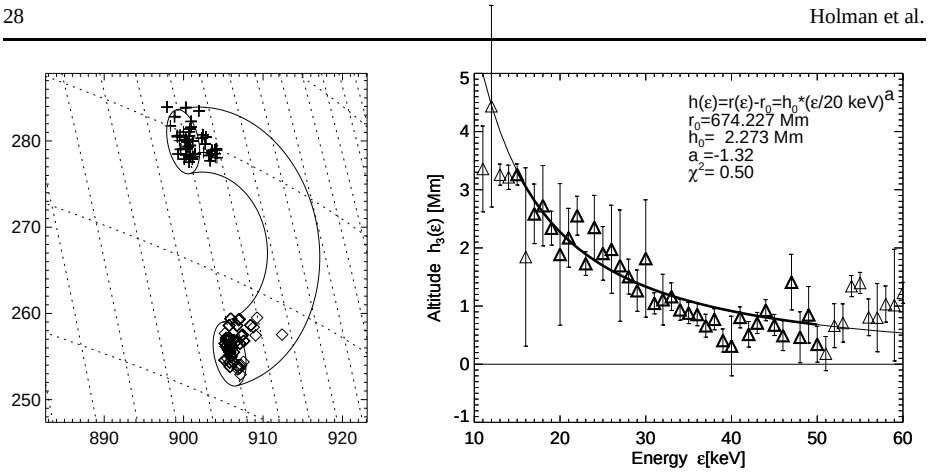

Fig. 7.1 The centroids of footpoint hard X-ray emission are marked for different photon energies between 10 keV and 60 keV for SOL2002-02-20T11:07 (C7.5), which occurred near the solar west limb and was imaged with *RHESSI* (left panel). The altitude $h(\varepsilon)$ as a function of energy ε shows a systematic height decrease with increasing energy (right panel) (from Aschwanden et al. 2002).

to which the results were compared, however, did not account for partial occultation of the X-ray sources by the solar limb.

The flare SOL2002-02-20T11:07 (C7.5) has been reanalyzed by Prato et al. (2009) using both photon maps over a range of photon energies and mean electron flux maps deduced from *RHESSI* visibilities over a range of electron energies. Using source centroids computed from the maps and assuming an exponential decrease in density with height, they found the density scale height to be an order of magnitude larger than the expected chromospheric scale height on the quiet Sun, but consistent with the scale height in a non-static, flaring atmosphere. This is also consistent with the enhanced plasma densities found at ∼1000-5000 km altitudes by Aschwanden et al. (2002).

If the results for the 400-1500 km height range (Kontar et al. 2008b) and for the ∼1000-5000 km height range (Aschwanden et al. 2002; Prato et al. 2009) are typical of flare loops, they imply that the upper chromosphere and transition region respond with a non-hydrostatic, expanded atmosphere while the low chromosphere does not respond to the flare energy release. These results could, of course, depend on the magnitude of the flare. More studies of this kind are clearly desirable, especially in coordination with observations of spectral lines from the chromosphere and transition region.

7.2 Loop Sources and their Evolution

As discussed above, footpoint sources are produced by bremsstrahlung emission in the thick-target chromosphere. The compactness of such sources results from the rapid increase of the density from the tenuous corona to the much denser chromosphere. This also gives rise to the compact height distribution of emission centroids at different energies as shown in Figure 7.1. However, if the density distribution has a somewhat gradual variation, one would expect a more diffuse height distribution. Specifically, at some intermediate energies, we expect that HXR emission would appear in the legs of the loop, rather than the commonly observed looptop sources at low energies and footpoint sources at high energies. This has

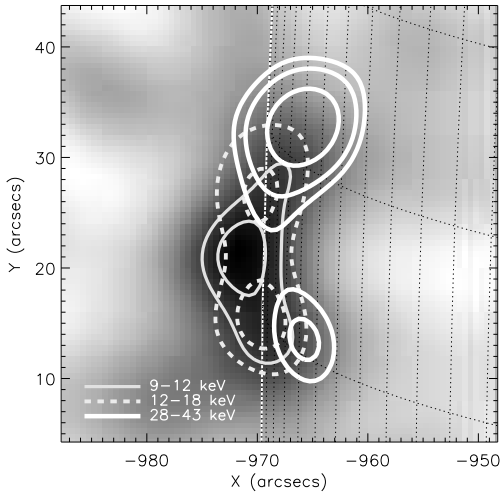

Fig. 7.2 CLEAN images at 04:58:22-04:58:26 UT during the impulsive phase of SOL2003-11-13T05:01 (M1.6). The background shows the image at 9-12 keV. The contour levels are 75% and 90% of the peak flux at 9-12 keV (*looptop*), 70% and 90% at 12–18 keV (*legs*), and 50%, 60%, & 80% at 28–43 keV (*footpoints*) (from Liu et al. 2006).

been observed by *RHESSI* in SOL2003-11-13T05:01 (M1.6) (Liu et al. 2006) (Figure 7.2) and in SOL2002-11-28T04:37 (C1.0) (Sui et al. 2006b).

To reveal more details of the energy-dependent structure of SOL2003-11-13T05:01 (M1.6), Figures 7.3*a-c* show the X-ray emission profile along the flare loop at different energies for three time intervals in sequence. The high energy emission is dominated by the footpoints, but there is a decrease of the separation of the footpoints with decreasing energy and with time. At later times the profile becomes a single source, peaking at the looptop. The general trend suggests an increase of the plasma density in the loop with time (Liu et al. 2006), which can be produced by chromospheric evaporation and can give rise to progressively shorter stopping distances for electrons at a given energy. Such a density increase also smooths out to some extent the sharp density jump at the transition region. This results in the non-thermal bremsstrahlung HXRs at intermediate energies appearing in the legs of the loop, at higher altitudes than the footpoints, as shown in Figure 7.2.

From the emission profiles in the non-thermal regimes of the photon spectra, Liu et al. (2006) derived the density distribution along the loop, using the empirical formula for non-thermal bremsstrahlung emission profiles given by Leach & Petrosian (1983, Equation 11). Leach and Petrosian found that this formula closely approximates their numerical results for a steady-state, power-law injected electron distribution with a uniform pitch-angle distribution, no return-current losses, and a loop with no magnetic field convergence. Since this formula is a function of the column density, one does not need to assume any model form of the density distribution (cf. Aschwanden et al. 2002). Figure 7.4 shows the density profiles derived from the emission profiles in the three time intervals shown in Figure 7.3. Between

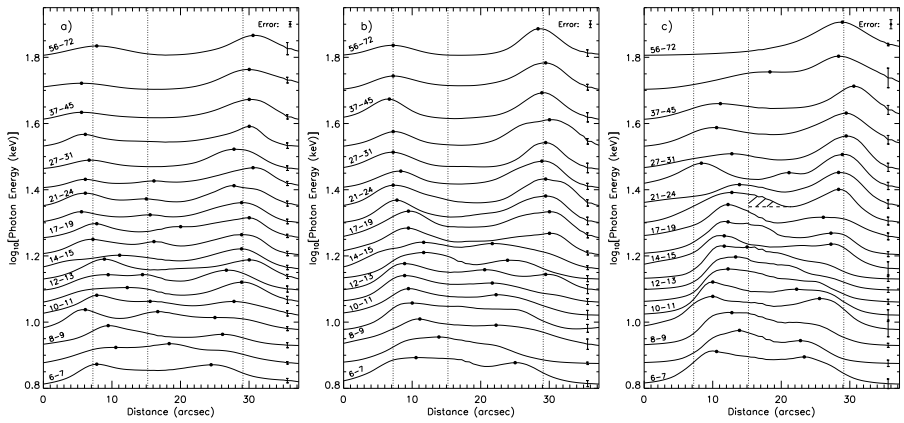

Fig. 7.3 (*a*) Brightness profiles in different energy bands measured along a semi-circular path fit to the flaring loop for the time interval 04:58:00–04:58:24 UT of SOL2003-11-13T05:01. The vertical axis indicates the average photon energy (logarithmic scale) of the energy band for the profile. Representative energy bands (in units of keV) are labeled above the corresponding profiles. The filled circles mark the local maxima, and the vertical dotted lines are the average positions of the centroids of the looptop and footpoint sources. (*b*, *c*) Same as (*a*), but for 04:58:24–04:58:48 and 04:58:48–04:59:12 UT, respectively. The error bars show the uncertainty of the corresponding profile (from Liu et al. 2006).

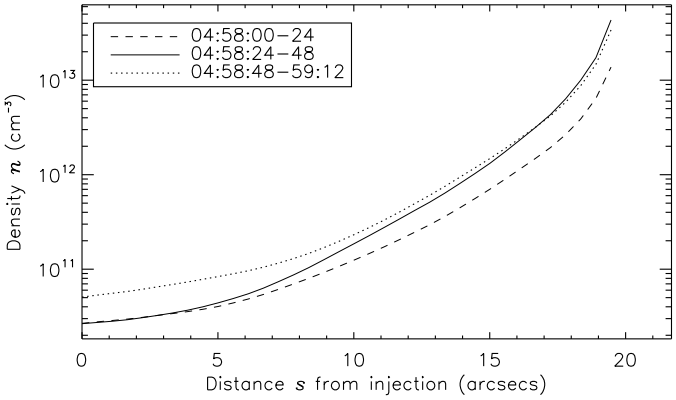

Fig. 7.4 Averaged density profiles along one leg of the loop inferred from the HXR brightness profiles during the three time intervals in Figure 7.3. The distance is measured along the leg extending from the centroid of the thermal looptop source at about 15 arcsec in Figure 7.3 to the end of the fitted semi-circle at about 37 arcsec (from Liu et al. 2006).

the first and second intervals, the density increases dramatically in the lower part of the loop, while the density near the looptop remains essentially unchanged. The density enhancement then shifts to the looptop from the second to the third interval. This indicates a mass flow from the chromosphere to the looptop, most likely caused by chromospheric evaporation. For papers studying chromospheric evaporation using coordinated *RHESSI* HXR and EUV Doppler-shift observations, see Milligan et al. (2006a,b) and Brosius & Holman (2007).

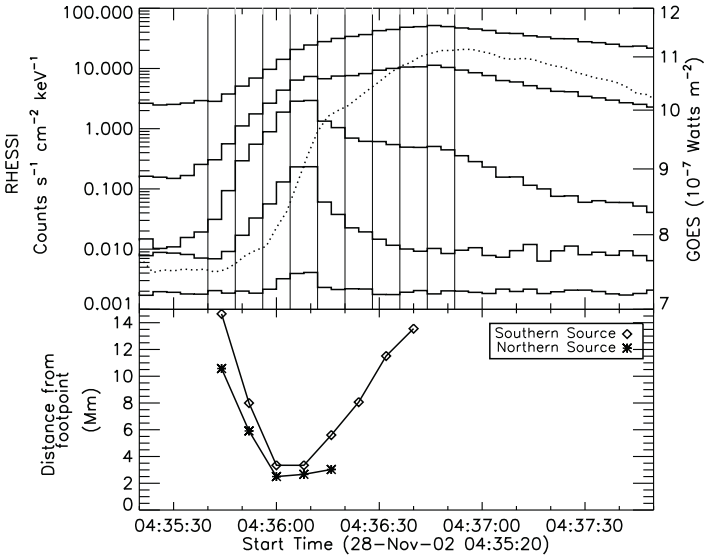

Fig. 7.5 *RHESSI* (*solid lines*) and *GOES* 1-8 Å (*dotted line*) light curves are shown in the *top panel*. The *RHESSI* energy bands (from top to bottom) are 3–6, 6–12, 12–25, and 50–100 keV, with scaling factors of 5, 1, 4, 3, and 0.5, respectively. The *RHESSI* and *GOES* integration times are 4 and 3 s, respectively. The *bottom panel* shows the distance between the 3-6 keV moving source centroids and their corresponding footpoint centroids located in the 25-50 keV image of the flare at the time of peak emission. The distances are plane-of-sky values with no correction for motions away from or toward the observer (from Sui et al. 2006b).

The flare SOL2002-11-28T04:37 (C1.0) was an early impulsive flare, meaning that there was minimal pre-heating of plasma to X-ray-emitting temperatures prior to the appearance of impulsive hard X-ray emission (see Section 3.5). *RHESSI* observations of this flare showed coronal X-ray sources that first moved downward and then upward along the legs of the flare loop (Sui et al. 2006b). The bottom panel of Figure 7.5 shows the motion of the sources observed in the 3-6 keV band. *RHESSI* and *GOES* light curves are shown in the top panel. The sources originated at the top of the flare loop and then moved downward along both legs of the loop until the time of peak emission at energies above 12 keV. Afterward the source in the northern leg of the loop was no longer observable, but the source in the southern leg moved back to the top of the loop. Its centroid location at the looptop was slightly but significantly lower than the centroid position at the beginning of the flare. Higher-energy sources showed a similar evolution, but they had lower centroid positions than their lower energy counterparts, again in agreement with the predictions of the thick-target model.

The early downward source motion along the legs of the loop is a previously unobserved phenomenon. At this time we do not know if the occurrence is rare, or if it is simply rarely observed because of masking by the radiation from the thermal plasma. Sui et al. (2006b) argue that the motion results from the hardening of the X-ray spectrum, and possibly an increase in the low-energy cutoff, as the flare hard X-ray emission rises to its peak intensity. A flatter spectrum results in a higher mean energy of the electrons contributing to the radiation at a given X-ray energy. In a loop with a plasma density that increases significantly from the top to the footpoints, these higher energy electrons will propagate to a lower altitude in the

loop as the spectrum hardens. The softening of the spectrum after peak emission would also contribute to the upward motion of the source after the peak. However, at that time chromospheric evaporation would likely be increasing the density in the loop, as discussed above for SOL2003-11-13T05:01 (M1.6) , and thermal emission would be more important. All of these can contribute to an increase in the height of the centroid of the X-ray source. The downward motion may only occur in initially cool flare loops, i.e., early impulsive flares, because these loops are most likely to contain the density gradients that are required.

In an attempt to differentiate between thermal and non-thermal X-ray emission, Xu et al. (2008) modeled the size dependence with photon energy of coronal X-ray sources observed by *RHESSI* in ten M-class limb flares. They determined the one-sigma Gaussian width of the sources along the length of the flare loops by obtaining forward fits to the source visibilities. The integration times ranged from one to ten minutes and the source sizes were determined in up to eight energy bins ranging in energy from as low as 7 keV to as high as 30 keV. They found the source sizes to increase slowly with photon energy, on average as $\varepsilon^{1/2}$. The results were compared with several models for the variation of the source size with energy. The source size was expected to vary as $\varepsilon^{-1/2}$ for a thermal model with a constant loop density and a temperature that decreased with a Gaussian profile along the legs of the loop from a maximum temperature at the top of the loop. For the injection of a power-law electron flux distribution into a high-density loop so that the loop is a collisional thick target, the source size was expected to increase as ε^2. Neither of these models are consistent with the observed $\varepsilon^{1/2}$ dependence. A hybrid thermal/non-thermal model and a non-thermal model with an extended acceleration region at the top of the loop were found to be consistent with the deduced scaling, however. The extended acceleration region was deduced to have a half-length in the range $10'' - 18''$ and density in the range $(1-5) \times 10^{11}$ cm^{-3}. We note that the extended acceleration region model implies a column density in the range $0.73 - 6.5 \times 10^{20}$ cm^{-2} along the half length and, from Equation 2.4, all electrons with energies less than somewhere in the range of 23 keV – 68 keV that traverse this half length will lose all of their energy to collisions. The acceleration process would therefore need to be efficient enough to overcome these losses. On the other hand, the 7 – 30 keV energy range is the range in which fits to spatially integrated X-ray spectra typically show a combination of both thermal and non-thermal bremsstrahlung emission.

Studies of flare hard X-ray source positions and sizes as a function of photon energy and time hold great promise for determining the height structure of flare plasma and its evolution, as well as providing information about the magnetic structure of the flare loop. Such studies are currently in their early stages, in that they usually assume an over simplified power-law or exponential height distribution for the plasma and do not take into account the variation of the plasma ionization state with height. They also assume the simple, one-dimensional collisional thick-target model, without consideration of the pitch-angle distribution of the beam electrons or the possibility of additional energy losses to the beam (such as return-current losses). Given the potential for obtaining a better understanding of flare evolution, we look forward to the application of more sophisticated models to the flare hard X-ray data.

8 Hard X-ray timing

The analysis of energy-dependent time delays allows us to test theoretical models of physical time scales and their scaling laws with energy. In the wavelength domain of hard X-rays, there are at least three physical processes known in the observation of solar flares that lead to measurable time delays as a function of energy (for a review, see Aschwanden 2004): (1)

time-of-flight dispersion of free-streaming electrons, (2) magnetic trapping with the collisional precipitation of electrons, and (3) cooling of the thermal plasma.

8.1 Time-of-Flight Delays

The first type, the *time-of-flight (TOF)* delay, has a scaling of $\Delta t(\varepsilon) \propto \varepsilon^{-1/2}$ and is caused by velocity differences of electrons that propagate from the coronal acceleration site to the chromospheric energy-loss region. The time differences are of order $\Delta t \approx 10 - 100$ ms for non-thermal electrons at energies $E \approx 20 - 100$ keV (e.g., Aschwanden et al. 1995, 1996). The measurement of such tiny time delays requires high photon statistics and high time resolution. Such data were provided by *CGRO*/BATSE, which had 8 detectors, each with an effective collecting area of $\sim$2000 cm^2 and oriented at different angles to the Sun so that detector saturation at high count rates was not a problem. (For comparison, the total effective collecting area of *RHESSI*'s detectors is less than 100 cm^2.)

These studies of TOF delays have provided important evidence that electrons are accelerated in the corona, above the top of the hot flare loops observed in soft X-rays. The fine structure in the light curves of most, but not all, of the studied flare bursts showed energy-dependent time delays consistent with the free streaming of electrons to the footpoints of the flare loops from an origin somewhat more distant than the half-length of the loops (Aschwanden et al. 1995; Aschwanden & Schwartz 1995; Aschwanden et al. 1996).

8.2 Trapping Delays

The second type, the *trapping delay*, is caused by magnetic mirroring of coronal electrons which precipitate toward the chromosphere after a collisional time scale $\Delta t(\varepsilon) \propto \varepsilon^{3/2}$. This is observable for time differences of $\Delta t \approx 1 - 10$ s for non-thermal electrons at $E \approx 20 - 100$ keV (e.g., Vilmer et al. 1982; Aschwanden et al. 1997). For trapping delays the higher energy X-rays lag the lower energy X-rays, as opposed to time-of-flight delays where the higher energy X-rays precede the lower energy X-rays.

Aschwanden et al. (1997) filtered variations on time scales $\sim$1 s or less out of *CGRO* BATSE flare HXR light curves. They found time delays in the remaining gradually varying component to be consistent with magnetic trapping and collisional precipitation of the particles. Trap plasma densities $\sim 10^{11}$ cm^{-3} were deduced. No evidence was found for a discontinuity in the delay time as a function of energy and, therefore, for second-step (two-stage) acceleration of electrons at energies ≤ 200 keV.

8.3 Thermal Delays

The third type, the *thermal delay*, can be caused by the temperature dependence of cooling processes, such as by thermal conduction, $\tau_c(T) \propto T^{-5/2}$ (e.g., Antiochos & Sturrock 1978; Culhane et al. 1994), or by radiative cooling, $\tau_r(T) \propto T^{5/3}$ (e.g., Fisher & Hawley 1990; Cargill et al. 1995). The observed physical parameters suggest that thermal conduction dominates in flare loops at high temperatures as observed in soft X-ray wavelengths, while radiative cooling dominates in the later phase in postflare loops as observed in EUV wavelengths (Antiochos & Sturrock 1978; Culhane et al. 1994; Aschwanden & Alexander

2001). When the temperature drops in the decay phase of flares, the heating rate can justifiably be neglected and the conductive or radiative cooling rate dominate the temperature evolution. Before *RHESSI*, the cooling curve $T(t)$ in flare plasmas had been studied in only a few flares (e.g., McTiernan et al. 1993; Culhane et al. 1994; Aschwanden & Alexander 2001).

The high spectral resolution of *RHESSI* data is particularly suitable for any type of thermal modeling, because we can probe the thermal plasma from $\sim$3 keV up to $\sim$30 keV with a FWHM resolution of $\sim$1 keV thanks to the cooled germanium detectors (Lin et al. 2002; Smith et al. 2002). This allows us to measure flare temperatures with more confidence. A statistical study of flare temperatures measured in the range of $T \approx 7-20$ MK indeed demonstrates some agreement between the values obtained from spectral fitting of *RHESSI* data with those obtained from *GOES* flux ratios (Battaglia et al. 2005), although *RHESSI* has a bias for the high-temperature tail of the differential emission measure (DEM) distribution (Aschwanden et al. 2008; Väänänen & Pohjolainen 2007). Of course, we expect an agreement between the deduced emission-measure-weighted temperatures only when both instruments are sensitive to a temperature range that covers the flare DEM peak.

A close relationship between the non-thermal and thermal time profiles was found early on, in the sense that the thermal emission often closely resembles the integral of the non-thermal emission, a relationship that is now known as the *Neupert effect* (Neupert 1968; Hudson 1991; Dennis & Zarro 1993). This relationship is, however, strictly only expected for the asymptotic limit of very long cooling times, while a physically more accurate model would quantify this effect by a convolution of the non-thermal heating with a finite cooling time. The deconvolution of the e-folding cooling time in such a model has never been attempted statistically and as a function of energy or temperature. Theoretical discussions of the Neupert effect, including multiple energy release events, chromospheric evaporation, and cooling, can be found in Warren & Antiochos (2004), Liu et al. (2010), and Reeves & Moats (2010).

The cooling time at a given energy can be estimated from the decay time of a flare time profile. For instance, the decay times measured with *GOES* in soft X-rays were found to have a median of $\tau_{decay} \approx 6$ min (Veronig et al. 2002a,b). The observed cooling times have typically been found to be much longer than predicted from classical conduction, but shorter than the radiative cooling time (e.g., McTiernan et al. 1993; Jiang et al. 2006; Raymond et al. 2007). This discrepancy could result from either continuous heating or suppression of conduction during the decay phase, or a combination of both.

The Neupert effect was tested by correlating the soft X-ray peak flux with the (time-integrated) hard X-ray flux. A high correlation and time coincidence between the soft X-ray peak and hard X-ray end time was generally found, but a significant fraction of events also had a different timing (Veronig et al. 2002c). A delay of 12 s was found in the soft X-ray flux time derivative with respect to the hard X-ray flux in SOL2003-11-13T05:01 (M1.6) (Liu et al. 2006, also see Section 7.2). Time delays such as this could be related to the hydrodynamic flow time during chromospheric evaporation. Tests of the "theoretical Neupert effect," i.e., comparisons of the beam power supply of hard X-ray-emitting electrons and the thermal energy of evaporated plasma observed in soft X-rays, found it to strongly depend on the low-energy cutoff to the non-thermal electron distribution (Veronig et al. 2005). This provides another approach to deducing the energy at which the low-energy cutoff in the electron distribution occurs in individual flares. The Neupert effect has also been studied in several flares by Ning (2008, 2009), who finds a high correlation between the hard X-ray flux and the time derivative of the thermal energy deduced from X-ray spectral fits (Ning

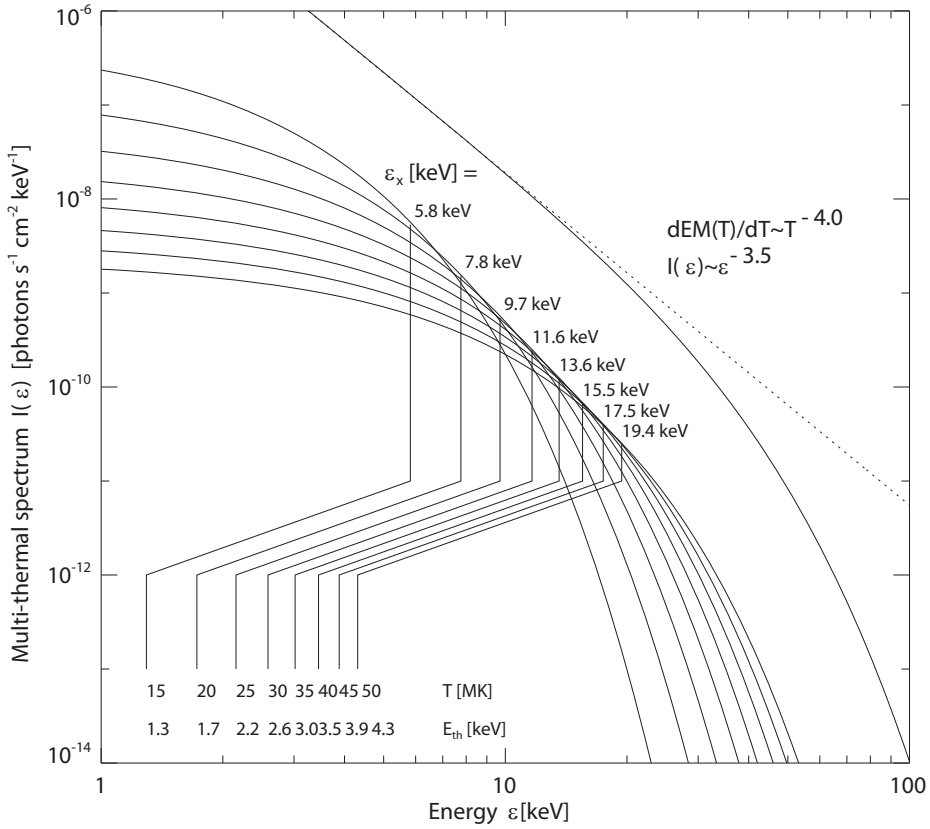

Fig. 8.1 Example of a multi-thermal spectrum with contributions from plasmas with temperatures of $T = 15, 20, ..., 50$ MK and a DEM distribution of $dEM(T)/dT \propto T^{-4}$. The individual thermal spectra and their sum are shown with thin linestyle, where the sum represents the observed spectrum. Note that the photons in the energy range $\varepsilon = 5.8 - 19.4$ keV are dominated by temperatures of T=15–50 MK, which have a corresponding thermal energy that is about a factor of $(4 + 1/2) = 4.5$ lower than the corresponding photon energy ($\varepsilon_{th} = 1.3 - 4.3$ keV). The summed photon spectrum without the high-temperature cutoff approaches the power-law function $I(\varepsilon) \propto \varepsilon^{-3.5}$ (*dotted line*) (from Aschwanden 2007).

2008) and an anti-correlation between the hard X-ray spectral index and the time rate of change of the UV flare area observed by *TRACE* (Ning 2009).

8.4 Multi-Thermal Delay Modeling with *RHESSI*

Since major solar flares generally produce a large number of individual postflare loops, giving the familiar appearance of loop arcades lined up along the flare ribbons, it is unavoidable that each loop is heated up and cools down at different times, so that a spatially integrated spectrum always contains a multi-thermal differential emission measure distribution (cf. Warren 2006). The resulting multi-thermal bremsstrahlung spectrum (for photon energies

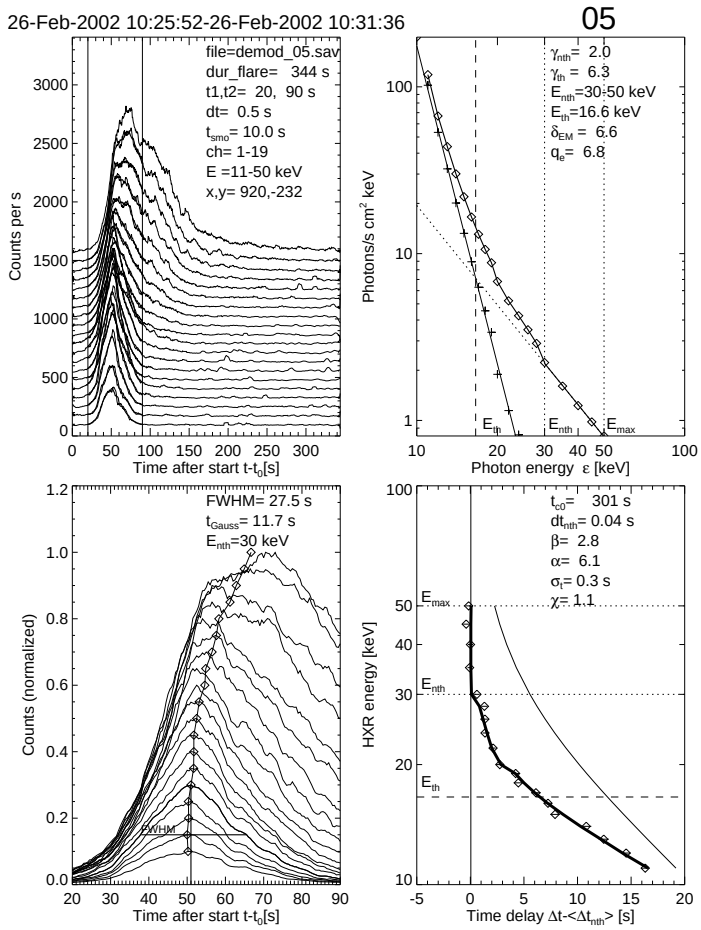

Fig. 8.2 X-ray light curves are shown for SOL2002-02-26T10:27 (C9.6), for energies of 10 keV to 30 keV in intervals of 1 keV, observed with *RHESSI* (left panels). The spectrum is decomposed into thermal and non-thermal components (top right panel) and the delay of the peaks at different energies is fitted with a thermal conduction cooling time model that has a scaling of $\tau_{cond}(T) \approx T^{-\beta}$ (right bottom panel). The best fit shows a power index of $\beta = 2.8$, which is close to the theoretically expected value of $\beta = 5/2$ (Equation 8.2). The full delay of the thermal component is indicated with a thin curve (bottom left panel), while the weighted (thermal+non-thermal) fit is indicated with a thick curve (from Aschwanden 2007).

ε) observed in soft X-rays (neglecting the Gaunt factor of order unity),

$$I(\varepsilon) = I_0 \int \frac{\exp(-\varepsilon/k_B T)}{T^{1/2}} \frac{dEM(T)}{dT} dT \ , \tag{8.1}$$

is then a function of a multi-thermal *differential emission measure* distribution $dEM(T) = n^2(T)dV$. An example of a multi-thermal spectrum from a differential emission measure proportional to T^{-4} up to a maximum temperature of 50 MK is shown in Figure 8.1.

As discussed above, the initial cooling of the hot flare plasma (say at $T \gtrsim 10$ MK) is generally dominated by conductive cooling (rather than by radiative cooling, which can dominate later after the plasma cools to EUV-emitting temperatures of $T \lesssim 2$ MK). The

thermal conduction time has the following temperature dependence:

$$\tau_{cond}(T) = \frac{\varepsilon_{th}}{dE/dt_{cond}} = \frac{3n_e k_B T}{\frac{d}{ds}\kappa T^{5/2}\frac{dT}{ds}} \approx \frac{21}{2}\frac{n_e L^2 k_B}{\kappa} T^{-5/2} = \tau_{c0}\left(\frac{T}{T_0}\right)^{-5/2} ; \qquad (8.2)$$

see Aschwanden (2007) for parameter definitions. Since the thermal bremsstrahlung at decreasing photon energies is dominated by radiation from lower temperature flare plasma, the conductive cooling time is expected to become longer at lower temperatures ($\tau_{cond} \propto T^{-5/2}$). Thus, the soft X-ray peak is always delayed with respect to the harder X-ray peaks, reflecting the conductive cooling of the flare loops.

Aschwanden (2007) has measured and modeled this conductive cooling delay $\tau_{cond}(\varepsilon)$ for a comprehensive set of short-duration ($\leq$ 10 min) flares observed by *RHESSI*. One example is shown in Figure 8.2. He finds that the cooling delay Δt expressed as a function of the photon energy ε and photon spectral index γ can be approximated by

$$\Delta t(\varepsilon,\gamma) \approx \tau_g \frac{7}{4}\left[\log\left(1+\frac{\tau_{c0}}{\tau_g}\left(\frac{\varepsilon}{(\gamma-1)\varepsilon_0}\right)^{-\beta}\right)\right]^{3/4} , \qquad (8.3)$$

(where τ_g is the Gaussian width of the time profile peak) and yields a new diagnostic of the process of conductive cooling in multi-thermal flare plasmas. In a statistical study of 65 flares (Aschwanden 2007), 44 (68%) were well fit by the multi-thermal model with a best fit value for the exponent of $\beta = 2.7 \pm 1.2$, which is consistent with the theoretically expected value of $\beta = 2.5$ according to Equation 8.2. The conductive cooling time at $T_0 = 11.6$ MK ($\varepsilon_0 = 1$ keV) was found to range from 2 to 750 s, with a mean value of $\tau_{c0} = 40$ s.

We note that these timing data, as well as thick-target fits to the non-thermal part of spectra that reveal the evolution of the energy content in accelerated electrons, provide additional constraints on models such as the multithread flare model of Warren (2006).

9 Hard X-ray spectral evolution in flares

9.1 Observations of spectral evolution

The non-thermal hard X-ray emission from solar flares, best observed in the 20 to 100 keV range, is highly variable. Often several emission spikes with durations ranging from seconds to minutes are observed. In larger events, sometimes a more slowly variable, long duration emission can be observed in the later phase of the flare. Hence, most flares start out with an *impulsive* phase, while some events, mostly large ones, show the presence of a late *gradual* phase in the hard X-ray time profile.

While these two different behaviors can already be spotted by looking at lightcurves, they also are distinct in their spectral evolution. The impulsive spikes tend to be harder at the peak time, and softer both in the rise and decay phase. The spectrum starts soft, gets harder as the flux rises and softens again after the maximum of the emission. This pattern of the spectral evolution is thus called *soft-hard-soft* (SHS). On the other hand, in the gradual phase, the flux often slowly decreases, while the spectrum stays hard or gets even harder. This different kind of spectral evolution is called *soft-hard-harder* (SHH).

Historically, both the SHS (Parks & Winckler 1969; Kane & Anderson 1970) and the SHH behavior (Frost & Dennis 1971) were observed in the early era of hard X-ray observations of the Sun. Subsequent investigation confirmed both the SHS (Benz 1977; Brown & Loran

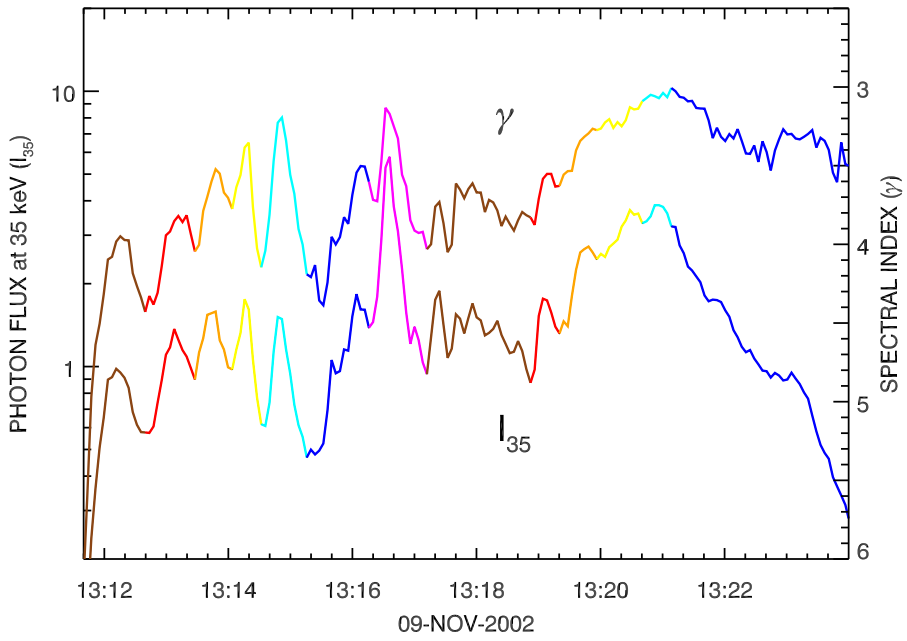

Fig. 9.1 Time evolution of the spectral index γ (*upper curve, linear scale on right*) and the flux normalization I_{35} (*lower curve, logarithmic scale on left*) of the non-thermal component in SOL2002-11-09T13:23 (M4.9). Different emission spikes are shown in different colors (after Grigis & Benz 2004).

1985; Lin & Schwartz 1987; Gan 1998; Fletcher & Hudson 2002; Hudson & Fárník 2002) and the SHH (Cliver et al. 1986; Kiplinger 1995; Saldanha et al. 2008; Grigis & Benz 2008) behavior. The SHH behavior has been found to be correlated with proton events in interplanetary space (Kiplinger 1995; Saldanha et al. 2008; Grayson et al. 2009).

Evidence for hard-soft-hard (HSH) spectral evolution at energies above ∼50 keV has been reported for multiple spikes in SOL2004-11-03T03:35 (M1.6) (Shao & Huang 2009b). SHS behavior was observed at lower energies. This HSH behavior might be explained by albedo, which typically peaks around 30–40 keV (see Kontar et al. 2011), but the authors corrected for albedo from isotropically emitted photons. A likely explanation is that the spikes overlie a harder, gradually varying component, possibly emission from trapped electrons (Section 8.2).

While all these observations established the qualitative properties of the spectral evolution, a statistical analysis of the quantitative relation between the flux and spectral index had not been performed in the pre-*RHESSI* era. Here, we summarize *RHESSI* results investigating quantitatively the spectral evolution of the nonthermal component of the hard X-ray emission, as well as the theoretical implications. More details can be found in Grigis & Benz (2004, 2005, 2006).

To quantify the spectral evolution, a simple parameterization for the shape of the nonthermal spectrum is needed. Luckily, in solar flares the spectrum is well described by a power law in energy, which often steepens above 50 keV. Such a softening of the spectrum can be modeled by a broken power-law model. However, it is difficult to observe such a

downward bending at times of weak flux, because the high-energy region of the spectrum is lost in the background. As a compromise, Grigis & Benz (2004) fitted the data to a single power-law function at all times. Although the single power law does not always provide a good fit to the spectra, it provides a characteristic spectral slope and ensures a uniform treatment of the spectra at different times.

The two free parameters of the power-law model are the spectral index γ and the power-law normalization I_{ε_0} at the reference energy ε_0. The reference energy ε_0 is arbitrary, but fixed, usually near the logarithmic mean of the covered energy range. In the *RHESSI* spectral analysis software, OSPEX, $\varepsilon_0 = 50$ keV by default. The time dependent spectrum is given by

$$I(\varepsilon,t) = I_{\varepsilon_0}(t)\left(\frac{\varepsilon}{\varepsilon_0}\right)^{-\gamma(t)}. \tag{9.1}$$

A representative sample of 24 solar flares of *GOES* magnitudes between M1 and X1 was selected by Grigis & Benz (2004). The spectral model (Equation 9.1), with the addition of an isothermal emission component at low energies, was fitted with a cadence of one *RHESSI* spin period (about 4 s). This delivered a sequence of measurements of the quantities $I_{\varepsilon_0}(t)$ and $\gamma(t)$ for each of the 24 events, covering a total time of about 62 minutes of non-thermal hard X-ray emission. For these events, $\varepsilon_0 = 35$ keV was chosen, a meaningful energy which lies about in the middle of the range where the non-thermal emission is best observed in these M-class flares.

An example of the measured time evolution of the spectral index γ and the flux normalization I_{35} for the longer-lasting event of the set is shown in Figure 9.1. A correlation in time between the two curves can be readily seen. Single emission spikes are plotted in different colors, so that the soft-hard-soft evolution can be observed during each spike (with the exception of the late, more gradual phase, where the emission stays hard as the flux decays).

As there is an anti-correlation in time between $\log I_{35}(t)$ and $\gamma(t)$, a plot of one parameter as a function of the other, eliminating the time dependence, shows the relationship between them. Figure 9.2 shows plots of γ vs. I_{35} for 3 events where there are only one or two emission peaks. The points in the longer uninterrupted rise or decay phase during each event are marked by plus symbols. A linear relationship between $\log I_{35}$ and γ can be seen during each phase, although it can be different during rise and decay.

On the other hand, a plot of all the 911 fitted model parameters for all the events show a large scatter, as shown in Figure 9.3. The large scatter can be understood as originating from the superposition of data from a large numbers of different emission spikes, each featuring linear trends with different parameters. This plot does demonstrate, however, the tendency for flatter spectra to be associated with more intense flares.

RHESSI observations of the gradual phase of large solar flares (Grigis & Benz 2008) and its relation with proton events (Saldanha et al. 2008; Grayson et al. 2009) have shown that the hardening behavior is complex and cannot be characterized by a continuously increasing hardness during the event. Therefore the soft-hard-harder (SHH) denomination does not accurately reflect the observed spectral evolution. Rather, phases of hardening (or even approximatively constant hardness) are often seen in larger events as the flux decays (Kiplinger 1995). The start of the hardening phase can happen near the main peak of the flare, or later. The end of hardening can even be followed by new impulsive SHS peaks. The most recent statistical study of the correlation of SHH behavior with proton events (Grayson et al. 2009) found that in a sample of 37 flares that were magnetically well-connected to Earth, 18

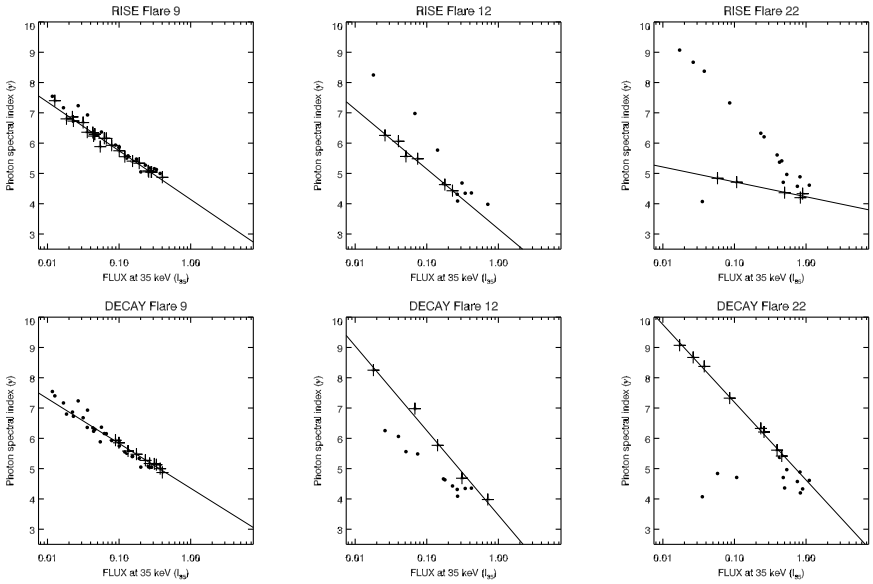

Fig. 9.2 Spectral index γ vs. flux normalization I_{35} for three events, showing the linear dependence of single rise and decay phases of emission spikes on a log-linear scale. Dots mark results from individual spikes, while pluses mark the longer rise or decay phase (from Grigis & Benz 2004).

showed SHH behavior and 12 of these produced solar energetic particle (SEP) events. None of the remaining 19 flares that did not show SHH behavior produced SEP events.

9.2 Interpretation of spectral evolution

Can we explain the soft-hard-soft spectral behavior theoretically? The problem here is that many effects contribute to the properties of the high-energy electron distribution whose bremsstrahlung hard X-rays are observed by *RHESSI* and similar instruments. We can identify three main, closely related classes of physical processes that affect the distribution of the electrons and the spectrum of the X-ray photons they generate: (1) the *acceleration* of part of the thermal ambient plasma, (2) the *escape* from the acceleration region, and (3) the *transport* to the emitting region. The photon spectrum also depends on the properties of the bremsstrahlung emission mechanism.

Miller et al. (1996) proposed a stochastic acceleration mechanism where electrons are energized by small-amplitude turbulent fast-mode waves, called the transit-time damping model. They showed that their model could successfully account for the observed number and energy of electrons accelerated above 20 keV in subsecond spikes or energy release fragments in impulsive solar flares. However, they made no attempt to explain the observed hard X-ray spectra (which are softer than predicted by the transit-time damping model) and did not consider spectral evolution. Furthermore, this approach does not account for particle escape. Grigis & Benz (2006) extended the model with the addition of a term describing the escape of the particles from the acceleration region, as in the model of Petrosian & Donaghy (1999). To ensure conservation of particles, they also add a source term of cold particles coming into the accelerator (such as can be provided by a return current).

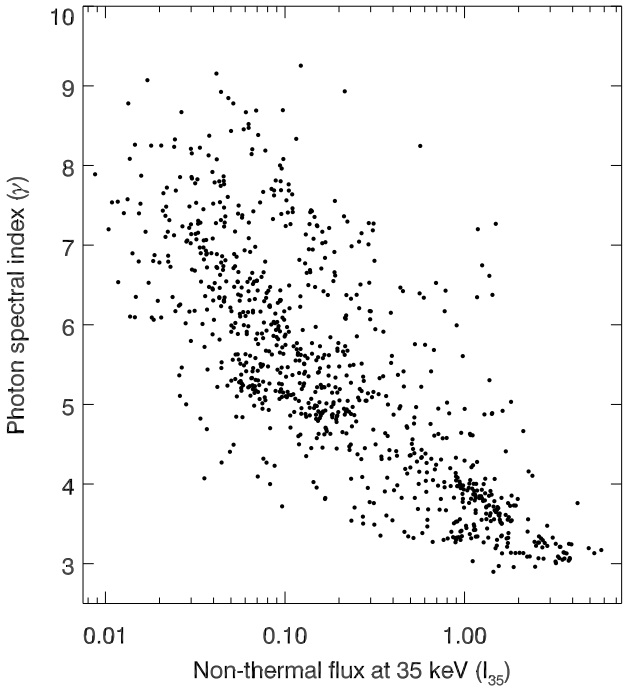

Fig. 9.3 Plot of the spectral index γ versus the fitted non-thermal flux at 35 keV (given in photons s^{-1} cm^{-2} keV^{-1}). All 911 data points from the 24 events are shown (from Grigis & Benz 2004).

The stochastic nature of this acceleration model implies that the electrons undergo a diffusion process in energy space. Mathematically, the acceleration is described by the following convective-diffusive equation:

$$\frac{\partial f}{\partial t} = \frac{1}{2}\frac{\partial^2}{\partial E^2}\Big[(D_{\rm COLL}+D_{\rm T})\,f\Big] - \frac{\partial}{\partial E}\Big[(A_{\rm COLL}+A_{\rm T})\,f\Big] - S(E)\cdot f + Q(E)\,, \qquad (9.2)$$

where $f(E)$ is the electron density distribution function, $D_{\rm T}$ and $A_{\rm T}$ are, respectively, the diffusion and convection coefficients due to the interactions of the electrons with the accelerating turbulent waves, $D_{\rm COLL}$ and $A_{\rm COLL}$ are, respectively, the diffusion and convection coefficients due to collisions with the ambient plasma, $S(E)$ is the sink (escape) term, and $Q(E)$ is the source (return current) term. The escape term is proportional to $v(E)/\tau$, where $v(E)$ is the electron speed, and τ is the escape time. The escape time can be energy-dependent, but for simplicity it is initially kept constant. The longer the escape time, the better the particles are trapped in the accelerator. The source term is in the form of a Maxwellian distribution of electrons with the same temperature as the ambient plasma.

The coefficients $D_{\rm T}$ and $A_{\rm T}$ are proportional to the dimensionless acceleration parameter

$$I_{\rm ACC} = \frac{U_{\rm T}}{U_{\rm B}}\cdot\frac{c\langle k\rangle}{\Omega_{\rm H}}, \qquad (9.3)$$

where $U_{\rm T}$ and $U_{\rm B}$ are, respectively, the energy densities of the turbulent waves and of the ambient magnetic field, $\langle k\rangle$ is the average wave vector, and $\Omega_{\rm H}$ is the proton gyrofrequency.

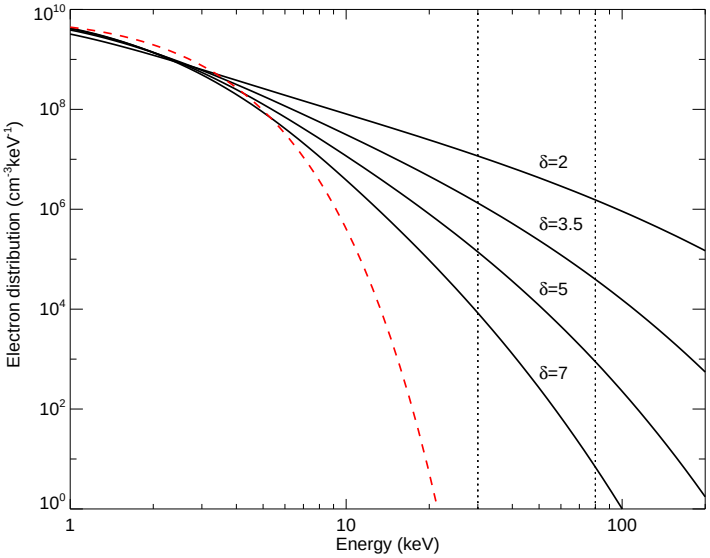

Fig. 9.4 Accelerated electron density distributions with different values of the power-law index resulting from changes in $I_\tau = I_{\rm ACC} \cdot \tau$. The dashed curve represents the ambient Maxwellian distribution. The two dotted lines indicate the energy range used for the computation of the power-law index δ shown above each spectrum. Harder spectra have a larger I_τ value (from Grigis & Benz 2006).

Equation 9.2 can be solved numerically until an equilibrium state ($\partial f/\partial t = 0$) is reached. The equilibrium electron spectra from the model are controlled by two parameters: the acceleration parameter $I_{\rm ACC}$ described above and the escape time τ. Above 10-20 keV, the collision and source terms in Equation (9.2) can be neglected, since they apply to the ambient Maxwellian, and thus the equilibrium spectra depend to a first approximation only on the product $I_\tau = I_{\rm ACC} \cdot \tau$.

Figure 9.4 shows the equilibrium electron spectra for different values of $I_\tau = I_{\rm ACC} \cdot \tau$. As I_τ increases, the spectrum gets harder and harder. To explain the soft-hard-soft effect, either the acceleration or the trapping efficiency (or both) must increase until the peak time, and then decrease again. We note that this model does not include magnetic trapping (other than in the magnetic turbulence itself), which can alter the computed electron spectra and their time evolution (e.g., Metcalf & Alexander 1999).

To see whether this produces the linear relation between the spectral index and the log of the flux normalization, Grigis & Benz (2006) computed the hard X-ray emission from these model electron spectra. Since these are equilibrium spectra, thin-target emission was computed. They then plotted the spectral index vs. the flux normalization of the resulting photon spectra. Since the spectra are not power-law, but bend down, they fit a power-law model to the model photon spectrum in a similar range as the one used for the observations.

Figure 9.5 shows the computed values for the spectral indices and flux normalizations for both the electron and the photon spectrum from the model. The results show that there is indeed a linear relation between the spectral index and the log of the flux normalization.

An alternative mechanism that could be responsible for soft-hard-soft spectral evolution is return current losses as the electrons propagate to and within the thick-target footpoints of the flare loop (Zharkova & Gordovskyy 2006). The highest electron energy to which re-

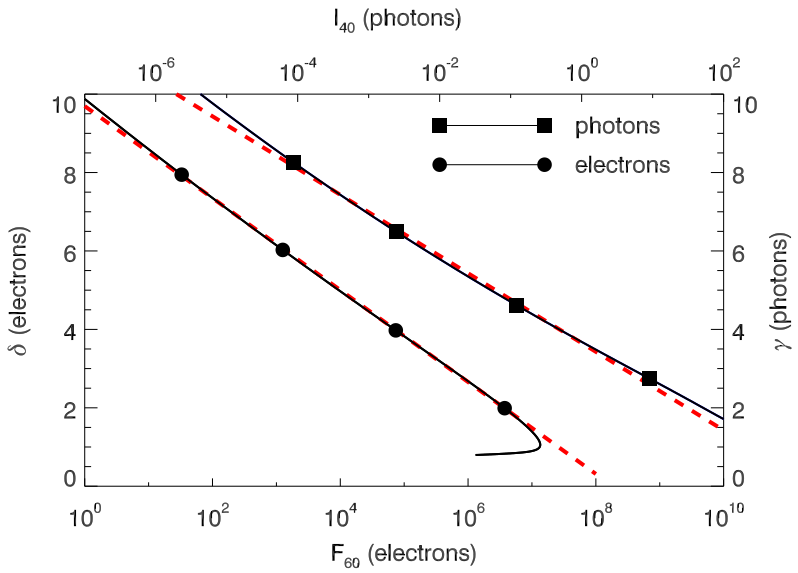

Fig. 9.5 Model results for the spectral index and flux normalization for electrons and photons. The dashed line is the best straight-line fit to the model results (in the range of spectral indices from 2 to 8 for the electrons, and 3 to 9 for the photons), corresponding to a pivot-point behavior (from Grigis & Benz 2006).

turn current losses are significant is proportional to the return current electric field strength, which is in turn proportional to the electron beam flux density (see Section 5). Therefore, as the electron flux density increases and then decreases, the low-energy part of the X-ray spectrum flattens to higher and then lower energies as the return current electric field strength increases and then decreases. The net effect is SHS spectral evolution below the maximum energy for which return current losses are significant during the flare. The observation of SHS behavior in coronal X-ray sources, however, indicates that this spectral evolution is a property of the acceleration mechanism rather than a consequence of energy losses during electron propagation (Battaglia & Benz 2006, see Section 10.3).

Are there two stages of electron acceleration, one responsible for the impulsive phase and one for the gradual phase? *RHESSI* spectroscopy and imaging of a set of 5 flares with hardening phases (Grigis & Benz 2008) showed that there is no discontinuity in the motion of footpoints at the onset of hardening and no clear separation between the impulsive and the gradual phase: the former seems to smoothly merge into the latter. This supports the view that the same acceleration mechanism changes gradually in the later phase of the flare, rather than a two stage acceleration theory. The hardening phase may in fact be caused by an increase in the efficiency of trapping of the electrons above 100 keV.

The underlying cause of the SHS spectral evolution has been addressed in terms of the stochastic acceleration model by Bykov & Fleishman (2009) and Liu & Fletcher (2009). Bykov and Fleishman consider acceleration in strong, long-wavelength MHD turbulence, taking into account the effect of the accelerated particles on the turbulence. They argue that the electron spectrum flattens during the linear acceleration phase, while the spectrum steepens during the nonlinear phase when damping of the turbulence because of the particle acceleration is important, giving SHS spectral evolution. They argue that SHH evolu-

tion will be observed when the injection of particles into the acceleration region is strong. Liu & Fletcher also argue that the SHS evolution results from dependence of the electron distribution power-law index on the level of turbulence as it increases and subsequently decreases. They attribute changes in the SHS correlation during a flare to changes in the background plasma, likely due to chromospheric evaporation.

We note that simple direct-current (DC) electric field acceleration of electrons out of the thermal plasma can produce the SHS spectral evolution. The flux of accelerated electrons and the maximum energy to which electrons are accelerated and, therefore, the high-energy cutoff to the electron distribution, increase and decrease together as the electric field strength increases and decreases (Holman 1985). The X-ray spectrum is steeper at energies within one to two orders of magnitude below the high-energy cutoff (Holman 2003). In large flares, however, where the X-ray spectrum is observed to continue to MeV energies or higher, there is no evidence for a high-energy cutoff in the appropriate energy range. Therefore, at least for large flares with spectra extending to high energies, a simple DC electric field acceleration model does not appear to be appropriate.

10 The connection between footpoint and coronal hard X-ray sources

Hard X-ray (HXR) sources at both footpoints of a coronal loop structure have been observed since Hoyng et al. (1981). As reviewed in Sections 1 & 2, they are understood to be thick-target bremsstrahlung emission produced by precipitating electrons, accelerated somewhere in or above the loop. A third HXR source situated above the looptop (see Krucker et al. 2008a, for a review) was first noted by Masuda et al. (1994) in *Yohkoh* observations. The nature of this coronal HXR source has remained uncertain, but in simple solar flare models with reconnection and particle acceleration in the corona, we expect some relation between coronal HXR sources and footpoints. *RHESSI* has enabled us to study events featuring coronal HXR sources and footpoints simultaneously. By studying the behavior of the sources in time and the relations between them, we can address questions such as: Are both coronal and footpoint emissions caused by the same electron population? How is such an electron beam modified in the loop (collisions, return currents, trapping, etc.)? Is SHS behavior (Section 9.1) a transport effect produced by collisions or return currents, or is it a feature imposed by the acceleration mechanism?

10.1 *RHESSI* imaging spectroscopy

RHESSI has provided the possibility of obtaining simultaneous, high-resolution imaged spectra at different locations on the Sun. One can therefore study each source separately in events with several contemporaneous HXR sources. The high spectral resolution has allowed a reliable differentiation between thermal and non-thermal emission to be made in many flares. Furthermore, *RHESSI*'s imaging spectroscopy has allowed differences in individual flare source spectra and their evolution to be studied in considerable detail.

Imaged spectra and the relative timing of sources in three flares, including the limb flare SOL2002-02-20T11:07, were studied by Krucker & Lin (2002). Sui et al. (2002) analyzed and modeled the two footpoint sources and a high, above-the-looptop hard X-ray source observed in this flare. Emslie et al. (2003) analyzed SOL2002-07-23T00:35 (X4.8) flare with four HXR sources observed by *RHESSI*. They found a coronal source with a strong thermal component, but the non-thermal component could not be studied due to severe pulse pile-up.

Battaglia & Benz (2006) studied five M-class events. Due to the smaller pile-up amount in those events, studying the non-thermal coronal emission was possible. The results of these studies are summarized below.

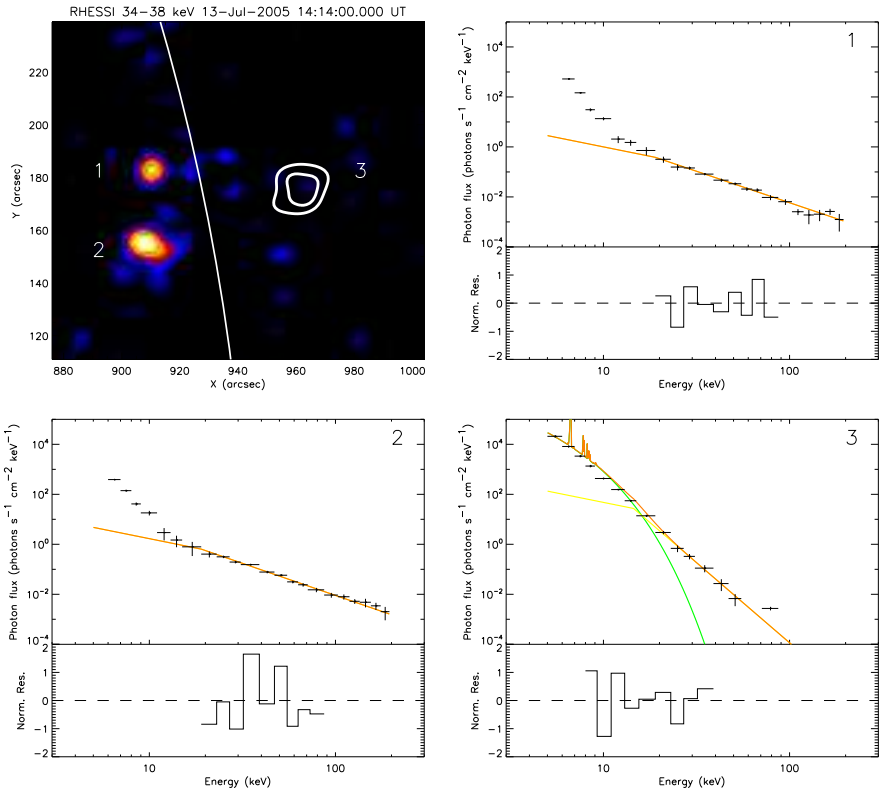

Fig. 10.1 *Top left* Composite CLEAN image of a *RHESSI* event with three hard X-ray sources. The footpoints (labeled 1 & 2) are visible on the solar disc in an image made at 34–38 keV. The position of the coronal source (labeled 3) high above the limb is indicated by the 50 and 80% white contours taken from a 10–12 keV image. *Plots 1-3* show spectra and normalized residuals over the fitted energy range for the north footpoint (1), south footpoint (2), and coronal source (3) (after Battaglia & Benz 2006).

10.2 Relation between coronal and footpoint sources

The quantitative relations between the footpoints and the coronal source and between the two footpoints can give information about the physical mechanisms at work in a solar flare. Simple models envision a beam of accelerated electrons encountering a low-density region in the corona, leading to thin-target bremsstrahlung. When the same electron beam reaches the chromosphere, the particles are fully stopped in the dense material, producing thick-target emission. Assuming an electron power-law distribution for the electron energy E of the form

$$\mathscr{F}(E) = AE^{-\delta} \tag{10.1}$$

producing thin-target bremsstrahlung in the coronal source, the observed photon spectrum has spectral index $\gamma_{thin} = \delta + 1$ (Equation 2.10). Reaching the chromosphere, the accelerated electrons will be fully stopped, producing thick-target bremsstrahlung with a photon spectral index $\gamma_{\rm thick} = \delta - 1$ (Equation 2.12). In such a simple scenario one would therefore expect a difference in the photon spectral index $\gamma_{thin} - \gamma_{thick} = 2$ between the coronal source and the footpoints. Further, the two footpoints should be of equal hardness and intensity if one assumes a symmetric loop and symmetric injection of particles into the legs of the loop.

10.2.1 Observed difference between coronal and footpoint spectral indices

A sample of flares observed with *Yohkoh* to have coronal HXR sources was studied by Petrosian et al. (2002). They found that the spectral index of the coronal sources was, on the average, steeper by 1 than the spectral indices of the footpoint sources. Sui et al. (2002) also found a spectral index difference of 1 for SOL2002-02-20T11:07 (C7.5) observed with *RHESSI*.

Battaglia & Benz (2006) found that the coronal source was softer than both footpoints for all of their five events in nearly all analyzed time bins. Figure 10.1 (top left) shows an image of SOL2005-07-13T14:49 (M5.0) in the 34-38 keV energy band. The two footpoints are visible, as well as the 50 and 80% contours of the coronal source taken from a 10–12 keV image. Spectra and spectral fits are shown for the two footpoints and the coronal source. The steepness of the coronal source spectrum (number 3 in the figure) relative to the spectra from the footpoints is apparent. However, the quantitative difference between the values of the spectral index obtained for the coronal source and the footpoints often differed significantly from 2. For the five flares analyzed, the smallest mean difference in the spectral indices, averaged over time, was 0.59 ± 0.24. The maximum mean difference, averaged over time, was 3.68 ± 0.14. These clearly contradict the theoretical expectation summarized above. Simple thin-thick target scenarios do not seem to work in most cases and additional effects need to be considered.

Evidence for two populations of coronal source non-thermal spectra was found by Shao & Huang (2009a). They compare coronal and footpoint spectral indices at 28 hard X-ray peaks from 13 single-loop flares observed by *RHESSI*. The spectral index in the coronal sources was determined from an isothermal plus power-law fit below 30 keV, while the footpoint spectral indices were determined from a power-law fit at 30-60 keV photon energies. They argue that the coronal spectra can be divided into two groups. One, for which the coronal spectral index is greater than 5, is well correlated with the footpoint spectral index, and the difference in the indices ranges from 2-4. For the other, where the spectral indices are anticorrelated, the coronal spectral index is less than 5, and the difference in the indices ranges from 0-2. For the group of anticorrelated spectral indices, the coronal spectral index is correlated with the photon flux, while the footpoint spectral index is anticorrelated with the photon flux for both groups. These are intriguing results if confirmed by future studies.

10.2.2 Differences between footpoints

No significant difference was found in the spectral indices for the two footpoints in SOL2002-02-20T11:49 (C7.5) by Krucker & Lin (2002) and Sui et al. (2002). Piana et al. (2007) inverted count visibility spectra for this flare to obtain mean electron flux distributions for the footpoints. They found the mean electron flux distribution function at the northern footpoint to be somewhat steeper ($\Delta\delta \approx 0.8$) than that derived for the southern footpoint. They also found the distribution function for the region between the footpoints (not the coronal

source studied by Sui et al.) to be steeper than the footpoint distribution functions ($\Delta\delta \approx 1.6$ relative to the southern footpoint) and to substantially steepen at energies above $\sim$60 keV.

Krucker & Lin (2002) found that, when a connection between footpoints could be determined, the footpoints brightened simultaneously (to within the $\sim$1 s time resolution of the observations) and had similar spectra.

Differences of 0.3 – 0.4 between the spectral indices of two footpoints in SOL2002-07-23T00:35 (X4.8) were reported by Emslie et al. (2003).

For the flares analyzed by Battaglia & Benz (2006), a significant difference was found in only one out of five events. For all other events, the mean difference in $\gamma_{\rm fp}$ was zero within the statistical uncertainty.

Different spectra at the two footpoints imply an asymmetric loop. Such an asymmetry can result, for example, from different column densities or different beam fluxes and corresponding return current energy losses in the legs of the loop. It could also result from asymmetric magnetic trapping within the loop (e.g., Alexander & Metcalf 2002). In a study of 53 flares showing two HXR footpoints, Saint-Hilaire et al. (2008) found that footpoint asymmetry was greatest at the time of peak HXR flux and the difference in the footpoint spectral indices $\Delta\gamma$ rarely exceeded 0.6. In most cases they found the footpoint asymmetry to be inconsistent with different column densities in the two legs of the loops.

In SOL2003-10-29T20:49 (X10.0) Liu et al. (2009a) found that the brighter HXR footpoint was marginally, but consistently harder than the dimmer footpoint by $\Delta\gamma = 0.15 \pm 0.13$. They concluded that neither asymmetric magnetic mirroring nor asymmetric column density *alone* can explain the full time evolution of the footpoint HXR fluxes and spectral indices. However, a self-consistent explanation might be obtained by considering these two effects together and/or in combination with one or more additional transport effects, such as nonuniform target ionization, relativistic beaming, and return current losses.

10.3 Spectral evolution in coronal sources

Previous observations of SHS spectral evolution (see Section 9.1) were made with full-Sun spectra which, except for over-the-limb events, are typically dominated by footpoint emission. Battaglia & Benz (2006), in their imaging spectroscopy study, found that the coronal source itself shows SHS evolution. This is illustrated in Figure 10.2. This finding implies that SHS is not caused by transport effects within the flare loop, but is rather a property of the acceleration mechanism itself. Indeed, Grigis & Benz (2006) showed that SHS can be reproduced for electron spectra in a transit-time-damping, stochastic-acceleration model (Section 9.2).

10.4 Interpretation of the connection between footpoints and the coronal source

In the above account, emphasis was given to the difference in the spectral index between the coronal source and footpoints. Assuming a thin target in the corona and a thick target at the footpoints, one would expect a difference of two. However, whether the coronal source acts as thin- or thick-target depends on the energy of the accelerated electrons and the column density in the corona. Veronig & Brown (2004), for example, found coronal sources with column densities high enough to act as thick targets for electrons with energies up to 60 keV.

As early as 1976, Melrose & Brown (1976) showed that magnetic trapping with collisional scattering of electrons out of the trap can lead to a thick-target coronal source. The

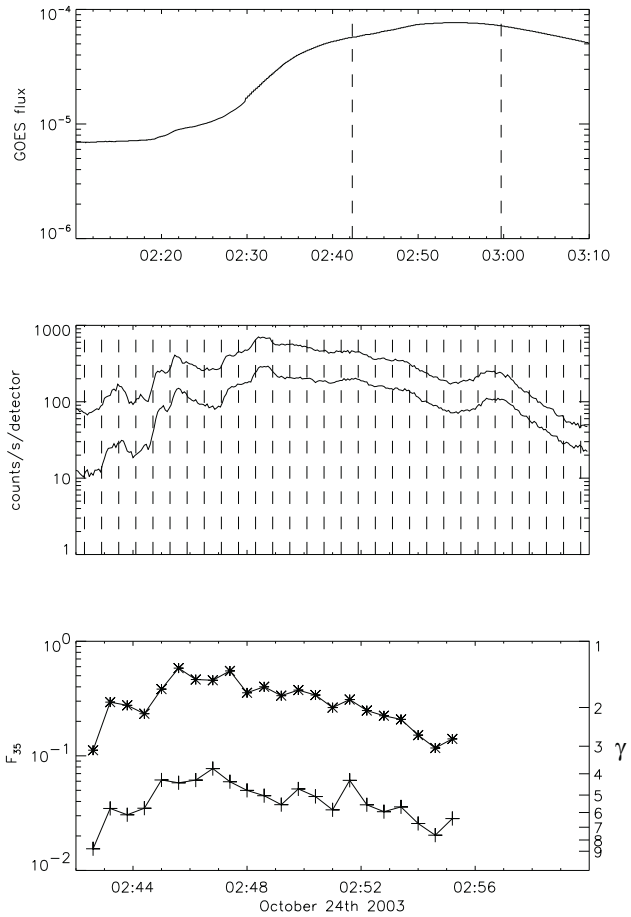

Fig. 10.2 *Top: GOES* 1–8 Å light curve of SOL2003-10-24T02:54 (M7.6). *Middle: RHESSI* 25–50 and 50–100 keV light curves near the peak of the *GOES* flare. *Bottom:* time evolution of fitted coronal source flux at 35 keV (F_{35}, * symbols, left log scale) and spectral index (γ, + symbols, right log scale) displaying SHS evolution (after Battaglia & Benz 2006).

coronal source transitions through a thin-thick period, with the time scale for this transition depending on the electron energy and the plasma density in the trap. The trapping essentially increases the effective column density in the corona. Metcalf & Alexander (1999) analyzed six flares with coronal sources observed by *Yohkoh* and found that three of the six flares showed properties consistent with trapping.

A simple 1-D model that described the coronal emission as intermediate thin-thick, depending on electron energy, was developed by Wheatland & Melrose (1995). In this model a high-density region ($\gtrsim 10^{12}$ cm^{-3}) is hypothesized to be present at or above the top of the flare loop. The model makes predictions for the shape of the coronal and footpoint spectra and the relations between them. Fletcher (1995) obtained Monte Carlo solutions to the Fokker-Planck equation to show that, with the inclusion of high electron pitch angles and collisional scattering, a compact coronal X-ray source is produced at the top of a loop with a constant coronal density $\sim 3 \times 10^{10}$ cm^{-3}. Holman (1996) showed that, even in the simple 1-

D model, a compact coronal source is produced when electrons are injected into a loop with a constant coronal density $\sim 2 \times 10^{11}$ cm^{-3} (see *hesperia.gsfc.nasa.gov/sftheory/loop.htm*). A compact coronal HXR source can also be produced if there is a compact magnetic trap at or above the top of the loop. Fletcher & Martens (1998) showed that, with such a trap, a significant coronal X-ray source can be produced at plasma densities as low as $\sim 4 \times 10^9$ cm^{-3}. Petrosian & Donaghy (1999) showed that the coronal HXR source can be a consequence of acceleration and trapping by turbulence or plasma waves. In their stochastic acceleration model, the difference between the coronal and footpoint spectra is explained by the energy-dependent time scale for electrons to escape the acceleration region.

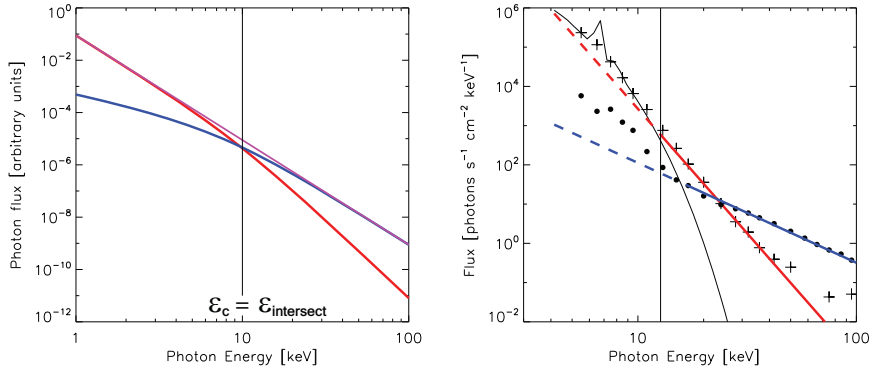

Fig. 10.3 *Left:* spectra for coronal source (red) and footpoints (blue) according to the model of Wheatland & Melrose (1995). The spatially integrated spectrum is shown in violet. *Right:* observed *RHESSI* spectra for the event SOL2003-10-24T02:54 (M7.6). Isothermal and power-law fits to the coronal (crosses) and footpoint (dots) spectra are shown. The vertical line indicates the predicted critical energy for the transition between thin and thick target (after Battaglia & Benz 2007).

The left panel of Figure 10.3 illustrates the model of Wheatland & Melrose (1995). The spatially integrated spectrum (violet) is the power-law spectrum (thick-target, $\gamma_{thick} = \delta - 1$) expected for a single-power-law electron distribution with no low- or high-energy cutoffs and no thermal component. For $\varepsilon \ll \varepsilon_c = \sqrt{2KN}$ (see Equation 2.4), the spectrum is dominated by thick-target radiation from the coronal source (red). There is a low-energy cutoff in the electron distribution at the footpoints at $E \approx \sqrt{2KN}$ because of the energy losses in the coronal source. The spectrum is dominated by thick-target radiation from the footpoints (blue) where $\varepsilon \gg \varepsilon_c$. It is in this regime that the radiation from the coronal source is thin-target and the spectral index of the coronal source is steeper by 2 than that of the footpoints. These spectra are characteristic of all the models reviewed above.

Sui et al. (2002) compared the *RHESSI* observations of SOL2002-02-20T11:07 (C7.5) to a model with a constant-coronal-density loop and no magnetic trapping. They used a finite difference method (e.g., McTiernan & Petrosian 1990; Holman et al. 2002) to obtain steady-state solutions to the Fokker-Planck equation with collisional scattering and energy losses. Model images were convolved with the *RHESSI* response to produce simulated *RHESSI* observations for direct comparison with the SOL2002-02-20T11:07 flare images and imaged spectra. They found that, after obtaining a power-law model spectrum with an index of $\gamma = 3$ that agreed with the observed footpoint spectra, the effective spectral index of the coronal

source from the model ($\gamma = 4.7$) was significantly steeper than that obtained for the flare ($\gamma = 4$).

Battaglia & Benz (2007) compared the model of Wheatland & Melrose (1995) to the results of their study of five flares observed by *RHESSI*. The right panel of Figure 10.3 shows observed spectra and spectral fits for one particular event. The observed spectra were dominated by thermal coronal emission at low energies. Therefore, not all of the model predictions could be tested. However, the observed relations between the spectra did not agree with the predictions of the model. For the flare in Figure 10.3, for example, the difference between the coronal source and footpoint spectral indices at the higher photon energies is 3.8 ± 0.1, not 2. Also, an estimate of the column density in the coronal source gives $\sqrt{2KN} \approx$ 10-15 keV, while the intersection of the coronal and footpoint spectra is found to be at $\varepsilon \approx 23$ keV. Battaglia & Benz (2008) have found that this large difference in the spectral indices is consistent with spectral hardening caused by return current losses (see Section 5).

11 Identification of electron acceleration sites from radio observations

While energetic electrons excite hard X-ray emission during their precipitation into the dense layers of the solar atmosphere, they can also excite decimeter and meter wave radio emission during propagation and trapping in magnetic field structures in the dilute solar corona. The radio emission pattern in dynamic spectrograms can give information about the electron acceleration process, the locations of injection of electrons in the corona, and the properties of the coronal magnetoplasma structures.

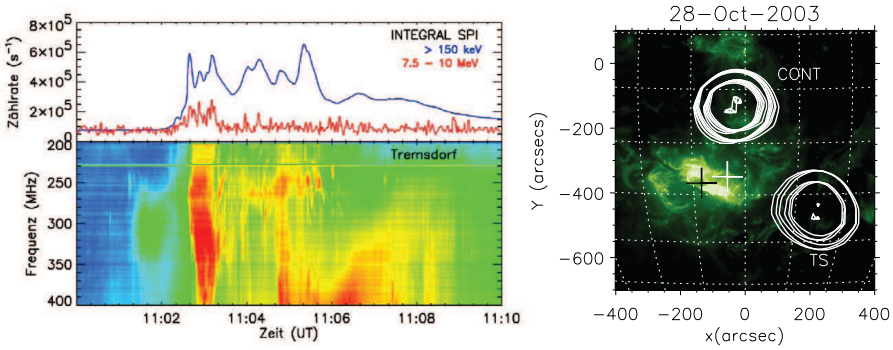

Fig. 11.1 SOL2003-10-28T11:10 (X17.2). *Left, bottom:* (see Warmuth et al. 2007) 200-400 MHz radio spectrum (Astrophysical Institute Potsdam) showing the signature of the outflow termination shock (TS, starting at 11:02:47 UT). *Left, top*: *INTEGRAL* count rates at 150 keV and 7.5–10 MeV. *Right:* (after Aurass et al. 2007): radio source positions (Nançay Radio Heliograph, 327 MHz) overlaid on a *SOHO*-EIT image (11:47 UT 195 Å). The bright areas are EUV flare ribbons in AR10486. *RHESSI* HXR centroids are shown as "+". The integration time intervals are: for the TS source SW of AR10486 11:02:45–11:03:15 UT, for the continuum source CONT N of AR10486 11:13–11:17 UT, respectively (see also Figure 11.2). The radio contours are at 50, 70, and 99.5% of the peak flux value.

Here we take as an example SOL2003-10-28T11:10 (X17.2) (shown in Figure 11.1). Different acceleration sites can be discriminated during the impulsive and the gradual flare phases. Radio spectral data from the Astrophysical Institute Potsdam (AIP; Mann et al.

1992), imaging data from the Nançay Radio Heliograph (NRH, Kerdraon & Delouis 1997), and hard X-ray (*RHESSI*, *INTEGRAL*) data were combined in the analysis of this event. The conclusion was reached that a nondrifting, high-frequency type II radio burst signature in the radio spectrum coincided with a powerful electron acceleration stage. Simultaneously with the nondrifting type II signature, highly relativistic ($\geq$10 MeV) electrons were observed in the impulsive phase of the flare (Figure 11.1, upper left). The radio spectrum suggests that this can be due to acceleration at the reconnection outflow termination shock (Aurass & Mann 2004), as predicted for a classical two-ribbon flare (Forbes 1986, Tsuneta & Naito 1998, Aurass et al. 2002). The radio source site is observed about 210 Mm to the SW of the flaring active region (TS in Figure 11.1, right). In this direction, *TRACE* and *SOHO*/LASCO[1] C2 images reveal dynamically evolving magnetoplasma structures in an erupting arcade (Aurass et al. 2006). For realistic parameters derived from these observations (the geometry, density, temperature, and low magnetic field values of $\sim$5 Gauss), Mann et al. (2006) have found that a fully relativistic treatment of acceleration at the fast-mode outflow shock can explain the observed fluxes of energetic particles (see Zharkova et al. 2011).

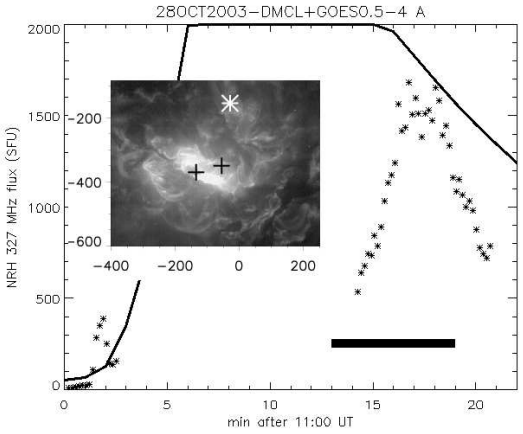

Fig. 11.2 Timing of the source CONT in Figure 11.1: the NRH 327 MHz flux curve (asterisks) versus the *GOES* 0.5-4 Å flux curve (solid line, partly off-scale). Inset: *SOHO*/EIT image showing the radio source centroid (white asterisk) and *RHESSI* HXR centroids as in Figure 11.1. Thick bar: the start time of GeV-energy proton injection in space (after Aurass et al. 2007).

In the main flare phase of the same event, an additional radio source (CONT in Figure 11.1) was found, lasting for $\sim$10 min, indicating the presence of another acceleration site. No X-ray, EUV, or Hα emission was observed at the location of this radio source. Figure 11.2 gives the timing and the source position with respect to the flaring active region. CONT is a m-dm-continuum source with fiber burst fine structure. Fiber bursts are excited by whistler waves propagating along field lines of the coronal magnetic field. As marked by a bold bar in the Figure, the time of the CONT emission is also the start time of GeV proton injection in space. Aurass et al. (2006) have shown that this source site is not far from an open field (particle escape) region in the potential coronal magnetic field. The source briefly

[1] Large Angle and Spectrometric Coronagraph

flashes up already in the early impulsive phase. Based on a new method of fiber burst analysis (Aurass et al. 2005; Rausche et al. 2007), Aurass et al. (2007) argue that this source most likely indicates acceleration at a contact between separatrix surfaces of different magnetic flux systems.

Radio observations of flares and their implications are further addressed in White et al. (2011).

12 Discussion and Conclusions

12.1 Implications of X-ray observations for the collisional thick-target model

As discussed in Section 2, the core assumption of the collisional thick-target model is that the spatially integrated hard X-ray emission from non-thermal electrons is bremsstrahlung (free-free radiation) from electrons that lose all their suprathermal energy through collisional losses in the ambient plasma as they simultaneously radiate the hard X-rays. "Simultaneously" means within the observational integration time. This implies that all electrons that contribute significantly to the observed radiation reach a plasma dense enough or, more precisely, traverse a high enough column density for all of their suprathermal energy above the observed photon energies to be collisionally lost to the ambient plasma within the integration time. For typical $\gtrsim$1 s integration times, these conditions are met when the electrons stream downward from the corona into the increasingly dense plasma of the solar transition region and chromosphere.

Since the thick-target model is often implicit in our interpretation of the hard X-ray emission from flares, it is important to keep the underlying assumptions in mind and test the model while at the same time applying it to flare observations. We have discussed above several physical processes that, if significant, change the conclusions of the simple collisional thick-target model regarding the electron distribution produced in the acceleration region. These processes occur in either the thick-target region itself, or during the propagation of the electrons from the acceleration region to the thick-target region. Only with the high spectral resolution and imaging of *RHESSI* has it become possible to observationally address these processes. Even with the *RHESSI* observations, however, it is difficult to conclusively determine the importance of each process.

A physical process that distorts the emitted X-ray spectrum is albedo (Section 3.4 and Kontar et al. 2011). Fortunately, the albedo contribution to the X-ray spectrum can be easily corrected on the assumption that the X-ray photons are isotropically emitted. This correction is available in the *RHESSI* spectral analysis software. If the photons are significantly beamed downward, however, the distortion of the spectrum can be substantially greater than that from isotropically emitted photons. An anisotropic photon distribution results from emitting electrons with an anisotropic pitch-angle distribution. The degree of anisotropy of the electron pitch-angle distribution also quantitatively affects conclusions from the thick-target model concerning the acceleration process. Therefore, it is important to better determine the pitch-angle distribution of the emitting electrons and the contribution of albedo to the hard X-ray spectrum (see Kontar et al. 2011).

The simple collisional thick-target model assumes that the target plasma is fully ionized. We have seen, however, that a nonuniformly ionized target region can produce an upward kink, or "chicane," in an otherwise power-law X-ray spectrum (Section 4). This spectral shift can provide a valuable diagnostic of the ionization state of the target plasma and its evolution. It is likely, however, that the power-law spectrum below the chicane is hidden by

thermal radiation. The chicane is then observed only as a downward break in the spectrum at energies above those dominated by the thermal emission. The upper limit on the magnitude of the break provides a method for ruling out nonuniform ionization as the sole cause of large spectral breaks. To further distinguish this break from spectral breaks with other causes, it is important to better determine the degree of ionization as a function of column density at the thick-target footpoints.

Return-current energy losses can also produce a downward break in the X-ray spectrum (Section 5). The break energy depends on both the thermal structure of the plasma in the flare loop and on the non-thermal electron flux density distribution. These spectral modifications and their evolution throughout flares provide an important test for the presence of initially un-neutralized electron beams and the return currents they must drive to neutralize them. Although *RHESSI* observations provide substantial information about the structure and evolution of flare spectra, only a lower limit on the electron flux density can usually be determined. Observations and analysis sufficiently accurate and comprehensive to verify the presence of return current energy losses as the cause of a spectral break are yet to be obtained. On the other hand, significant evidence exists (Section 5.3) indicating that return current losses do have an impact on flare hard X-ray emission.

A thorough comparison of measured flare spectra with theoretical spectra computed from models incorporating collisional and return current energy losses (including their effect on the angular distribution of the non-thermal electrons), as well as nonuniform target ionization and albedo, is still needed. Spectral fitting alone, however, is not likely to distinguish the importance of these different mechanisms. Comparison of the time evolution of the spectra, as well as of the spatial structure of the X-ray emission, with expectations would certainly enhance the possibility of success for such an endeavor.

The analysis of the evolution of X-ray source positions and sizes with photon energy and time provides another important test of the collisional thick-target model (Section 7). For these flares that show non-thermal source evolution in the corona and upper transition region, the source position and size are sensitive to the energy losses experienced by the non-thermal electrons. They are, in fact, sensitive to the very assumption that the sources are produced by electrons as they stream downward from an acceleration region higher in the corona. Further studies of the evolution of these coronal X-ray sources should substantially clarify the applicability of the collisional thick-target model.

For completeness, we note that under some circumstances other radiation mechanisms may significantly contribute to the X-ray emission from non-thermal electrons. The possibility that recombination (free-bound) radiation from the non-thermal electrons is sometimes important is discussed in Brown & Mallik (2008, 2009) (also see Kontar et al. 2011). However, the contribution of non-thermal free-bound radiation has recently been found to be less significant than originally estimated (Brown et al. 2010). MacKinnon & Mallik (2010) have concluded that inverse Compton radiation may significantly contribute to the X-ray/γ-ray emission from low-density coronal sources.

Another testable aspect of the collisional thick-target model is the heating of the flare plasma by the non-thermal electrons. If the flare plasma is primarily heated by these electrons and the thick-target region is primarily in the chromosphere and lower transition region, heating originating in the footpoints and expanding into the rest of the flare loop through “chromospheric evaporation” should be observed. On the other hand, if the loop is dense enough for the thick-target region to extend into the corona or if return-current heating is important, localized coronal heating and different ion abundances should be observed.

It has generally been difficult to establish a clear connection between the location and evolution of X-ray sources produced by non-thermal electrons and by thermal plasma at

different temperatures. This is largely because of a lack of high-cadence EUV images covering a broad range of coronal and transition region temperatures prior to the launch of *SDO*. Future studies of the coevolution of non-thermal X-ray sources and thermal sources in flares will be important in determining the extent to which heating mechanisms other than collisional heating by non-thermal electrons is significant.

Predicting the expected evolution of the heated plasma is hampered by insufficient knowledge of the dominant heat transport mechanisms. We have seen evidence that many flares cool by classical thermal conduction or radiation once the heating has subsided (Section 8.4), but this is not likely to be the dominant transport mechanism during rapid heating. Nevertheless, the spatial evolution of flare X-ray sources has so far been found to be consistent with chromospheric evaporation (Section 7.2). Also, the Neupert effect, observed in most flares, and Doppler-shift measurements qualitatively support the thick-target model (Section 8.3), but these do not rule out the possibility of other heating mechanisms temporally correlated with the electron beam collisional heating. As discussed in Section 3, substantial progress has been made in deducing the energy flux (total power) carried by non-thermal electrons, but we usually can deduce only a lower limit to this energy flux. Continuing studies of flares similar to SOL2002-04-15T03:55 (M1.2) and the initially cooler, early-impulsive flares (Section 3.5) may provide a better handle on this energy flux for comparison with thermal evolution. The thermal properties, energetics, and evolution of flares are discussed further in Fletcher et al. (2011).

12.2 Implications of X-ray observations for electron acceleration mechanisms and flare models

In Section 10 we addressed the X-ray spectra of hard X-ray sources sometimes observed above the top of the hot loops or arcades of loops observed in flares. We reviewed results indicating that the spectra are qualitatively, but not quantitatively consistent with expectations for electrons passing through a thin-target or quasi-thick-target region on their way to the thick-target footpoints of the flare loops. The apparent failure of these relatively simple models is probably a manifestation of the more complex above-the-looptop X-ray source structure revealed by *RHESSI* observations.

Before *RHESSI*, time-of-flight delays in hard X-ray timing indicated that electrons were accelerated in a region somewhat above the looptops of the hot flare loops in most flares (Section 8.1). Also, cusps were observed at the top of flare loops by *Yohkoh* (e.g., Section 10), indicating a magnetic connection to the region above the hot loops.

RHESSI images have revealed flares with double coronal sources, one at or just above the top of the hot loops and the other at a higher altitude above the lower source. The centroid of the lower source is higher in altitude at higher X-ray energies, while the centroid of the upper source is lower in altitude at higher X-ray energies, indicating that energy release occurred between these coronal sources (Sui & Holman 2003; Sui et al. 2004; Liu et al. 2008, 2009b). In one flare, the upper source accelerated outward to the speed of a subsequent coronal mass ejection. The white-light coronagraph on the *Solar Maximum Mission* (Webb et al. 2003), the Large Angle and Spectrometric Coronagraph (LASCO) and the Ultraviolet Coronagraph Spectrometer (UVCS) on *SOHO* (Ko et al. 2003; Lin et al. 2005), *RHESSI* (Sui et al. 2005b), and *TRACE* (Sui et al. 2006a) have all provided direct evidence for the presence of an extended, vertical current sheet above the hot flare loops and below the coronal mass ejection associated with eruptive flares. These and related observations are discussed further in Fletcher et al. (2011).

These recent observations strongly support the "standard" model of eruptive solar flares, in which the hot flare loops build up below a vertical current sheet where inflowing magnetic fields reconnect and a magnetic flux rope forms above the current sheet to become a coronal mass ejection (see Fletcher et al. 2011; Zharkova et al. 2011). The rate of electron acceleration has been observed to be correlated with the rate at which magnetic flux is swept up by the expanding footpoints of flare loops and with the rate of looptop expansion (Qiu et al. 2004; Sui et al. 2004; Holman 2005), indicating that the electron acceleration rate is correlated with the rate of magnetic reconnection. On the other hand, the observations also indicate that the rate of electron acceleration in the impulsive phase of flares is greatest *before* a large-scale current sheet or soft X-ray cusp is observed (Sui et al. 2008).

Initially, when the electron acceleration rate is highest, the current sheet may be short and associated with slow-mode shock waves, as in Petschek reconnection. Fast reconnection jets (e.g., Wang et al. 2007) can stream upward and downward from the current sheet, possibly ending in fast-mode shock waves where they collide with slower magnetized plasma at the flare loop tops and the lower boundary of the magnetic flux rope (termination shocks). The pair of above-the-looptop X-ray sources may be associated with these fast-mode shock waves. We have described possible evidence for these shock waves from radio observations in Section 11.

The most difficult task is determining the dominant acceleration mechanism or mechanisms responsible for the energetic particles. The region above the flare loops contains or can contain quasi-DC electric fields, plasma turbulence, slow- and fast-mode shock waves, and collapsing magnetic traps, allowing for almost any acceleration mechanism imaginable. The problem is as much one of ruling out mechanisms as of finding mechanisms that work (cf. Miller et al. 1997). Acceleration mechanisms are addressed in Zharkova et al. (2011).

In Section 9 we addressed the soft-hard-soft evolution of flare X-ray spectra. This spectral evolution could occur during the propagation of the electrons from the acceleration region to the thick-target footpoints. Return current losses, with their dependence on the electron beam flux (Section 5), for example, could be responsible for this evolution. However, the observation that above-the-looptop sources also show this spectral evolution (Section 10.3) indicates that it is a property of the acceleration process rather than electron beam propagation. We saw in Section 9.2 that the soft-hard-soft behavior can be reproduced in the acceleration region if the acceleration or trapping efficiency first increases and then decreases.

Flares displaying soft-hard-harder spectral evolution are of special interest, because they have been shown to be associated with high-energy proton events in space (Kiplinger 1995; Saldanha et al. 2008; Grayson et al. 2009). What is the connection between the appearance of energetic protons in space and X-ray spectral hardening late in flares? The answer to this question is important to both space weather prediction and understanding particle acceleration in flares.

12.3 Implications of current results for future flare studies in hard X-rays

What characteristics should a next-generation hard X-ray telescope have to make substantial progress in understanding electron propagation and acceleration in flares? The advances made with *RHESSI* have depended on its high-resolution count spectra that could generally be convolved with the detector response to obtain reliable photon flux spectra. These have been the first observations to allow detailed information about the evolution of accelerated electrons and associated hot flare plasma to be deduced for many flares. Equally important

has been the ability to produce hard X-ray images in energy bands determined by the user during the data analysis process. This imaging capability has been critical to determining the origin of the X-ray emission at a given photon energy and in obtaining spectra for individual imaged source regions. These high-resolution imaging spectroscopy capabilities will remain important for continued progress.

RHESSI's X-ray imaging capability has allowed a clear spatial separation to be made for many flares between footpoint sources with non-thermal spectra at higher energies and loop-top sources with thermal spectra at lower energies. However, in the energy range of overlap between $\sim$10 keV and 50 keV, where both types of sources may coexist, it is often difficult to distinguish weaker coronal sources (both thermal and non-thermal) in the presence of the stronger footpoint sources. This is because of the limited dynamic range of $<$100:1 (and significantly less for weaker events) that is possible in any one image made from *RHESSI* data. This is a consequence of the particular form of the Fourier-transform imaging technique that is used. Thus, in most flares the usually intense footpoints mask the much weaker coronal hard X-ray sources that can sometimes be seen in over-the-limb flares when the footpoints are occulted (e.g., Krucker & Lin 2008). In fact, these coronal hard X-ray sources can extend to high energies (up to $\sim$800 keV, Krucker et al. 2008b) and seem to be non-thermal in origin, thus making them of great interest in locating and understanding the particle acceleration process. It is important to study these non-thermal coronal sources in comparison with the footpoint sources, something that is currently not possible with *RHESSI*'s limited dynamic range except in the few cases with exceptionally strong coronal emission (see Section 10). In addition, again because of the *RHESSI* dynamic range and sensitivity limitations, it has not generally been possible to observe the thin-target bremsstrahlung emission from the corona that must be present from the electrons streaming down the legs of magnetic loops and also from electrons streaming out from the Sun and producing type-III bursts (see, however, Krucker et al. 2008c; Saint-Hilaire et al. 2009). For all of these reasons, a significantly greater dynamic range will be an important goal for future advanced solar hard X-ray instruments.

Flares at the solar limb for which the hard X-ray footpoints are occulted by the disk provide an important way of observing coronal hard X-ray sources, but these flares do not allow a comparison to be made between the coronal emission and the thick-target footpoint emission. A possible substitute for a high-dynamic-range instrument is hard X-ray observations from two or more spacecraft. Under the right conditions, one spacecraft can observe all the flare emission while the other observes only the coronal emission, with the footpoint emission occulted by the solar disk. Multi-spacecraft observations would also be important for deducing the directivity of the flare emission (especially in conjunction with X-ray polarization measurements – see Kontar et al. 2011) and 3-D source structure. This multi-spacecraft approach, however, limits the number of flares for which the coronal and footpoint emissions can be compared.

Hard X-ray timing studies have provided valuable information about electron propagation and the location of the acceleration region (Section 8). Since the time of flight of energetic electrons from a coronal acceleration region to the thick-target loop footpoint is typically $\sim$10–100 milliseconds, the photon count rate must be high enough to distinguish differences in flux on these time scales. Time-of-flight studies have not been successful with *RHESSI*, because of its relatively low collecting area and, therefore, count rate. An instrument with the collecting area and pulse-pileup avoidance of *CGRO*/BATSE, and the imaging and spectral resolution of *RHESSI*, would provide a new generation of studies on the characteristic time scales of propagation for the hard-X-ray-emitting electrons accelerated in flares. Alternatively, smaller instruments sent closer to the Sun on, for example, *Solar Or-*

biter or *Solar Probe* could achieve the required sensitivity. Flare studies on these time scales would provide important insights into the physical processes that impact the acceleration and propagation of energetic electrons in flares.

Acknowledgements We thank the chapter editor, Brian Dennis, and the two reviewers for comments that led to many improvements to the text. GDH acknowledges support from the *RHESSI* Project and NASA's Heliophysics Guest Investigator Program. MJA acknowledges support from NASA contract NAS5-98033 of the *RHESSI* mission through University of California, Berkeley (subcontract SA2241-26308PG), and NASA contract NAS5-38099 for the *TRACE* mission. HA acknowledges support by the German Space Agency *Deutsches Zentrum für Luft- und Raumfahrt* (DLR), under grant No. 50 QL 0001. MB acknowledges support by the Leverhulme Trust. PCG acknowledges support from NASA contract NNM07AB07C. EPK acknowledges support from a Science and Technology Facilities Council Advanced Fellowship. NASA's Astrophysics Data System Bibliographic Services have been an invaluable tool in the writing of this article.

References

N. Agueda, D. Lario, R. Vainio, B. Sanahuja, E. Kilpua, S. Pohjolainen, Astron. Astrophys. **507**, 981 (2009), doi:10.1051/0004-6361/200912224

D. Alexander, A. G. Daou, Astrophys. J. **666**, 1268 (2007), doi:10.1086/520331

D. Alexander, T. R. Metcalf, Solar Phys. **210**, 323 (2002), doi:10.1023/A:1022457413628

S. K. Antiochos, P. A. Sturrock, Astrophys. J. **220**, 1137 (1978), doi:10.1086/155999

M. J. Aschwanden, Astron. Astrophys. Suppl. **85**, 1141 (1990)

M. J. Aschwanden, *Physics of the Solar Corona. An Introduction* (Physics of the Solar Corona, 2004)

M. J. Aschwanden, Astrophys. J. **661**, 1242 (2007), doi:10.1086/516814

M. J. Aschwanden, D. Alexander, Solar Phys. **204**, 91 (2001), doi:10.1023/A:1014257826116

M. J. Aschwanden, J. C. Brown, E. P. Kontar, Solar Phys. **210**, 383 (2002), doi:10.1023/A:1022472319619

M. J. Aschwanden, R. M. Bynum, T. Kosugi, H. S. Hudson, R. A. Schwartz, Astrophys. J. **487**, 936 (1997), doi:10.1086/304633

M. J. Aschwanden, T. Kosugi, H. S. Hudson, M. J. Wills, R. A. Schwartz, Astrophys. J. **470**, 1198 (1996), doi:10.1086/177943

M. J. Aschwanden, R. A. Schwartz, Astrophys. J. **455**, 699 (1995), doi:10.1086/176617

M. J. Aschwanden, R. A. Schwartz, D. M. Alt, Astrophys. J. **447**, 923 (1995), doi:10.1086/175930

M. J. Aschwanden, R. A. Stern, M. Güdel, Astrophys. J. **672**, 659 (2008), 0710.2563, doi:10.1086/523926

H. Aurass, G. Mann, Astrophys. J. **615**, 526 (2004), doi:10.1086/424374

H. Aurass, G. Mann, G. Rausche, A. Warmuth, Astron. Astrophys. **457**, 681 (2006), doi:10.1051/0004-6361:20065238

H. Aurass, G. Rausche, G. Mann, Astron. Astrophys. **471**, L37 (2007), doi:10.1051/0004-6361:20077544

H. Aurass, G. Rausche, G. Mann, A. Hofmann, Astron. Astrophys. **435**, 1137 (2005), doi:10.1051/0004-6361:20042199

H. Aurass, B. Vršnak, G. Mann, Astron. Astrophys. **384**, 273 (2002), doi:10.1051/0004-6361:20011735

T. S. Bastian, A. O. Benz, D. E. Gary, ARAA **36**, 131 (1998), doi:10.1146/annurev.astro.36.1.131

M. Battaglia, A. O. Benz, Astron. Astrophys. **456**, 751 (2006), arXiv:astro-ph/0606353, doi:10.1051/0004-6361:20065233

M. Battaglia, A. O. Benz, Astron. Astrophys. **466**, 713 (2007), arXiv:astro-ph/0702309, doi:10.1051/0004-6361:20077144

M. Battaglia, A. O. Benz, Astron. Astrophys. **487**, 337 (2008), arXiv:0806.1701, doi:10.1051/0004-6361:200809418

M. Battaglia, P. C. Grigis, A. O. Benz, Astron. Astrophys. **439**, 737 (2005), arXiv:astro-ph/0505154, doi:10.1051/0004-6361:20053027

S. G. Benka, G. D. Holman, Astrophys. J. **435**, 469 (1994), doi:10.1086/174829

A. Benz (ed.), *Plasma Astrophysics, second edition*, volume 279 of *Astrophysics and Space Science Library* (2002)

A. O. Benz, Astrophys. J. **211**, 270 (1977)

J. W. Brosius, G. D. Holman, Astrophys. J. Lett. **659**, L73 (2007), doi:10.1086/516629

J. C. Brown, Solar Phys. **18**, 489 (1971)

J. C. Brown, Solar Phys. **28**, 151 (1973)

J. C. Brown, M. J. Aschwanden, E. P. Kontar, Solar Phys. **210**, 373 (2002), doi:10.1023/A:1022469402781

J. C. Brown, A. G. Emslie, G. D. Holman, C. M. Johns-Krull, E. P. Kontar, R. P. Lin, A. M. Massone, M. Piana, Astrophys. J. **643**, 523 (2006), doi:10.1086/501497

J. C. Brown, A. G. Emslie, E. P. Kontar, Astrophys. J. Lett. **595**, L115 (2003), doi:10.1086/378169

J. C. Brown, J. Kašparová, A. M. Massone, M. Piana, Astron. Astrophys. **486**, 1023 (2008), 0802.0621, doi:10.1051/0004-6361:200809496

J. C. Brown, J. M. Loran, Mon. Not. Roy. Astron. Soc. **212**, 245 (1985)

J. C. Brown, P. C. V. Mallik, Astron. Astrophys. **481**, 507 (2008), arXiv:0706.2823, doi:10.1051/0004-6361:20078103

J. C. Brown, P. C. V. Mallik, Astrophys. J. Lett. **697**, L6 (2009), doi:10.1088/0004-637X/697/1/L6

J. C. Brown, P. C. V. Mallik, N. R. Badnell, Astron. Astrophys. **515**, C1+ (2010), doi:10.1051/0004-6361:20078103e

J. C. Brown, D. B. Melrose, D. S. Spicer, Astrophys. J. **228**, 592 (1979), doi:10.1086/156883

A. M. Bykov, G. D. Fleishman, Astrophys. J. Lett. **692**, L45 (2009), 0901.2677, doi:10.1088/0004-637X/692/1/L45

P. J. Cargill, J. T. Mariska, S. K. Antiochos, Astrophys. J. **439**, 1034 (1995), doi:10.1086/175240

A. Caspi, R. P. Lin, Astrophys. J. Lett. **725**, L161 (2010), doi:10.1088/2041-8205/725/2/L161

E. W. Cliver, B. R. Dennis, A. L. Kiplinger, S. R. Kane, D. F. Neidig, N. R. Sheeley, Jr., M. J. Koomen, Astrophys. J. **305**, 920 (1986), doi:10.1086/164306
J. L. Culhane, A. T. Phillips, M. Inda-Koide, T. Kosugi, A. Fludra, H. Kurokawa, K. Makishima, C. D. Pike, T. Sakao, T. Sakurai, Solar Phys. **153**, 307 (1994)
B. R. Dennis, Solar Phys. **100**, 465 (1985)
B. R. Dennis, D. M. Zarro, Solar Phys. **146**, 177 (1993)
S. V. D'Iakonov, B. V. Somov, Solar Phys. **116**, 119 (1988)
E. Dzifčáková, M. Karlický, Solar Phys. **250**, 329 (2008), doi:10.1007/s11207-008-9219-3
A. G. Emslie, Astrophys. J. **224**, 241 (1978), doi:10.1086/156371
A. G. Emslie, Astrophys. J. **235**, 1055 (1980), doi:10.1086/157709
A. G. Emslie, Astrophys. J. Lett. **595**, L119 (2003), doi:10.1086/378168
A. G. Emslie, E. P. Kontar, S. Krucker, R. P. Lin, Astrophys. J. Lett. **595**, L107 (2003), doi:10.1086/378931
A. G. Emslie, H. Kucharek, B. R. Dennis, N. Gopalswamy, G. D. Holman, G. H. Share, A. Vourlidas, T. G. Forbes, P. T. Gallagher, G. M. Mason, T. R. Metcalf, R. A. Mewaldt, R. J. Murphy, R. A. Schwartz, T. H. Zurbuchen, Journal of Geophysical Research (Space Physics) **109**, 10104 (2004), doi:10.1029/2004JA010571
M. W. Ewell, Jr., H. Zirin, J. B. Jensen, T. S. Bastian, Astrophys. J. **403**, 426 (1993), doi:10.1086/172213
G. H. Fisher, S. L. Hawley, Astrophys. J. **357**, 243 (1990), doi:10.1086/168911
L. Fletcher, Astron. Astrophys. **303**, L9+ (1995)
L. Fletcher, H. S. Hudson, Solar Phys. **210**, 307 (2002), doi:10.1023/A:1022479610710
L. Fletcher, P. C. H. Martens, Astrophys. J. **505**, 418 (1998), doi:10.1086/306137
L. Fletcher et al., Space Sci. Rev. pp. XXX–XXX (2011)
T. G. Forbes, Astrophys. J. **305**, 553 (1986), doi:10.1086/164268
K. J. Frost, B. R. Dennis, Astrophys. J. **165**, 655 (1971)
W. Q. Gan, Astrophys. Spa. Sci. **260**, 515 (1998)
W. Q. Gan, Y. P. Li, J. Chang, Astrophys. J. **552**, 858 (2001), doi:10.1086/320574
J. A. Grayson, S. Krucker, R. P. Lin, Astrophys. J. **707**, 1588 (2009), doi:10.1088/0004-637X/707/2/1588
P. C. Grigis, A. O. Benz, Astron. Astrophys. **426**, 1093 (2004), arXiv:astro-ph/0407431, doi:10.1051/0004-6361:20041367
P. C. Grigis, A. O. Benz, Astron. Astrophys. **434**, 1173 (2005), arXiv:astro-ph/0501431, doi:10.1051/0004-6361:20042265
P. C. Grigis, A. O. Benz, Astron. Astrophys. **458**, 641 (2006), arXiv:astro-ph/0606339, doi:10.1051/0004-6361:20065809
P. C. Grigis, A. O. Benz, Astrophys. J. **683**, 1180 (2008), 0708.2472, doi:10.1086/589826
I. G. Hannah, E. P. Kontar, O. K. Sirenko, Astrophys. J. Lett. **707**, L45 (2009), 0911.0314, doi:10.1088/0004-637X/707/1/L45
E. Haug, Astron. Astrophys. **326**, 417 (1997)
S. Hayakawa, K. Kitao, Progress of Theoretical Physics **16**, 139 (1956)
J. Hénoux, M. Karlický, Astron. Astrophys. **407**, 1103 (2003), doi:10.1051/0004-6361:20030616
G. D. Holman, Astrophys. J. **293**, 584 (1985), doi:10.1086/163263
G. D. Holman, in *Bulletin of the American Astronomical Society* (1996), volume 28 of *Bulletin of the American Astronomical Society*, pp. 939–+
G. D. Holman, Astrophys. J. **586**, 606 (2003), doi:10.1086/367554
G. D. Holman, Advances in Space Research **35**, 1669 (2005), doi:10.1016/j.asr.2004.11.022
G. D. Holman, D. Eichler, M. R. Kundu, in *Radio Physics of the Sun*, ed. by M. R. Kundu, T. E. Gergely (1980), volume 86 of *IAU Symposium*, pp. 457–459
G. D. Holman, M. R. Kundu, K. Papadopoulos, Astrophys. J. **257**, 354 (1982), doi:10.1086/159994
G. D. Holman, L. Sui, J. McTiernan, V. Petrosian, in *Multi-Wavelength Observations of Coronal Structure and Dynamics*, ed. by P. C. H. Martens, D. Cauffman (2002), pp. 405–+
G. D. Holman, L. Sui, R. A. Schwartz, A. G. Emslie, Astrophys. J. Lett. **595**, L97 (2003), doi:10.1086/378488
P. Hoyng, A. Duijveman, M. E. Machado, D. M. Rust, Z. Svestka, A. Boelee, C. de Jager, K. T. Frost, H. Lafleur, G. M. Simnett, H. F. van Beek, B. E. Woodgate, Astrophys. J. Lett. **246**, L155+ (1981), doi:10.1086/183574
P. Hoyng, H. F. van Beek, J. C. Brown, Solar Phys. **48**, 197 (1976)
H. Hudson, J. Ryan, ARAA **33**, 239 (1995), doi:10.1146/annurev.aa.33.090195.001323
H. S. Hudson, in *Bulletin of the American Astronomical Society* (1991), volume 23 of *Bulletin of the American Astronomical Society*, pp. 1064–+
H. S. Hudson, F. Fárník, in *ESA Special Publication*, ed. by J. Kuijpers (2002), volume 506 of *ESA Special Publication*, pp. 261–264

Y. W. Jiang, S. Liu, W. Liu, V. Petrosian, Astrophys. J. **638**, 1140 (2006), arXiv:astro-ph/0508532, doi:10.1086/498863
C. M. Johns, R. P. Lin, Solar Phys. **137**, 121 (1992)
S. W. Kahler, Space Science Reviews **129**, 359 (2007), doi:10.1007/s11214-007-9143-0
S. R. Kane, K. A. Anderson, Astrophys. J. **162**, 1003 (1970)
M. Karlický, Astrophys. J. **690**, 189 (2009), doi:10.1088/0004-637X/690/1/189
M. Karlický, J. Kašparová, Astron. Astrophys. **506**, 1437 (2009), 0909.0146, doi:10.1051/0004-6361/200912616
M. Karlický, D. H. Nickeler, M. Bárta, Astron. Astrophys. **486**, 325 (2008), doi:10.1051/0004-6361:200809455
J. Kašparová, M. Karlický, E. P. Kontar, R. A. Schwartz, B. R. Dennis, Solar Phys. **232**, 63 (2005), arXiv:astro-ph/0508636, doi:10.1007/s11207-005-1581-9
J. Kašparová, E. P. Kontar, J. C. Brown, Astron. Astrophys. **466**, 705 (2007), arXiv:astro-ph/0701871, doi:10.1051/0004-6361:20066689
A. Kerdraon, J.-M. Delouis, in *Coronal Physics from Radio and Space Observations*, ed. by G. Trottet (1997), volume 483 of *Lecture Notes in Physics*, *Berlin Springer Verlag*, pp. 192–+
A. L. Kiplinger, Astrophys. J. **453**, 973 (1995), doi:10.1086/176457
J. W. Knight, P. A. Sturrock, Astrophys. J. **218**, 306 (1977)
Y.-K. Ko, J. C. Raymond, J. Lin, G. Lawrence, J. Li, A. Fludra, Astrophys. J. **594**, 1068 (2003), doi:10.1086/376982
H. W. Koch, J. W. Motz, Reviews of Modern Physics **31**, 920 (1959), doi:10.1103/RevModPhys.31.920
E. P. Kontar, J. C. Brown, Advances in Space Research **38**, 945 (2006a), arXiv:astro-ph/0508418, doi:10.1016/j.asr.2005.09.029
E. P. Kontar, J. C. Brown, Astrophys. J. Lett. **653**, L149 (2006b), arXiv:astro-ph/0611170, doi:10.1086/510586
E. P. Kontar, J. C. Brown, A. G. Emslie, R. A. Schwartz, D. M. Smith, R. C. Alexander, Astrophys. J. Lett. **595**, L123 (2003), doi:10.1086/378172
E. P. Kontar, J. C. Brown, G. K. McArthur, Solar Phys. **210**, 419 (2002), doi:10.1023/A:1022494318540
E. P. Kontar, E. Dickson, J. Kašparová, Solar Phys. pp. 149–+ (2008a), 0805.1470, doi:10.1007/s11207-008-9249-x
E. P. Kontar, I. G. Hannah, N. L. S. Jeffrey, M. Battaglia, Astrophys. J. **717**, 250 (2010), 1005.0599, doi:10.1088/0004-637X/717/1/250
E. P. Kontar, I. G. Hannah, A. L. MacKinnon, Astron. Astrophys. **489**, L57 (2008b), 0808.3334, doi:10.1051/0004-6361:200810719
E. P. Kontar et al., Space Sci. Rev. pp. XXX–XXX (2011)
N. A. Krall, A. W. Trivelpiece, *Principles of plasma physics* (International Student Edition - International Series in Pure and Applied Physics, Tokyo: McGraw-Hill Kogakusha, 1973, 1973)
S. Krucker, M. Battaglia, P. J. Cargill, L. Fletcher, H. S. Hudson, A. L. MacKinnon, S. Masuda, L. Sui, M. Tomczak, A. L. Veronig, L. Vlahos, S. M. White, Astron. Astrophys. Rev. **16**, 155 (2008a), doi:10.1007/s00159-008-0014-9
S. Krucker, G. J. Hurford, A. L. MacKinnon, A. Y. Shih, R. P. Lin, Astrophys. J. Lett. **678**, L63 (2008b), doi:10.1086/588381
S. Krucker, R. P. Lin, Solar Phys. **210**, 229 (2002), doi:10.1023/A:1022469902940
S. Krucker, R. P. Lin, Astrophys. J. **673**, 1181 (2008), doi:10.1086/524010
S. Krucker, P. Saint-Hilaire, S. Christe, S. M. White, A. D. Chavier, S. D. Bale, R. P. Lin, Astrophys. J. **681**, 644 (2008c), doi:10.1086/588549
J. Leach, V. Petrosian, Astrophys. J. **269**, 715 (1983), doi:10.1086/161081
K. W. Lee, J. Büchner, N. Elkina, Astron. Astrophys. **478**, 889 (2008), doi:10.1051/0004-6361:20078419
J. Lin, Y.-K. Ko, L. Sui, J. C. Raymond, G. A. Stenborg, Y. Jiang, S. Zhao, S. Mancuso, Astrophys. J. **622**, 1251 (2005), doi:10.1086/428110
R. P. Lin, B. R. Dennis, G. J. Hurford, D. M. Smith, A. Zehnder, P. R. Harvey, D. W. Curtis, D. Pankow, P. Turin, M. Bester, A. Csillaghy, M. Lewis, N. Madden, H. F. van Beek, M. Appleby, T. Raudorf, J. McTiernan, R. Ramaty, E. Schmahl, R. Schwartz, S. Krucker, R. Abiad, T. Quinn, P. Berg, M. Hashii, R. Sterling, R. Jackson, R. Pratt, R. D. Campbell, D. Malone, D. Landis, C. P. Barrington-Leigh, S. Slassi-Sennou, C. Cork, D. Clark, D. Amato, L. Orwig, R. Boyle, I. S. Banks, K. Shirey, A. K. Tolbert, D. Zarro, F. Snow, K. Thomsen, R. Henneck, A. McHedlishvili, P. Ming, M. Fivian, J. Jordan, R. Wanner, J. Crubb, J. Preble, M. Matranga, A. Benz, H. Hudson, R. C. Canfield, G. D. Holman, C. Crannell, T. Kosugi, A. G. Emslie, N. Vilmer, J. C. Brown, C. Johns-Krull, M. Aschwanden, T. Metcalf, A. Conway, Solar Phys. **210**, 3 (2002), doi:10.1023/A:1022428818870
R. P. Lin, R. A. Schwartz, Astrophys. J. **312**, 462 (1987), doi:10.1086/164891

R. P. Lin, R. A. Schwartz, R. M. Pelling, K. C. Hurley, Astrophys. J. Lett. **251**, L109 (1981), doi:10.1086/183704
S. Liu, L. Fletcher, Astrophys. J. Lett. **701**, L34 (2009), 0907.1874, doi:10.1088/0004-637X/701/1/L34
S. Liu, F. Han, L. Fletcher, Astrophys. J. **709**, 58 (2010), 0912.0402, doi:10.1088/0004-637X/709/1/58
W. Liu, S. Liu, Y. W. Jiang, V. Petrosian, Astrophys. J. **649**, 1124 (2006), arXiv:astro-ph/0603510, doi:10.1086/506268
W. Liu, V. Petrosian, B. R. Dennis, G. D. Holman, Astrophys. J. **693**, 847 (2009a), 0805.1055, doi:10.1088/0004-637X/693/1/847
W. Liu, V. Petrosian, B. R. Dennis, Y. W. Jiang, Astrophys. J. **676**, 704 (2008), arXiv:0709.1963, doi:10.1086/527538
W. Liu, T. Wang, B. R. Dennis, G. D. Holman, Astrophys. J. **698**, 632 (2009b), 0902.1805, doi:10.1088/0004-637X/698/1/632
A. L. MacKinnon, P. C. V. Mallik, Astron. Astrophys. **510**, A29+ (2010), 0908.3903, doi:10.1051/0004-6361/200913190
G. Mann, H. Aurass, W. Voigt, J. Paschke, in *Coronal Streamers, Coronal Loops, and Coronal and Solar Wind Composition*, ed. by C. Mattok (1992), volume 348 of *ESA Special Publication*, pp. 129–132
G. Mann, H. Aurass, A. Warmuth, Astron. Astrophys. **454**, 969 (2006), doi:10.1051/0004-6361:20064990
A. M. Massone, A. G. Emslie, E. P. Kontar, M. Piana, M. Prato, J. C. Brown, Astrophys. J. **613**, 1233 (2004), doi:10.1086/423127
S. Masuda, T. Kosugi, H. Hara, S. Tsuneta, Y. Ogawara, Nature **371**, 495 (1994), doi:10.1038/371495a0
J. M. McTiernan, S. R. Kane, J. M. Loran, J. R. Lemen, L. W. Acton, H. Hara, S. Tsuneta, T. Kosugi, Astrophys. J. Lett. **416**, L91+ (1993), doi:10.1086/187078
J. M. McTiernan, V. Petrosian, Astrophys. J. **359**, 524 (1990), doi:10.1086/169084
D. B. Melrose, Solar Phys. **130**, 3 (1990)
D. B. Melrose, J. C. Brown, Mon. Not. Roy. Astron. Soc. **176**, 15 (1976)
D. B. Melrose, G. A. Dulk, Astrophys. J. **259**, 844 (1982), doi:10.1086/160219
T. R. Metcalf, D. Alexander, Astrophys. J. **522**, 1108 (1999), doi:10.1086/307679
J. A. Miller, P. J. Cargill, A. G. Emslie, G. D. Holman, B. R. Dennis, T. N. LaRosa, R. M. Winglee, S. G. Benka, S. Tsuneta, J. Geophys. Res. **102**, 14631 (1997), doi:10.1029/97JA00976
J. A. Miller, T. N. Larosa, R. L. Moore, Astrophys. J. **461**, 445 (1996), doi:10.1086/177072
R. O. Milligan, P. T. Gallagher, M. Mathioudakis, D. S. Bloomfield, F. P. Keenan, R. A. Schwartz, Astrophys. J. Lett. **638**, L117 (2006a), arXiv:astro-ph/0509664, doi:10.1086/500555
R. O. Milligan, P. T. Gallagher, M. Mathioudakis, F. P. Keenan, Astrophys. J. Lett. **642**, L169 (2006b), arXiv:astro-ph/0603652, doi:10.1086/504592
V. M. Nakariakov, C. Foullon, E. Verwichte, N. P. Young, Astron. Astrophys. **452**, 343 (2006), doi:10.1051/0004-6361:20054608
W. M. Neupert, Astrophys. J. Lett. **153**, L59+ (1968), doi:10.1086/180220
Z. Ning, Solar Phys. **248**, 99 (2008), doi:10.1007/s11207-008-9124-9
Z. Ning, Science in China G: Physics and Astronomy **52**, 1686 (2009), doi:10.1007/s11433-009-0219-6
N. Nitta, B. R. Dennis, A. L. Kiplinger, Astrophys. J. **353**, 313 (1990), doi:10.1086/168618
L. Ofman, L. Sui, Astrophys. J. Lett. **644**, L149 (2006), doi:10.1086/505622
G. K. Parks, J. R. Winckler, Astrophys. J. Lett. **155**, L117+ (1969)
L. Peterson, J. R. Winckler, Physical Review Letters **1**, 205 (1958), doi:10.1103/PhysRevLett.1.205
L. E. Peterson, J. R. Winckler, J. Geophys. Res. **64**, 697 (1959), doi:10.1029/JZ064i007p00697
V. Petrosian, T. Q. Donaghy, Astrophys. J. **527**, 945 (1999), arXiv:astro-ph/9907181, doi:10.1086/308133
V. Petrosian, T. Q. Donaghy, J. M. McTiernan, Astrophys. J. **569**, 459 (2002), arXiv:astro-ph/0112363, doi:10.1086/339240
M. Piana, A. M. Massone, G. J. Hurford, M. Prato, A. G. Emslie, E. P. Kontar, R. A. Schwartz, Astrophys. J. **665**, 846 (2007), doi:10.1086/519518
M. Piana, A. M. Massone, E. P. Kontar, A. G. Emslie, J. C. Brown, R. A. Schwartz, Astrophys. J. Lett. **595**, L127 (2003), doi:10.1086/378171
M. Prato, A. G. Emslie, E. P. Kontar, A. M. Massone, M. Piana, Astrophys. J. **706**, 917 (2009), doi:10.1088/0004-637X/706/1/917
J. Qiu, H. Wang, C. Z. Cheng, D. E. Gary, Astrophys. J. **604**, 900 (2004), doi:10.1086/382122
G. Rausche, H. Aurass, G. Mann, M. Karlický, C. Vocks, Solar Phys. **245**, 327 (2007), doi:10.1007/s11207-007-9036-0
J. C. Raymond, G. Holman, A. Ciaravella, A. Panasyuk, Y.-K. Ko, J. Kohl, Astrophys. J. **659**, 750 (2007), arXiv:astro-ph/0701359, doi:10.1086/512604
K. K. Reeves, S. J. Moats, Astrophys. J. **712**, 429 (2010), doi:10.1088/0004-637X/712/1/429

H. L. Rowland, L. Vlahos, Astron. Astrophys. **142**, 219 (1985)
P. Saint-Hilaire, *Energy release in solar flares*, Ph.D. thesis, Ph.D dissertation, 2005. 157 pages; Switzerland: Eidgenoessische Technische Hochschule Zuerich (Switzerland); 2005. Publication Number: AAT C819508. DAI-C 66/02, p. 431, Summer 2005 (2005)
P. Saint-Hilaire, A. O. Benz, Astron. Astrophys. **435**, 743 (2005), doi:10.1051/0004-6361:20041918
P. Saint-Hilaire, S. Krucker, S. Christe, R. P. Lin, Astrophys. J. **696**, 941 (2009), doi:10.1088/0004-637X/696/1/941
P. Saint-Hilaire, S. Krucker, R. P. Lin, Solar Phys. **250**, 53 (2008), doi:10.1007/s11207-008-9193-9
R. Saldanha, S. Krucker, R. P. Lin, Astrophys. J. **673**, 1169 (2008), doi:10.1086/524929
C. Shao, G. Huang, Astrophys. J. **691**, 299 (2009a), doi:10.1088/0004-637X/691/1/299
C. Shao, G. Huang, Astrophys. J. Lett. **694**, L162 (2009b), doi:10.1088/0004-637X/694/2/L162
T. V. Siversky, V. V. Zharkova, Astron. Astrophys. **504**, 1057 (2009), 0907.1911, doi:10.1051/0004-6361/200912341
D. M. Smith, R. P. Lin, P. Turin, D. W. Curtis, J. H. Primbsch, R. D. Campbell, R. Abiad, P. Schroeder, C. P. Cork, E. L. Hull, D. A. Landis, N. W. Madden, D. Malone, R. H. Pehl, T. Raudorf, P. Sangsingkeow, R. Boyle, I. S. Banks, K. Shirey, R. Schwartz, Solar Phys. **210**, 33 (2002), doi:10.1023/A:1022400716414
Y. Su, G. D. Holman, B. R. Dennis, A. K. Tolbert, R. A. Schwartz, Astrophys. J. **705**, 1584 (2009), doi:10.1088/0004-637X/705/2/1584
L. Sui, G. D. Holman, Astrophys. J. Lett. **596**, L251 (2003), doi:10.1086/379343
L. Sui, G. D. Holman, B. R. Dennis, Astrophys. J. **612**, 546 (2004), doi:10.1086/422515
L. Sui, G. D. Holman, B. R. Dennis, Astrophys. J. **626**, 1102 (2005a), doi:10.1086/430086
L. Sui, G. D. Holman, B. R. Dennis, Astrophys. J. **646**, 605 (2006a), doi:10.1086/504885
L. Sui, G. D. Holman, B. R. Dennis, Astrophys. J. Lett. **645**, L157 (2006b), doi:10.1086/506325
L. Sui, G. D. Holman, B. R. Dennis, Astrophys. J. **670**, 862 (2007), doi:10.1086/522198
L. Sui, G. D. Holman, B. R. Dennis, Advances in Space Research **41**, 976 (2008), doi:10.1016/j.asr.2007.03.031
L. Sui, G. D. Holman, B. R. Dennis, S. Krucker, R. A. Schwartz, K. Tolbert, Solar Phys. **210**, 245 (2002), doi:10.1023/A:1022417832283
L. Sui, G. D. Holman, S. M. White, J. Zhang, Astrophys. J. **633**, 1175 (2005b), doi:10.1086/462410
E. Tandberg-Hanssen, A. G. Emslie, *The physics of solar flares* (Cambridge and New York, Cambridge University Press, 1988, 286 p., 1988)
S. Tsuneta, T. Naito, Astrophys. J. Lett. **495**, L67+ (1998), arXiv:astro-ph/9801109, doi:10.1086/311207
M. Väänänen, S. Pohjolainen, Solar Phys. **241**, 279 (2007), doi:10.1007/s11207-007-0235-5
G. H. J. van den Oord, Astron. Astrophys. **234**, 496 (1990)
A. Veronig, M. Temmer, A. Hanslmeier, W. Otruba, M. Messerotti, Astron. Astrophys. **382**, 1070 (2002a), arXiv:astro-ph/0207234, doi:10.1051/0004-6361:20011694
A. Veronig, B. Vršnak, B. R. Dennis, M. Temmer, A. Hanslmeier, J. Magdalenić, Astron. Astrophys. **392**, 699 (2002b), arXiv:astro-ph/0207217, doi:10.1051/0004-6361:20020947
A. Veronig, B. Vršnak, M. Temmer, A. Hanslmeier, Solar Phys. **208**, 297 (2002c), arXiv:astro-ph/0208088
A. M. Veronig, J. C. Brown, Astrophys. J. Lett. **603**, L117 (2004), doi:10.1086/383199
A. M. Veronig, J. C. Brown, B. R. Dennis, R. A. Schwartz, L. Sui, A. K. Tolbert, Astrophys. J. **621**, 482 (2005), doi:10.1086/427274
N. Vilmer, G. Trotter, S. R. Kane, Astron. Astrophys. **108**, 306 (1982)
N. Vilmer et al., Space Sci. Rev. pp. XXX–XXX (2011)
L. Vlahos, H. L. Rowland, Astron. Astrophys. **139**, 263 (1984)
T. Wang, L. Sui, J. Qiu, Astrophys. J. Lett. **661**, L207 (2007), arXiv:0709.2329, doi:10.1086/519004
A. Warmuth, G. D. Holman, B. R. Dennis, G. Mann, H. Aurass, R. O. Milligan, Astrophys. J. **699**, 917 (2009), doi:10.1088/0004-637X/699/1/917
A. Warmuth, G. Mann, H. Aurass, Central European Astrophysical Bulletin **31**, 135 (2007)
H. P. Warren, Astrophys. J. **637**, 522 (2006), arXiv:astro-ph/0507328, doi:10.1086/497904
H. P. Warren, S. K. Antiochos, Astrophys. J. Lett. **611**, L49 (2004), doi:10.1086/423840
D. F. Webb, J. Burkepile, T. G. Forbes, P. Riley, Journal of Geophysical Research (Space Physics) **108**, 1440 (2003), doi:10.1029/2003JA009923
M. S. Wheatland, D. B. Melrose, Solar Phys. **158**, 283 (1995)
S. M. White et al., Space Sci. Rev. pp. XXX–XXX (2011)
R. M. Winglee, A. L. Kiplinger, D. M. Zarro, G. A. Dulk, J. R. Lemen, Astrophys. J. **375**, 366 (1991), doi:10.1086/170196

Y. Xu, A. G. Emslie, G. J. Hurford, Astrophys. J. **673**, 576 (2008), doi:10.1086/524184
V. V. Zharkova, M. Gordovskyy, Astron. Astrophys. **432**, 1033 (2005), doi:10.1051/0004-6361:20041102
V. V. Zharkova, M. Gordovskyy, Astrophys. J. **651**, 553 (2006), doi:10.1086/506423
V. V. Zharkova et al., Space Sci. Rev. pp. XXX–XXX (2011)

Index

This figure "zharkova_left_low.gif" is available in "gif" format from:

http://arxiv.org/ps/1109.6496v1